INVESTIGATION OF METAL OXIDES FROM GREEN WASTE FOR GROW LIGHT

Thesis Submitted for the Award of the Degree of

DOCTOR OF PHILOSOPHY

in

Physics

By

Jasmeen Kaur

Registration Number: 12021157

Supervised By

Suman Rani (11795)

Department of Physics (Professor)

School of Chemical Engineering and Physical Sciences

LOVELY PROFESSIONAL UNIVERSITY, PUNJAB
2025

DECLARATION

I, hereby declare that the presented work in the thesis entitled "**Investigation of Metal Oxides from Green waste for Grow light**" in fulfillment of degree of Doctor of Philosophy (Ph.D.) is outcome of research work carried out by me under the supervision of Suman Rani, working as Professor, in the Dept. of Physics, School of chemical Engineering and Physical sciences of Lovely Professional University, Punjab, India. In keeping with general practice of reporting scientific observations, due acknowledgements have been made whenever work described here has been based on findings of other investigator. This work has not been submitted in part or full to any other University or Institute for the award of any degree.

(Signature of Scholar)

Name of the scholar: Jasmeen Kaur

Registration No: 12021157

Department/School: Dept. of Physics, School of Chemical Engineering and Physical Sciences

Lovely Professional University, Punjab, India

CERTIFICATE

This is to certify that the work reported in the Ph. D. thesis entitled "**Investigation of Metal Oxides from Green Waste for Grow Light**" submitted in fulfilment of the requirement for the award of the degree of **Doctor of Philosophy (Ph.D.)** in the Dept. of Physics, School of Chemical Engineering and Physical sciences, is a research work carried out by Jasmeen Kaur (12021157), is Bonafide record of his/her original work carried out under my supervision and that no part of thesis has been submitted for any other degree, diploma or equivalent course.

(Signature of Supervisor)

Name of supervisor: Suman Rani

Designation: Professor

Department/School: Dept. of Physics, School of Chemical Engineering and Physical Sciences

University: Lovely Professional University

Abstract

This research focuses on developing an eco-friendly method for synthesizing metal oxides (MOs) that enhance the efficiency of grow lights, which are crucial for promoting plant growth. These specialized lights aim to reproduce the natural light spectrum of the sun, which is essential for the healthy development of plants. Light serves as the primary energy source for photosynthesis, and the specific wavelengths that plants absorb are critical to their growth. Notably, chlorophyll, the green pigment in plants, carries out the most effective absorption in blue (400-500 nm) and red (600-700 nm) wavelengths. In indoor gardening and agriculture, artificial grow lights have become a popular solution, as they provide a controlled and customizable light source tailored to the specific needs of various plant species. This adaptability allows for optimal growth conditions, regardless of external light availability.

The study proposes investigating the properties of metal oxides that can enhance the light emitted by these artificial grow lights. By utilizing green synthesis methods, the research aims to minimize environmental impact while producing effective materials for light enhancement. This innovative approach not only seeks to improve plant growth through better light quality but also aligns with sustainable agriculture practices. Ultimately, this research has the potential to contribute significantly to indoor farming techniques, supporting healthier plant development and more efficient use of energy resources. The synthesis of metal oxides from fruit and vegetable waste as a sustainable approach for developing materials suitable for grow lights, detailed methodology was discussed in Chapter 3. With the increasing demand for energy-efficient lighting in agriculture, utilizing biodegradable resources, particularly organic waste, presents a novel pathway for producing functional metal oxides essential for optical applications. The waste of various fruit and vegetable residues was extracted and transformed into metal oxide nanoparticles.

This study explores some metal oxides, specifically CuO (copper oxide), ZnO (zinc oxide), NiO (Nickel oxide), MgO (magnesium oxide), and Fe_3O_4(Ferric oxide) from $^+$waste peels of fruits and vegetables, aimed at developing materials that meet the

requirements for grow lights in agricultural applications. We initially investigated the UV absorption properties of these metal oxides to fine-tune their band gaps, optimizing them for plant light needs. Various nanocomposites were synthesized from these metal oxides. This study investigates several nanocomposites of metal oxide, CuO/MgO, CuO/ZnO, NiO/MgO, and CuO/ZnO to identify the most suitable host for enhancing grow light applications. The focus is particularly on optical properties and band gap energies of these materials, as they are crucial for effective light absorption in the wavelengths critical for photosynthesis.

Through comprehensive UV absorption studies, it was determined that the CuO/ZnO nanocomposite exhibits the most favorable characteristics for grow light applications. Among the various synthesized nanocomposites, CuO/ZnO emerged as particularly advantageous because of their unique structural and optical characteristics. The combination of copper oxide (CuO) and zinc oxide (ZnO) not only creates a synergistic effect that enhances light absorption but also allows for effective tuning of the band gap energy, optimizing it for the critical wavelengths required for photosynthesis. This tailored band gap enables the nanocomposite to absorb and emit light in the blue and red regions, aligning perfectly with chlorophyll’s absorption spectrum. With a particular emphasis on identifying a suitable host CuO/ZnO nanocomposite was then doped with terbium and cobalt to enhance its photonic performance. Doping metal oxides is a crucial strategy for enhancing the performance of artificial grow lights, particularly in optimizing their spectral output for plant growth. By introducing specific dopants typically in small concentrations into the metal oxide matrix, researchers can significantly alter the material's optical, electronic, and structural properties. This process allows for fine-tuning of the light spectrum emitted by grow lights, thereby improving the efficacy of photosynthesis in plants.

The goal of doping is to achieve the best CIE (Commission Internationale de l'Éclairage) results, which provide a standardized way to assess the color characteristics of light sources. By carefully selecting dopants, such as rare earth

elements or transition metals, the emission spectrum of metal oxides can be shifted to enhance the wavelengths that chlorophyll absorbs most effectively.

The characterization of synthesized metal oxides and their nanocomposites was conducted using a range of analytical techniques. X-ray diffraction (XRD) was utilized to determine the crystalline phases and structural properties of the samples. Fourier Transform Infrared Spectroscopy (FTIR) was used for the identification of functional groups existing in the material, providing insights into the chemical bonding and interactions. Field Emission Scanning Electron Microscopy (FE-SEM) was utilized for analyzing the morphology of the surface and size distribution of particles of synthesized materials. To investigate the optical properties, UV-visible spectroscopy was conducted to assess the absorption characteristics of nanocomposites. Additionally, Fluorescence Spectroscopy was employed to study the emission and excitation behaviors of the prepared nanocomposites focusing on the transition lines relevant for potential applications in grow lights. UV-Visible Spectroscopy was conducted to assess the absorption characteristics of nanocomposites. The evaluation of color parameters like the Color Rendering Index (CIE) and Correlated Color Temperature (CCT) further demonstrates the suitability of these synthesized materials for agricultural lighting applications. Overall, the findings from the characterization techniques confirm the promising potential of these eco-friendly synthesized nanocomposites in enhancing the efficiency and sustainability of grow light systems. This research not only highlights the potential of organic waste into valuable materials for sustainable agricultural lighting but also contributes to advancements in energy-efficient grow light technologies. Results demonstrate that the synthesized metal oxides exhibit favorable light absorption properties and contribute to the sustainability of agricultural practices by effectively repurposing organic waste. This work not only highlights a practical solution for waste management but also paves the way for innovative, eco-friendly approaches in agricultural lighting, aligning with global sustainability goals and promoting circular economy practices. The synthesis method

employed to prepare the host nanocomposite of metal oxides, specifically CuO/ZnO doped with terbium and cobalt, utilizing green synthesis techniques derived from fruit and vegetable waste. The synthesis process involved the preparation of powder samples, which were subsequently sintered at 400°C to enhance their structural integrity and optical properties.

ACKNOWLEDGMENT *

Commencing this acknowledgement with a heartfelt expression of gratitude to the divine providence that has guided my path, I extend my sincerest thanks to the almighty for bestowing upon me the strength, wisdom, and blessings that have been instrumental in every step of this journey.

I am grateful to my research supervisor, Dr. Suman Rani. Their invaluable guidance, constant encouragement, and insightful feedback have played a crucial role in shaping this research. I am immensely grateful for their assistance and direction during this process; their unwavering support and motivation will always be remembered.

I extend my sincere thanks to Dr. Kailash Juglan for their constructive criticism and valuable suggestions, which significantly enhanced the quality of this work.

I am also indebted to the faculty members of the physics department at Lovely Professional University for providing an inspiring academic environment and the resources necessary for the successful completion of my research.

I pay my deepest respects to my parents, Mr. Rajinder Singh and Mrs. Harwinder Kaur, for their blessings and for raising me with boundless affection and care. My heartfelt admiration goes to my brother, Mr. Ripandeep Singh, for his understanding and support. I am especially appreciative of my husband, Mr. Gurwinder Singh, whose support and trust have been my pillars of strength. I would like to express my deepest gratitude to my daughter, Gursifat Kaur, whose unwavering strength and support have been my greatest source of inspiration throughout this journey.. Additionally, I am grateful to my friends and colleagues, whose inspiration made this academic journey much more enjoyable.

I want to thank all the participants who have helped me by contributing vital data to this study along with their valuable advice and insights.

Jasmeen Kaur

Content

Content	Page No.
Chapter 1: Introduction	1
1.1 Grow Light Spectra	3
1.2 Green Waste	5
1.3 Metal Oxides	9
1.3.1 Optical Band Gap	11
1.4 Requirement of phosphor for grow light	12
1.5 The grow phosphor Schemes	14
1.6 Metal oxide nanocomposite	14
1.6.1 Rare Earth and transition metal for luminescent properties	15
1.7 Research Motivation	19
1.7.1 Work Plan	21
Chapter 2: Review of Literature	30-61
Chapter 3: Synthesis and Characterization	62
3.1 Introduction	62
3.2 Mechanism behind the synthesis of metal oxide from plant waste	63
3.3 Material and chemical details	64
3.4 Synthesis of Metal Oxides	66
3.4.1 Synthesis of metal oxide from Banana peels	66
3.4.2 Synthesis of nanocomposite from metal oxides	69
3.4.3 Synthesis of Terbium doped CuO/ZnO and Cobalt doped CuO/ZnO metal oxide nanocomposite	70
3.5 Characterization techniques	72
3.5.1 X Ray Diffraction	73
3.5.2 Fourier-Transform Infrared Spectroscopy (FTIR)	75
3.5.3 FESEM	77
3.5.4 UV-Vis Spectroscopy	78

3.5.5 Fluorescence Spectroscopy 80
Chapter 4: Metal oxides from green waste 85

4.1 Metals Oxides Synthesized from Potato Peels 85
4.1.1 XRD Spectroscopy 86
4.1.2 FESEM Analysis 87
4.1.3 EDX Analysis 89
4.1.4 FTIR Spectroscopy 91
4.1.5 UV Absorption Spectroscopy 92
4.1.6. Fluorescence Spectroscopy 93
4.1.7 Quantum Yield 96
4.2 Metal Oxide Synthesized Using Banana Peels 98
4.2.1 XRD 98
4.2.2 FTIR Spectroscopy 100
4.2.3 FESEM study 101
4.2.4 EDX Analysis 103
4.2.5 UV Absorption 104
4.2.6 Fluorescence Spectroscopy 106
4.2.7 Colorimetry 108
4.2.8 Quantum yield in fluorescence 109
Chapter 5: Metal oxides nano composite from green waste 119

5.1 Introduction 199
5.2 To Study the band gap of Nanocomposite for an optically stable host Composite 120
5.2.1 UV Absorption of nanocomposite MgO/CuO 121
5.2.2 UV Absorption of nanocomposite NiO/ZnO 122
5.2.3 UV-Vis Absorption Of nanocomposite MgO/NiO 123
5.2.4 UV-Vis Absorption Of nanocomposite CuO/ ZnO 125

5.3 Synthesis of ZnO/CuO nanocomposite 128
5.3.1 X-Ray Diffraction 128
5.3.2 FTIR (Fourier Infrared spectroscopy) 130
5.3.3 FESEM study 131
5.3.4 EDX Analysis 132
5.3.5 UV-Vis Absorption 133
5.3.6 Fluorescence Spectroscopy 133
5.3.7 Quantum Yield 136
5.3.8 Decay analysis 137
5.3.9 Color Space Conversion 138
Chapter 6: Doped CuO/ZnO Nanocomposite 145
6.1 Introduction 146
6.1.1 X-Ray Diffraction 147
6.1.2 FTIR Spectroscopy 149
6.1.3 UV-Vis Absorption 149
6.1.4 Fluorescence Spectroscopy 151
6.2 Synthesis of Cobalt doped CuO-ZnO nanocomposite 156
6.2.1 X-Ray Diffraction 156
6.2.2 Fourier transform infrared spectroscopy 159
6.2.3 UV-Vis Absorption 160
6.2.4 Fluorescence Spectroscopy 162
Chapter 7: Summary and future scope 169-172

Abbreviations and Symbols

a- Lattice Constant

ε – Lattice Strain

Å – Angstrom

D – Crystalline Size

Eg – Energy Band Gap

υ – Frequency

θ- Bragg's Diffraction angle

β – Full Width Half Maxima

d – Interplanar Spacing

δ – Dislocation Density

JCPDS- Joint Committee on Powder Diffraction Standards

n- Refractive Index

eV – Electron Volt

EDX- Energy Dispersive X-ray Spectroscopy

SEM- Scanning Electron Microscopy

TEM- Transmission Electron Microscopy

UV-Vis- Ultraviolet Visible Spectroscopy

V- Volt

K – Kelvin

nm – Nanometer

RE- Rare Earth

λ – Wavelength

XRD – X-Ray Diffraction

XPS – X-Ray Photoelectron Spectroscopy

FESEM – Field Emission Scanning Electron Spectroscopy

FTIR – Fourier Transform Infrared Spectroscopy

MOs- Metal Oxides

BP - Banana Peels

$C_{20}Z_{80}$ = 0.2 copper nitrate 0.8 zinc nitrate trihydrate

$C_{40}Z_{60}$ = 0.4 copper nitrate 0.6 zinc nitrate trihydrate

$C_{60}Z_{40}$ = 0.6 copper nitrate 0.4 zinc nitrate trihydrate

$C_{80}Z_{20}$ = 0.8 copper nitrate 0.2 zinc nitrate trihydrate

List of Figures

Figure No.	Caption of Figure	Page No.
1.1	McCree curve describes the various wavelengths required for the photosynthesis process of plant	3
1.2	Photosynthetically Active Radiation (PAR) Spectra	4
1.3	Recycling process of green waste into grow light	6
1.4	Representation of the eco-friendly waste management practices and their environmental benefits	7
1.5	Overview of the various approaches used in nanoparticles' Synthesis	9
1.6	Graphical representation of two types of band gap: (a) Direct & (b) Indirect	12
1.7	Colour chromaticity coordinates for grow light Applications	13
1.8	Schematic representation of the nanocomposite studied for grow light applications	15
1.9	Energy level diagram of Terbium Tb^{3+}	18
1.10	Energy level diagram of Terbium Co^{3+}	19
1.11	Research work plan for synthesis of metal oxides for grow light applications	21
3.1	Describing the mechanism of green synthesis of MOs from green waste	64
3.2	Steps involved in metal oxides synthesis made from waste banana peels	67
3.3	Pictorial representation of the synthesis from waste peels of banana, peas, potato using green synthesis method	68
3.4	Typical flowchart for the synthesis of nanocomposite of ZnO-CuO by green synthesis method.	70

3.5	Flowchart representation of the synthesis of Terbium/Cobalt doped CuO/ZnO nanocomposite	72
3.6	Working principle of X-Ray diffraction	74
3.7	Instrumental image of X-ray Diffractometer and results of XRD pattern of CuO, N i O and the nanocomposite of CuO-NiO at 400℃	75
3.8	Representation of the working principle of FTIR	76
3.9	Instrumental image of FTIR spectrometer and results of FTIR spectrum of CuO, NiO and the nanocomposite of CuO-NiO at 400℃	77
3.10	Instrumental image of FESEM and view of results obtained from SEM of CuO/NiO nanocomposite at 400^0 C	78
3.11	Working principle of UV-Vis absorption detector	79
3.12	Instrumental image of UV-Vis spectrometer and results of absorption spectrum of CuO-NiO at 400℃	80
3.13	(a) Working principle of fluorescence spectrophotometer (b) Jablonski "s diagram	81
3.14	Instrumental image of fluorescence spectrophotometer and results of spectrum of CuO-NiO at 400℃	82
4.1	XRD spectra of CuO, NiO, ZnO, MgO Fe_3O_4 metal oxides prepared from potato peels and sintered at 400^0C.	86
4.2	FE-SEM micrographs of the CuO, NiO, ZnO, MgO, Fe_3O_4 metal oxides prepared from potato peels and sintered at 400^0C	88
4.3	FESEM micrograph and grain size distribution analysis of MOs prepared from potato peels annealed at 400^0C.	88

4.4	EDX spectrum of CuO, NiO, ZnO, MgO, Fe_3O_4, metal oxides prepared from potato peels and sintered at 400^0C	90
4.5	FTIR spectra of CuO, NiO, ZnO, MgO, and Fe_3O_4 metal oxides synthesized using potato peels and sintered at 400°C.	91
4.6	a) Plot of UV absorption spectra of metal oxides (b) Tauc plot of the obtained UV spectra prepared from potato peels and sintered at 400 ^{0}C.	92
4.7	Fluorescence Spectra of CuO, NiO, ZnO, MgO, Fe_3O_4 metal oxides prepared from potato peels sintered at 400^0C	95
4.8	CIE coordinates of the metal oxides CuO, NiO, ZnO, Fe_3O_4, and MgO	96
4.9	Systematic representation of calculated quantum yield of metal oxides prepared from potato peels	97
4.10	XRD spectra of BP, CuO, NiO, ZnO, Fe_3O_4, and MgO metal oxides annealed	98
4.11	FTIR spectroscopy of the metal oxides prepared from banana peels annealed at 400^0C.	101
4.12	Representation of FESEM images and distribution analysis of MOs prepared from banana peels annealed at 400^0C.	102
4.13	Bar graph represents the Comparison of crystallite/particle size calculated from XRD and FESEM.	103
4.14	EDX spectrum of CuO, NiO, ZnO.Fe_3O_4 and MgO metal oxides prepared from banana peels annealed at 400^0C.	104
4.15	UV-vis spectroscopic analysis of CuO, NiO, ZnO, Fe_3O_4, and MgO metal oxide annealed at 400^0C	105

4.16	Fluorescence Spectroscopy of CuO, NiO, ZnO, Fe_3O_4 and MgO metal oxides prepared from banana peels annealed at 400^0C	106
4.17	CIE coordinates of the metal oxides CuO, NiO, ZnO, Fe_3O_4, and MgO annealed at 400^0C	109
4.18	Schematic representation of the calculated quantum yield for metal oxides synthesized from potato peels.	109
5.1	Nanocomposite prepared by using banana peels	120
5.2	(a) UV absorption (b) Tauc plot of CuO, MgO and the MgO /CuO nanocomposite sintered at 400 ^{0}C.	121
5.3	(a)UV absorption (b) Tauc plot of ZnO, NiO and the ZnO/NiO nanocomposite sintered at 400 ^{0}C	122-123
5.4	(a) UV absorption (b) Tauc plot of NiO, MgO and the NiO/MgO nanocomposite sintered at 400 ^{0}C.	124
5.5	(a)UV absorption (b) Tauc plot of CuO, ZnO and the CuO/ZnO nanocomposite sintered at 400 ^{0}C.	126
5.6	XRD spectra of Pure ZnO, CuO and nanocomposites of ZnO/CuO annealed at 400^0C.	129
5.7	Fourier transform infrared spectroscopy pure CuO, ZnO, CuO/ZnO sintered at 400^0C prepared from banana peels.	131
5.8	FESEM micrographs and bar graphs of particle size of the Pure CuO, ZnO, and C20Z80 of powder sample sintered at 400 ^{0}C respectively.	132
5.9	EDX spectrum of Pure CuO, ZnO, and C20Z80 of powder sample sintered at 400 ^{0}C respectively.	133
5.10	EDX spectrum of Pure CuO, ZnO, and C20Z80 of powder sample sintered at 400 ^{0}C respectively.	135

5.11	Integrated areas of the CuO, ZnO, and nanocomposites of ZnO-CuO metal oxides excited at 210,310 nm and sintered at 400^0 C.	135
5.12	Representation of calculated quantum yield of the ZnO, CuO ,ZnO/CuO and the nanocomposites.	137
5.13	Fluorescence Decay times were obtained for pure ZnO, CuO and nanocomposites of ZnO-CuO sintered at 400^0C.	138
5.14	CIE coordinates of the pure CuO, ZnO and the nanocomposites of CuO/ZnO excited at 210, 310 respectively	139
6.1	XRD spectra of Pure ZnO, CuO and terbium doped ZnO/CuO nanocomposite annealed at 400^0C	148
6.2	FTIR spectra of terbium doped CuO-ZnO nanocomposites prepared from banana peels and sintered at 400 ^{0}C	149
6.3	Plot of UV-Vis absorption spectrum of terbium doped CuO-ZnO nanocomposites prepared from banana peels and sintered at 400 ^{0}C. (b) Tauc plot of the obtained UV-Vis spectra	151
6.4	Transition lines /Energy level diagram of terbium	152
6.5	Fluorescence Spectra of Tb doped CuO-ZnO nanocomposites (a) Wavelength 400-600nm (b) 460-580 nm excited at 210, sintered at 400^0C (a) Wavelength 400-600nm (b) 460-580 nm excited at 210, sintered at 400^0C	152
6.6	Integrated areas of the terbium CuO- ZnO nanocomposite excited at 210 sintered at 400^0 C	154
6.7	CIE coordinates of the terbium doped CuO-ZnO nanocomposites excited at 210 sintered at 400^0 C	155
6.8	XRD spectra of Pure ZnO, CuO and nanocomposites of cobalt doped ZnO/CuO annealed at 400^0C	157

6.9	FTIR spectra of cobalt doped CuO-ZnO nanocomposites prepared from banana peels and sintered at 400 ^{0}C	160
6.10	Plot of UV-Vis absorption spectrum of Pure CuO-ZnO nanocomposites cobalt doped CuO/ZnO prepared from banana peels and sintered at 400 ^{0}C. (b) Tauc plot of the obtained UV-Vis spectra	161
6.11	Fluorescence Spectra of Cobalt doped CuO-ZnO nanocomposites (a) Wavelength 400-650nm (b) 450-580 nm excited at 210, sintered at 400^{0}C	163
6.12	CIE coordinates of the Cobalt doped CuO- ZnO nanocomposites excited at 210 sintered at 400^0 C.	164
7.1	C20Z80 doped with (a) terbium (Tb) and (b) cobalt (Co) for grow light applications.	171

List of Tables

Table No.	Caption of Table	Page No.
1.1	Detail of Various phytochemicals and reducing agents present in plant waste	7-9
1.2	Comparison of direct bandgap metal oxides needed for optical properties	11
2.1	Summary of work done in green synthesis approach of metal oxides production and their uses	48-51
3.1	Details of the chemicals used for the preparation of metal oxide.	64-65
3.2	Comprehensive overview of various waste peels used for the synthesis of metal oxides	65
3.3	Components and their quantities used for the preparation of metal oxides	67
3.4	Proportion of Copper and Zinc used in nanocomposite preparation	69
3.5	Proportion of Copper and Zinc used in synthesis of terbium /Cobalt doped CuO/ZnO	71
4.1	Details of metal oxide prepared from Potato peel, metal Precursor Salt, Average crystallite size and structure of the metal oxides	87
4.2	Elemental Composition of prepared metal oxides synthesized from potato peel.	89-90
4.3	Calculated CIE and CCT coordinates of the CuO, NiO, ZnO, MgO and Fe_3O_4	96
4.4	Information on metal oxides synthesized from banana peel, including the metal precursor salt, average crystallite size, and crystal structure of the oxides	99
4.5	Calculated optical band gap (Eg) of the metal oxides	105

	prepared by using banana peels	
4.6	Detailed colorimetry coordinates of metal oxides calculated from Fluorescence spectra obtained with 310 nm excitation.	108
5.1	Calculated Optical band gaps of the metal oxide and nanocomposite of MgO/CuO from the UV absorption data.	122
5.2	Calculated Optical band gaps of the metal oxide and nanocomposite of ZnO/NiO from the UV absorption data.	123
5.3	Calculated Optical band gaps of the metal oxide and nanocomposite of MgO/NiO from the UV absorption data.	125
5.4	Calculated Optical band gaps of the metal oxide and nanocomposite of CuO/ZnO from the UV absorption data.	127
5.5	Parameters calculated for the nanocomposites prepared from green synthesis such as crystallite size D, lattice strain of metal oxide ZnO, $C_{20}Z_{80}$, $C_{40}Z_{60}$, $C_{60}Z_{40}$, $C_{80}Z_{20}$, CuO sintered at 400^0C.	130
5.6	Calculated Integrated Areas of the prepared samples at 210 and 310 excitations	136
5.7	Calculated CIE coordinates, lifetime, and decay time of the Pure ZnO CuO and nanocomposites of ZnO/CuO annealed at 400^0C.	139-141
6.1	Parameters calculated for the nanocomposites prepared from green synthesis such as crystallite size D(nm), Lattice Strain (($\times 10^{-6}$) of Tb doped CuO/ZnO sintered at 400^0C.	148-149
6.2	Calculated CIE coordinates and CCT of the Tb doped	155

	CuO/ ZnO nanocomposites excited at 210 sintered at 400^0 C	
6.3	Parameters calculated for the nanocomposites prepared from green synthesis such as crystallite sized and lattice strain of metal oxide doped cobalt ZnO- CuO sintered at 400^0C are tabulated in table 6.3.	158
6.4	Calculated CIE coordinates and CCT and quantum yield of the Cobalt doped Cu/Zn oxide nanocomposites metal oxide excited at 210 nm sintered at 400^0 C.	164

Chapter 1

INTRODUCTION

1. Introduction

Houseplants have the unique ability to bring vitality and calm to any environment. Indoor plants are popular among decorators, and for good health, plants play an important part in everyday life. The best indoor plants for your home are easy to maintain. Plants require light to grow, blossom, and create seeds. Without a proper amount of light, carbohydrates cannot be produced, energy supplies are lost, and plants die. Indoor gardening is growing more popular in urban areas due to limited space and the need for sustainable food supplies. Indoor plants can help improve air quality by filtering pollutants and raising humidity, resulting in a healthier living environment. Many urban homes lack adequate sunlight, especially those facing north or located in densely populated areas. Grow lights help make up for this shortage. As urbanization increases, indoor gardening with grow lights becomes increasingly important for sustainable living, food security, and improving the quality of life in small areas. As a result, providing an adequate amount of light is critical for optimal plant growth. Grow light is an electric light that assists the plant to grow. It is an attempt to provide the light spectrum the same as that of the sun. As there are different stages of the plants every stage needs a different spectrum of light for each stage such as the germination phase, flowering etc. and this is the requirement of PAR light to fall in the 400–700 nm wavelength [1]. The Chlorophyll present in plants converts light energy into a different form, that is, chemical energy and it absorbs mostly in the blue and red region for the spectrum of photosynthesis. Light is an essential component for plants as it is used for photosynthesis with the help of Chlorophyll A and B. The absorbance spectrum measures how much light is absorbed by these pigments. Plants require the peaks obtained in red and blue regions which show that these two colors are important to carry out the process of photosynthesis. The light essential for the morphologically healthy development plant is blue. Red light, on the other hand, aids in photosynthesis in plants. This study will concentrate on the significance of the light.

spectrum, particularly the blue and red wavelengths, for plants' healthy growth through the absorption of chlorophyll. It will also focus on how grow lights can be used as a synthetic light source for indoor growth. Usually in the 400–780 nm region, they seek to provide the best possible light spectrum for photosynthesis [2]. Thomas Engelmann's research in 1882 showed that red light promotes flowering and fruiting, blue light significantly influences leaf growth, and green light, which is mostly reflected, was initially thought to contribute the least to photosynthesis. [3]. Six more recent studies, however, have demonstrated that green light, in addition to ultraviolet (UV) and near-infrared (NIR) light, supports plant growth and development [4]. Research has indicated that plant morphology and physiology may be greatly influenced by the various mixes of red and blue light. For example, lettuce grew more quickly when exposed to a combination of red (645 nm) and blue (470 nm) light, allowing for harvesting in as few as 5-7 days [5]. When compared to conventional lighting, LED lights with different red-blue ratios have been found to play a role in the betterment of the fresh weight of shoots, the development of the root systems, and the amount of chlorophyll in lettuce [6]. In many plant species, the blue: red ratio affects the morphology, acclimatization, and growth of seedlings. Furthermore, plant responses may also be influenced by a range of wavelengths in the red spectrum (596–664 nm), with combinations of orange, red, and hyper-red-light influencing growth characteristics in annual ornamentals [7]. These results emphasize how crucial it is to find a method for optimization of the light spectrum for effective plant growth. Red and blue photons are absorbed more because of chlorophyll a and b pigments; they are successful in promoting photosynthesis at the surface of the leaf. Green photons, on the other hand, go farther down the leaf, assisting in the lower layers' carbon fixation via the pigment β-carotene, which is an accessory pigment used in photosynthesis. The total rate of photosynthesis is established by the amalgamation of β-carotene, chlorophyll a, and chlorophyll b absorption [8, 9]. Various pigments absorb at different wavelengths and this profile of overall photosynthetic action spectrum is represented by “McCree curve”, as shown in Fig. 1.1 [10].

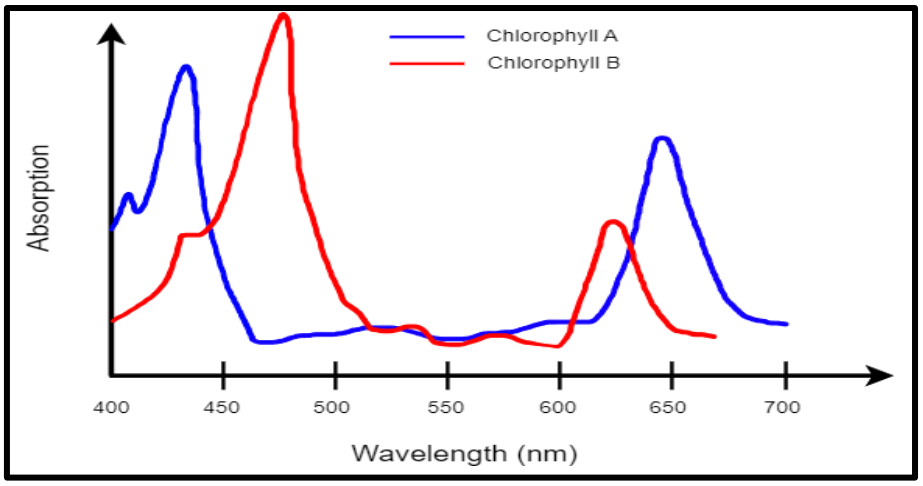

Fig. 1.1. McCree Curve describes the various wavelengths required for the photosynthesis process of plants.

1.1. Grow light Spectra

Among various grow light systems, LEDs provide the best power factor distribution or photosynthetic photon flux density (PPFD) at the same level of energy consumption as fluorescent or high intensity discharged light. LED grow lights have become a cutting-edge technology that makes precise light parameter adjustments possible for productive greenhouse farming [11]. These lights provide more control over light management in agriculture with controlled environments since they can be employed in place of or in addition to natural sunlight. Several technologies are available for growing lights, such as hybrid systems, artificial lighting, and solar spectral shaping [12]. LED-based solutions, which provide intra-canopy lighting to boost crop quality and save energy, show great promise [13]. The two most used lamps in agriculture are fluorescent lamps and high-pressure sodium lamps (HPS) [14].

Common LED lighting for indoor agriculture includes white LED tubes and light tubes with certain red-to-blue light ratios. While white LEDs are usually blue LEDs covered with YAG phosphor, which turns part of the blue light into yellow, the red and blue wavelengths match the absorption spectrum of chlorophyll and b.

Photosynthesis depends on photosynthetically active radiation (PAR), which is mostly visible in blue and red regions of the spectrum and ranges from 400 to 700 nm. Fig 1.2. represents PAR spectra required for growing light.

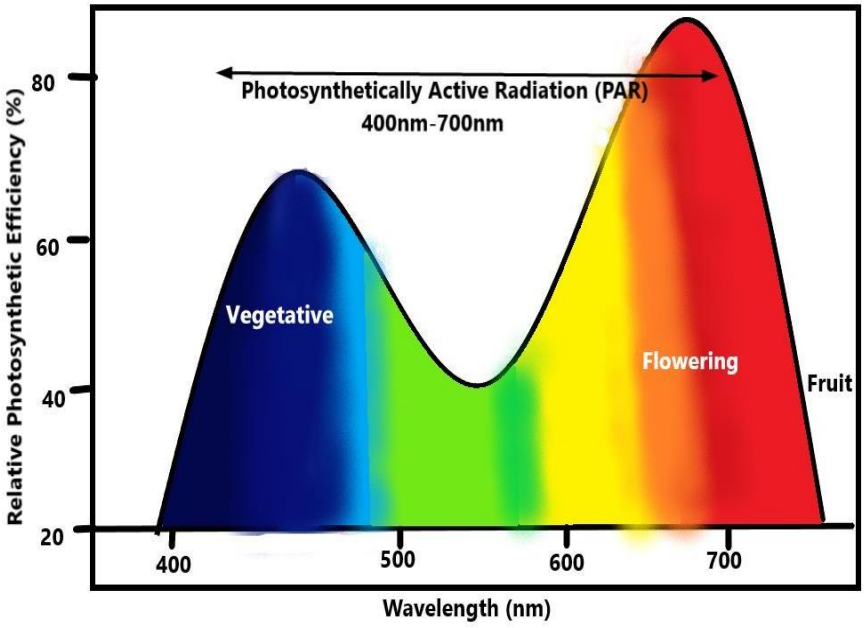

Fig 1.2. Photosynthetically Active Radiation (PAR) Spectra.

PAR, or photosynthetically active radiation, is usually measured between 400 and 700 nm and is essential for plant development and growth [15]. The conventional McCree curve for the spectrum response of photosynthesis has been called into question by recent research, indicating the necessity for a re-evaluation with greater wavelength resolution [16]. Understanding how plants react to light depends on accurate PAR measurement, and the new advances in inexpensive sensors help to differentiate between various light hues and provide an affordable option to costly commercial instruments [17].

The wavelength of light needed at different stages of plant growth:

Red light: Both the growth of stems and the expansion of leaflets depend on red light (1.9 eV to 1.87 eV, 630 nm). Additionally, this wavelength controls seed germination, dormancy durations, and flowering.

Blue Light: Both leaf thickness and the amount of chlorophyll in the plant are

impacted by blue light (400-520 nm, 3.1 eV-2.38 eV).

Green Light: To support leaf growth in the lower canopy, green light (2.48eV–2.0eV, 500–600 nm) can pass through heavy upper canopies.

Far-red light: To aid the growth of leaves in the lower part of the plant. The far-red light (1.72eV-1.67eV, 720–740 nm) also penetrates dense upper canopies. Furthermore, IR light exposure shortens a plant's flowering period. The tendency of plants exposed to far-red light to develop bigger leaves versus plants which are not exposed to this spectrum of light is another advantage of far-red light. [18,19]

1.2. Green Waste

This method reduces food waste and improves sustainability by transforming waste into useful resources. Utilizing waste materials can lessen the cost of raw materials utilized in producing metal oxides. This strategy promotes circular economic concepts, reducing environmental impact and increasing resource efficiency. It encourages using abundant, untapped resources, which may lead to advances in material science. Metal oxide synthesis from waste peels is a viable and sustainable method for managing garbage while simultaneously producing valuable materials for various industrial uses [20]. Green synthesis has received increased attention in past years because of concerns about the consequences of normal chemical synthesis procedures, which frequently employ hazardous chemicals and generate large amounts of waste, on the environment and human health. In agricultural and other plant development fields, one method of green synthesis is the use of artificial lighting systems that emit red and blue light. Biological entities such as plants, microbes, and animals are used in green synthesis instead of harsh chemical agents like sodium borohydride or hydrazine [21]. Using natural substances found in these organisms, such as flavonoids, phenolic compounds, amino acids, and other secondary metabolic products, this technique lowers metal ions and creates nanoparticles [22]. In addition to being economical and environmentally beneficial, this technique offers a good substitute for conventional chemical processes, which frequently require hazardous solvents and reducing agents. Fig 1.3 represents the recycling process of green

synthesized metal oxides for grow light spectra.

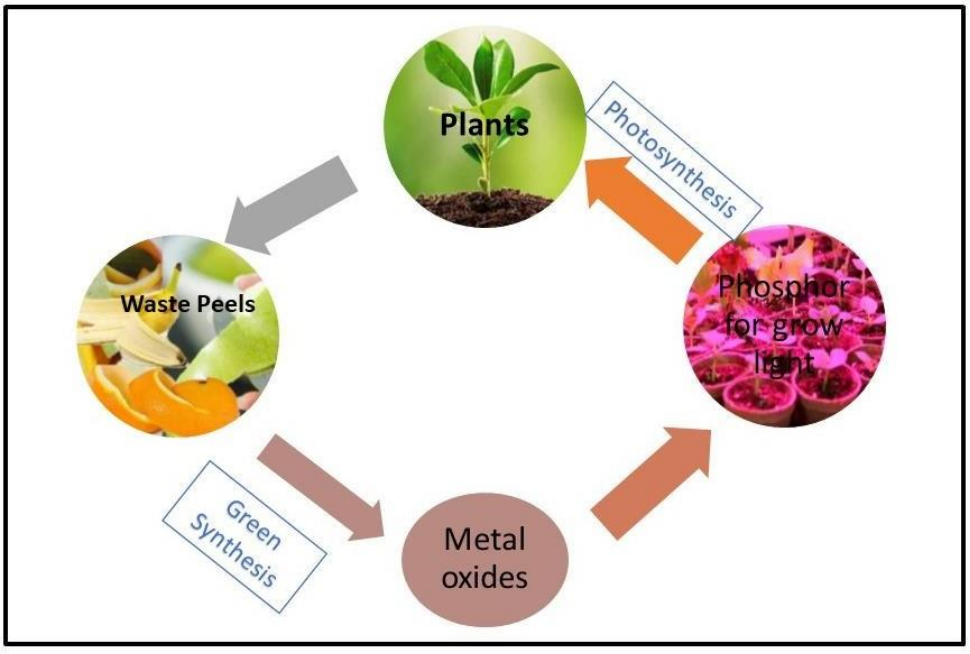

Fig 1.3. The recycling process of green waste into grow light

Every part of the plant has photo chemicals like carotenoids and polyphenols, which encompass phenolic acids, flavonoids, stilbenes, or lignans which act as a reducing agent. Therefore, it can be utilized to prepare metal oxides via green synthesis [23]. The popularity of plant-based green synthesis stems from the variety of plant metabolites that can be used to produce nanoparticles. Various types of parts of plants are present such as seeds, bark, leaves, roots, and fruits, and these have different phytochemical profiles that determine which portions are useful [24]. These plant-based techniques are beneficial because they yield nanoparticles with unique characteristics, including sizes, shapes, and surface areas, all of which are essential for drug delivery, biosensing, and catalytic applications [25]. Also, green synthesis supports the larger objectives of green chemistry by providing an environmentally benign and sustainable method of producing nanomaterials. In the case of plants, indoor growing has become necessary due to environmental changes and urbanization causing a decrease in the amount of land accessible for traditional farming. Natural

sunshine is frequently insufficient in these regulated surroundings, thus grow lights are crucial for supplying the right light spectrum for the best possible plant growth. The eco-friendly waste management practices and their environmental benefits are represented in Fig 1.4.

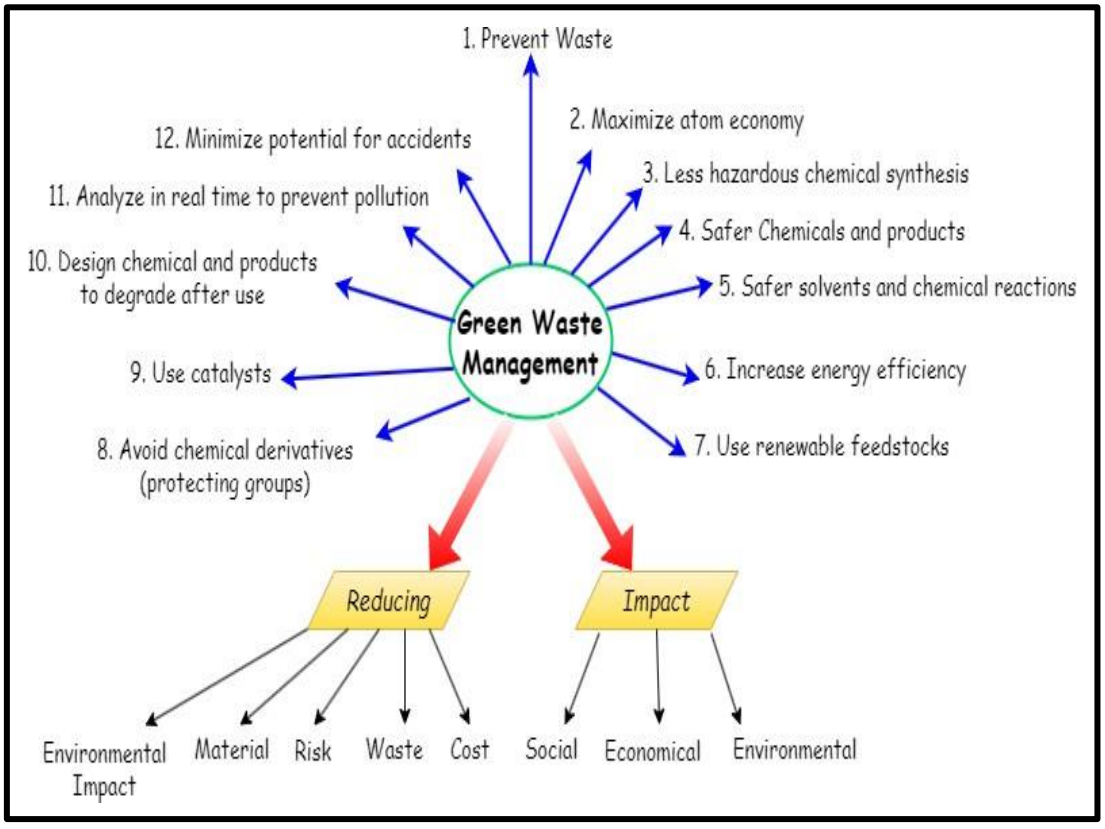

Fig 1.4. Representation of the eco-friendly waste management practices and their environmental benefits.

Table 1.1: Detail of phytochemicals that act as reducing agents present in plant waste**.**

S.no	**Plant Waste**	**Botanical Name**	**Phytochemicals**	**Phytochemicals act as reducing agent**	**References**

1	**Banana peels**	Musa	Phenolic Compounds act as a reducing agent in chemical reactions, mainly in the presence of metals.	Polyphenols: Antioxidants that help combat oxidative stress. Tannins: It has antimicrobial and anti-inflammatory properties. Carotenoids: Due to antioxidant effects this phytochemical basically contribute to health benefits.	[26, 27]
2	**Potato peels**	Solanum tuberosum	Ascorbic Acid: It acts as a reducing agent and also has antioxidant properties	Chlorogenic Acid: Acts as an antioxidant and has anticancer properties. Flavonoids: Act as an antioxidant and contribute to cardiovascular health	[28, 29]
3	**Peas peels**	Pisum sativum	Phenolic Compounds: Act as a reducing agent in biochemical processes.	Saponins: They act as an antioxidant and have a potential cholesterol-lowering effect. Flavonoids: This also contributes to	[30,31]

				antioxidant properties.	

Phytochemicals and reducing agents in the peels of bananas, potatoes, and peas contribute to their health benefits and potential uses. Peels of various fruits, as well as vegetables, are rich in phytochemicals that provide health benefits and act as reducing agents in various applications. Incorporating these peels into diets or using them in natural product formulations could leverage their beneficial properties.

1.3. Metal oxides

For synthesizing nanoparticles, there are two types of approaches as shown in Fig 1.5.

1. Top-up approach
2. Bottom-down approach.

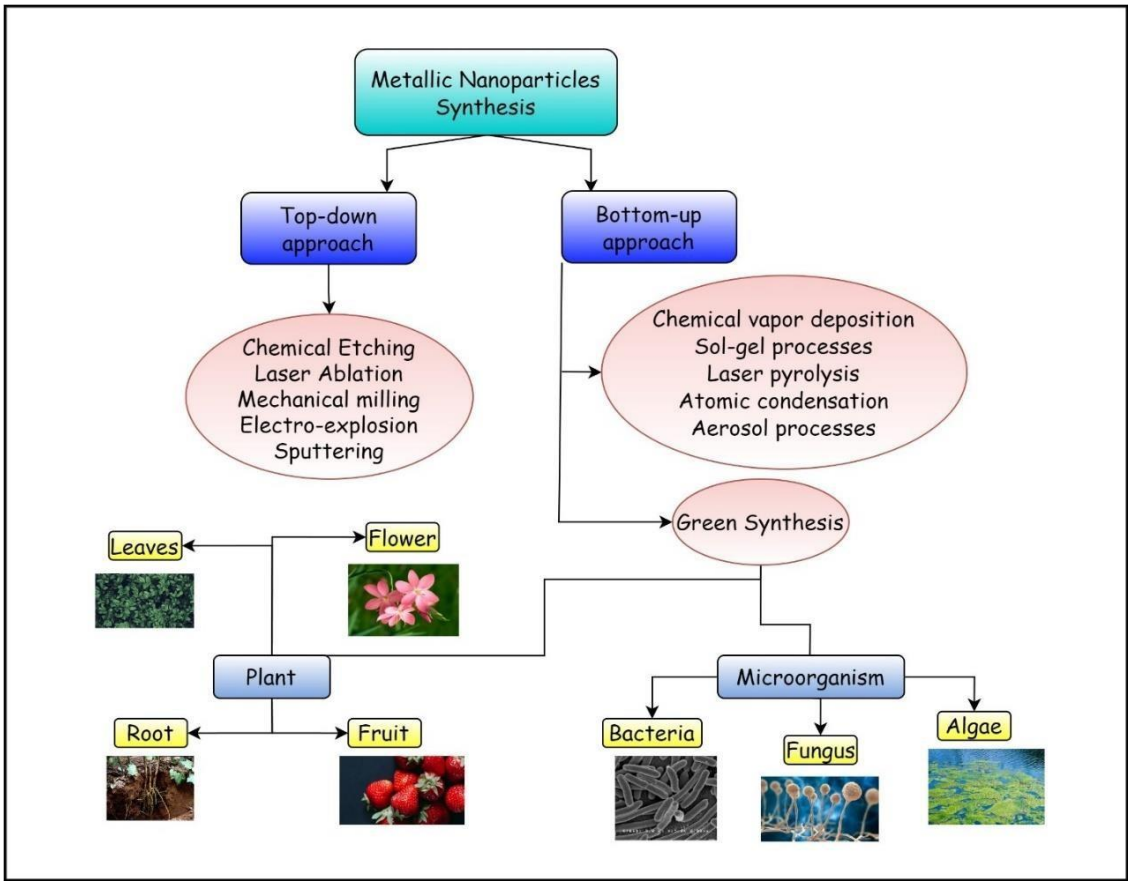

Fig 1.5. Overview of the various approaches used in nanoparticle synthesis [32]

Top-down approach

Using physical, chemical, or mechanical processes, nanoparticles are obtained by reduction of bulk materials in the top-down technique [33]. This method may result in bare nanoparticles that are prone to clumping. It has been shown that a unique top-down technique employing high-purity magnetite ore and an oleic acid coating can produce stable nanoparticles [34].

Bottom-up approach

The bottom-up approach involves using techniques such as chemical reduction, biological synthesis, and microfluidic technology to create nanoparticles from individual atoms or molecules. It is thought to be more successful at regulating nanoparticle size and form [35]. The capacity of metal oxides to produce charged particles when excited with the right amount of energy makes them an excellent technology for electronics and environmental remediation. Because metal oxides have special characteristics, optical techniques can reveal important information about the metal oxides released by different UV-Vis-IR light components.

Due to their many functional characteristics, metal oxide nanostructures can be used in various applications, including gas sensors, solar cells, optoelectronics, catalysis, corrosion resistance, and environmental protection [36, 37]. The oxide's optical, electrical, chemical, and mechanical behaviors are shaped by various elements, including its doping levels, composition, intrinsic defects, and crystal structure. These factors have a major impact on the oxide's functional characteristics. The morpho-structural features and, consequently, the physicochemical properties of metal oxides are greatly influenced by the synthesis methods and processing conditions [38]. Furthermore, their band gaps and electronic structures may be precisely adjusted by varying their sizes and diameters, creating a broad range of potential uses. Metal oxides are common elements of the crust of the Earth and have long been employed in ceramics. Metal oxide semiconductors, in contrast to traditional inorganic semiconductors like silicon and III-V compounds, have distinctive thin-film properties, electrical configurations, charge transport behaviors, and material design

principles that enable traditional and novel functionality. Conducting oxides that are transparent, p-type and n-type semiconductors used in electronic devices, developments in printable metal oxide electronics, and amorphous oxide semiconductors commercialization for technologies like flat-panel display are all results of recent progress in metal oxide semiconductors.

Table 1.2. Comparison of direct band gap metal oxides needed for optical properties.

Parameter	**Zinc Oxide (ZnO)**	**Copper Oxide (CuO)**	**Magnesium Oxide (MgO)**	**Nickel Oxide (NiO)**	**Iron Oxide (Fe_3O_4)**
Crystal Structure	Hexagonal	Monoclinic	Cubic	Cubic	Cubic
Melting Point(^{0}C)	1975 ℃	1326℃	2825℃	1900 ℃	1593℃
Sintering Temperature	600-1000℃	700-900℃	1500-1800℃	300-700℃	1100℃
Optical Band Gap (eV)	3.36 eV	1.2 eV	2.9 eV	3.6-4.0 eV	1.82eV
Type of Band Gap	Direct	Direct	Direct	Indirect	Indirect
Refractive Index	2.00	1.4	1.73	2.82	2.34
References	[39, 40]	[41-43]	[44-46]	[47, 48]	[49, 50]

1.3.1. Optical Band Gap

The optical band gap is a special feature of semiconductor materials that describes the smallest amount of energy needed for a substance to absorb a photon [51,52]. This gap regulates which wavelengths of light a material can absorb or transmit, determining its optical properties and applications. It has a critical role in shaping how a material interacts with light. Direct and indirect are the two kinds of optical band gaps

represented graphically in Fig 1.6. In direct band gap, an electrons and holes have the same crystal momentum in the valence and conduction bands. At the same momentum value, the valence band's top and the conduction band's bottom occur. A photon can be directly emitted by an electron. Band gap that is indirect, the valence and conduction bands, electrons and holes have different crystal momentum. The valence band's maximal energy happens at a different momentum value. When electrons absorb energy, their momentum changes and their frequency and wavelength deviate. For grow light spectra, direct band gap material is required.

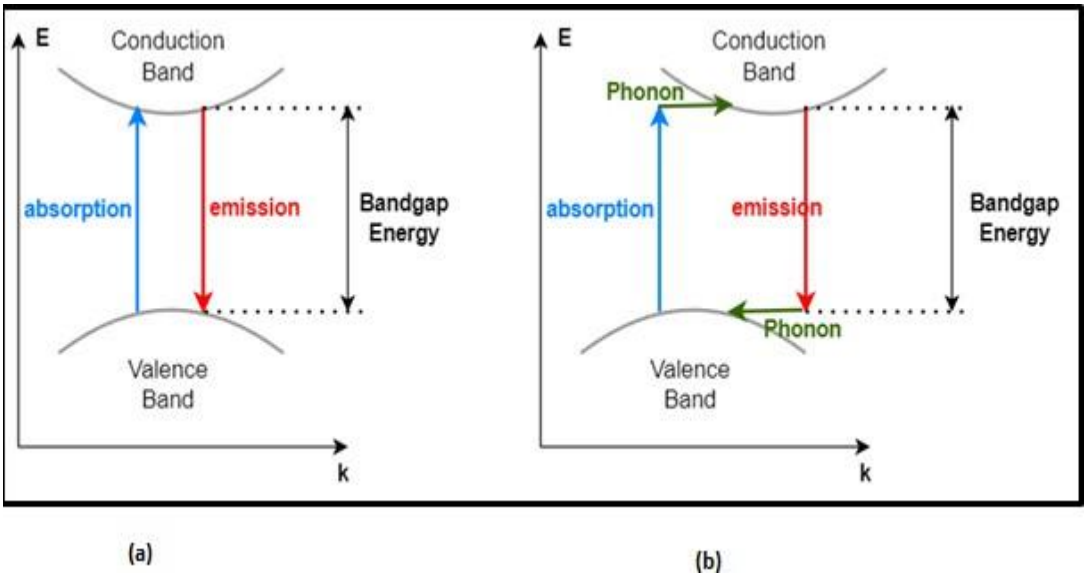

Fig. 1.6. Graphical representation of two types of band gap: (a) Direct & (b) Indirect.

Numerous theoretical and experimental techniques have been used to study optical band gaps in metal oxides. In transition metal oxides, band gaps along with dopant state energies have been determined by using OS-CDFT (oxidation-state constrained density functional theory) which has shed light on the material's electronic structures [53].

1.4. Requirement of phosphor for grow light

1. Excitation spectral requirement for grow light

Phosphor should absorb the light in UV and blue regions (200-500) nm. In a direct band gap semiconductor, the conduction band’s minimum and valence band’s

maximum energy state occurs at the same momentum (k-vector). This characteristic allows for direct electronic transitions between these states making the material highly efficient for processes involving light absorption and emission.

1. **Emission spectral Range required for grow light**

The light spectrum as discussed in section 1.1 should mainly focus on wavelengths between 400 nm and 700 nm, including both blue (400-500 nm) and red (600-700 nm) light called Photosynthetically Active Radiation (PAR), which are most effective for photosynthesis.

2. **CIE-coordinates required for grow light**

Grow lights' color characteristics are represented by their CIE coordinates based on the CIE 1931 color space. CIE 1931 coordinates are important factors to consider when assessing light sources used to describe and investigate light's color characteristics [54-56]. Ideally, the coordinates required for grow light should lie in the purple region as shown in figure 1.7.

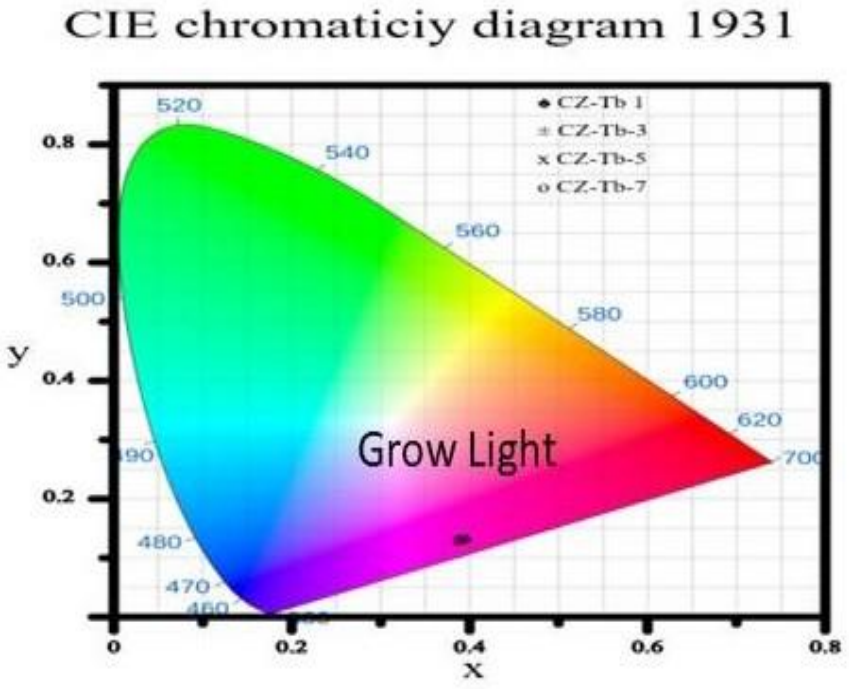

Fig 1.7. Color Chromaticity Coordinates for Grow Light Applications.

1.5. The Grow Light Phosphor Schemes

The Grow light Phosphor can be produced by the following two schemes:

(i) Red and blue phosphors excited by UV light produce grow light spectra as shown in Fig 1.2.

(ii) Red phosphors are excited by blue light, and the remaining blue light combines with the red light emitted from the phosphor to create grow light as shown in Fig 1.2.

1.6. Metal oxide nanocomposites

Metals are incorporated at the nanoscale into strong matrices, which are then engineered to increase their stability and give the matrix itself certain functions. These are called metal nanocomposites. In this, the metal matrix is supplemented with nanoparticles which results in improved mechanical, electrical, and thermal properties [57, 58]. Because of their increased strength, stiffness, and resistance to wear, these composites are used in the biomedical, automotive, and aerospace industries. Metal oxide material nanocomposites have potential uses in solar cells, batteries, sensors, photodetectors, photocatalysis, lasers, and light-emitting diodes, they have garnered a lot of interest [59]. Moreover, nanocomposites present new business and technological potential for a range of sectors. Two metal oxides combined in a common matrix to form multiphase nanocomposites have been created for a different application such as photocatalytic reactions and antibacterial qualities. Such metal oxide nanocomposites include CuO-ZnO, TiO_2-WO_3, ZnO-MgO, ZnO-NiO and Co_3O_4-ZnO [60-64] combinations, which have been produced and examined using various methods to explore their possible applications. When nanomaterials are confined, they exhibit a changeable band gap that may be precisely adjusted by managing the diameters of the particles. But the band gap is not the sole parameter that matters for many applications in different fields. Oxidative and reductive powers of holes and electrons, respectively, are defined by absolute positions of conduction and valence band edges concerning the vacuum energy. Therefore, detailed understanding of phenomena such as electrocatalysis or photocatalysis is only

possible when these essential facts are obtained, either through computational or experimental means. It is evident that the oxidative power of electrons in conduction bands and that of holes in the valence band differs significantly throughout semiconductors; as a result, the band edges can be tuned to alter the redox activity of the semiconductors [65].

In this study, we explored various metal oxide nanocomposites mentioned in Fig 1.8 to identify the most suitable host materials for grow light applications. The selected metal oxides were evaluated based on their optical properties, stability, and ability to enhance photosynthesis in plants.

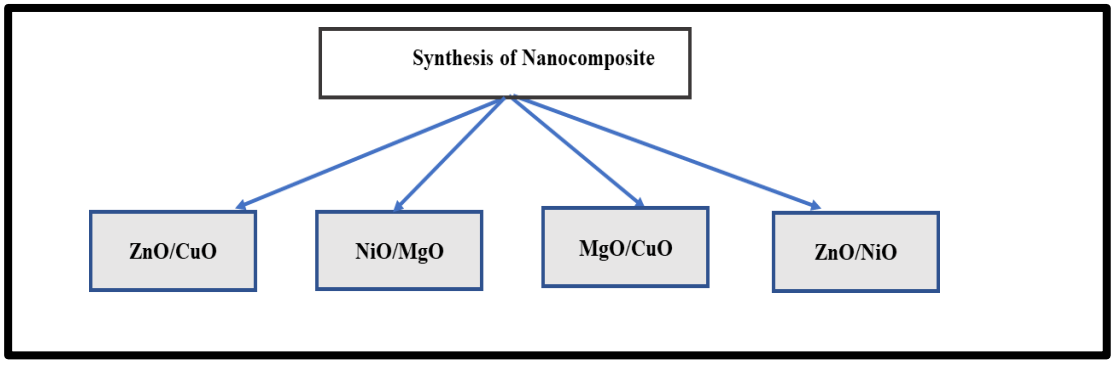

Fig 1.8. Schematic representation of the nanocomposite studied for grows light applications.

1.6.1 Rare Earth and transition metal for luminescent properties

Rare earth elements (REEs) and transition metals play important functions in luminous materials, which are used in displays, lighting, and optical systems. Rare earth elements (REEs) include the 15 lanthanides, scandium, and yttrium, which are frequently classified together due to their comparable chemical properties [66]. These elements are distinguished by partially filled f-orbitals, which play a major role in their peculiar optical and electrical properties. Rare earth elements have outstanding luminous qualities, making them useful for various purposes, for instance, phosphor. Because of their electronic structure and capacity for electronic transitions, rare earth elements have special luminous qualities that make them invaluable in a variety of technological applications. New compounds and matrices are continuously being

investigated for improvement in their luminous efficiency and increasing their usefulness in contemporary technology.

Important features of their luminous behavior include:

1. Rare earth ions f-electrons undergo electronic transitions, leading to strong emission lines. This produces unique colors, making them appropriate for colorimetric applications.
2. Rare earth ions have low non-radiative transition probabilities, resulting in excited states with lengthy lifetimes. This characteristic is useful for applications that require persistent luminescence.
3. Rare earth ions absorb and transfer energy, leading to efficient excitation from a host matrix. This ability is essential for improving luminous characteristics in a variety of materials.
4. Rare earth minerals luminescence is temperature sensitive, making them suitable for thermometry and sensing applications.
5. By incorporating different rare earth ions in a phosphor matrix, a variety of luminous hues can be produced. This adaptability is utilized in lighting and display technology.

The d-block of the periodic table contains transition metals, which act as a link between metals and non-metals. Some of these metals, such [Ar] $4s^2$ $3d^{1-10}$, have unusual electronic configurations. They can be used in many applications because their partially filled d-orbitals provide several oxidation states and a broad spectrum of reactivity. Transition metals are often used as dopants in phosphor materials. Dopants like Cr^{3+}, Fe^{3+}, Co^{3+}, Ni^{3+}, and Cu^{3+} are frequently employed [67]. By adding impurity levels, doping with these metals improves the absorption and conductivity of the host material and can change its optical (absorption, luminescence, band gap), electrical, and magnetic properties. When metal ions or complexes go from an excited state to their ground state, they emit electromagnetic radiation, which is the cause of luminosity in transition metals.

Key characteristics of transition metals are summarized as follows:

1. Reactivity and color: Transition metals are characterized by their reactivity, which can result in the creation of colored ions due to their varied oxidation states.
2. Hardness and Density: In general, they have large densities and are hard.
3. High Melting/ Boiling Points: They have high melting as well as high boiling points.
4. Coordination Numbers: Because of their partially filled d-orbitals, they can form stable compounds with a variety of coordination geometries. Their coordination numbers range from 1 to 12.
5. Colorful Complexes: The complexes are colored, with distinct colors originating from electronic transitions in the d-orbitals when certain light wavelengths are absorbed and emitted.
6. Strong metallic bonding: Transition metals have Strong metallic bonds inside their crystal structures, which enhances their stability and physical characteristics. These qualities emphasize special and adaptable transition metals for different purposes.

In the current investigation Tb, a rare-earth element, and cobalt were doped in a nanocomposite of CuO/ZnO nano phosphors. Rare-earth ions typically enter lattices in the (+3) state, as seen in the transition lines of Tb^{3+} are shown in Fig 1.9 are known to emit visible radiation in the green region. Trivalent Tb ions provide optical devices in blue and green color regions and have been expected as one of the promising species and have been reported in several compounds. These investigations demonstrate how rare earth dopants can be used to modify material properties to suit a wide range of technological needs. Dependent upon concentration, lattice distortions and changes in optical characteristics were observed due to Tb doping in CuO/ZnO nanophosphors. The emission is stimulated by 210 nm radiation.

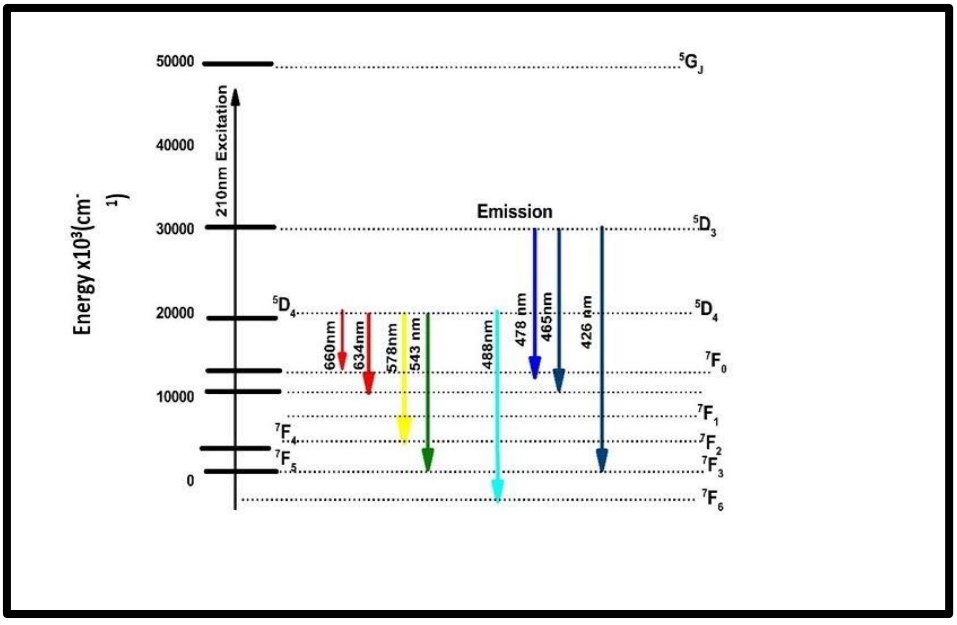

Fig 1.9. Energy level diagram of terbium Tb^{3+}

In the case of Cobalt (Co^{3+}) D_6 and D_5 configurations are responsible for the exhibition of transition that results in the absorption and emission in the UV- Vis spectrum. The absorption near the blue and green regions of the visible region is due to the D_6 configuration or low spin Co^{3+} ions and absorption in the IR and red region is due to the D_5 configuration or high spin of Co^{3+} ions as shown in Fig 1.10. Along with this emission takes place after ions get excited and relaxed, and typical emission of Co^{3+} ions take place in visible and IR regions owed to the 4T1(4P) →4A2 and 4T1(4F) →4A1.The corresponding wavelengths of these transitions vary and depend on the specific host or cobalt complex. [68]

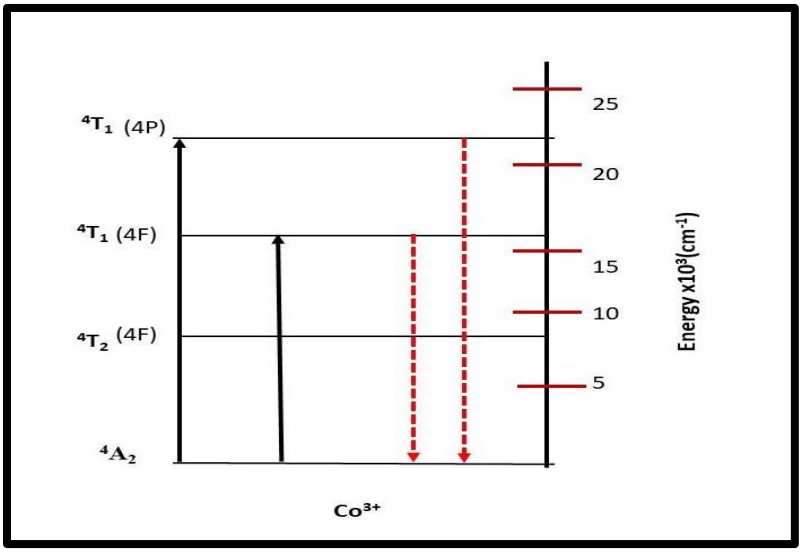

Fig 1.10. Energy level diagram of Cobalt Co^{3+}

1.7 Research motivation

There are serious environmental problems because of the growing quantity of kitchen garbage, especially in cities. Conventional methods of managing trash frequently result in contamination and the depletion of resources. As the world becomes more conscious of sustainability, it is critical to investigate novel approaches to resource recovery and waste reduction. Green synthesis is a promising technique that turns trash into valuable products using environmentally friendly procedures. We can reduce trash and turn organic materials into valuable resources for products like grow lights by using kitchen waste as a raw material. His research attempts to find novel ways to convert kitchen trash into high-performing materials, supporting agricultural productivity and environmental sustainability.

Our goal is to maximize the performance of these materials in grow light systems by creating nanocomposites and optimizing critical parameters like color space coordinates. This research offers a deeper understanding of the important optical properties of metal oxides by a thorough examination of their luminous behavior. It also shows that these materials have the potential to be used in a wider range of optical devices, especially grow lights. Using green synthesis approaches, metal oxide

nanoparticles and their composites are synthesized and characterized for the work. Advanced characterization techniques like field emission scanning electron microscopy (FE-SEM), fluorescence spectroscopy, Fourier transform infrared spectroscopy (FTIR), and X-ray diffraction (XRD) are used to assess the produced materials after they are sintered. These methods help in evaluating the materials' optical characteristics and structural soundness, emphasizing their suitability for application in energy-efficient lighting systems for the growth of plants.

1.7.1. Work Plan

Metal oxides have special properties which account for their wide range of applications. Based on these characteristics, metal oxides were chosen for the current study, which studied their optical properties for solid-state grow light sources. This study documented the synthesis and characterization of nano-sized metal oxides and nanocomposites, as shown in Fig 1.11. Among a wide family of metal oxides, we choose to synthesize ZnO, CuO, NiO, MgO, and Fe_3O_4 by green synthesis method and observe the effect on their optical properties for studying applications of grow light. Among the large family of metal oxide nanoparticles ZnO, CuO, NiO, MgO, and Fe_3O_4 have been under intense investigation for the last few years. Further, metal oxide nanoparticles display high mechanical stability due to low surface energy in comparison to their bulk counterparts. Bulk metallic oxides having well-defined crystal structures are robust and stable. They also display unique structural and optical properties which can be tuned by quantum size effect and structural modification. In addition, oxygen vacancies should have a specific effect on optical properties. In this research, we investigated various metal oxides to identify the most suitable option for optimizing on-grow light applications. These materials are useful in variety of applications due to their incongruent melting, optical, and stability features. The green synthesis approach was used to develop both doped and dopant-free materials. Sintering and different procedures for characterization, such as field emission scanning electron microscopy (FE-SEM), Fluorescence spectroscopy, UV absorption Spectroscopy, Fourier transform infrared spectroscopy (FTIR), X-ray diffraction

(XRD) are employed to evaluate both the material's structural and optical properties.

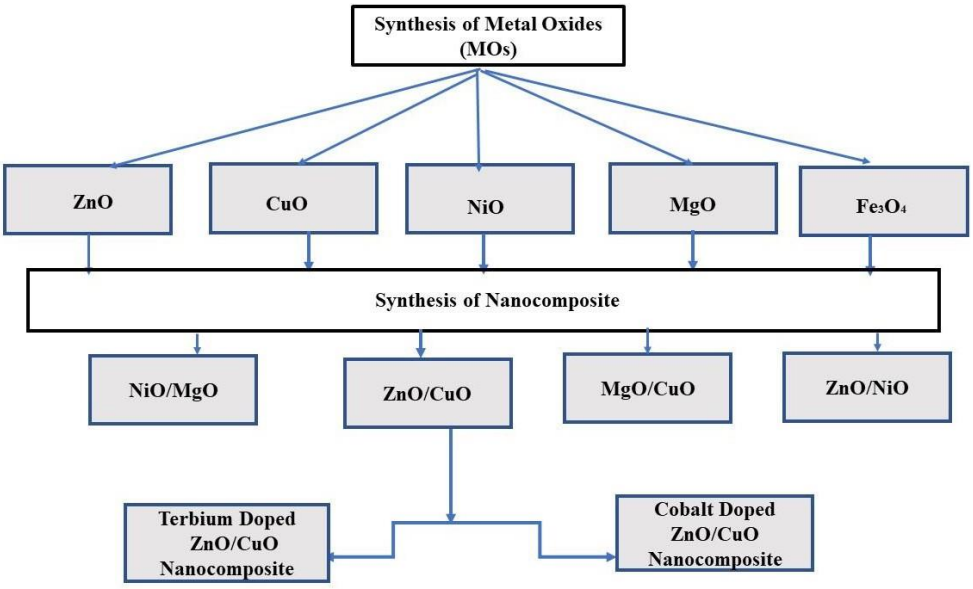

Fig 1.11. Research Work Plan for the synthesis of metal oxides for application of Grow Light.

1.7.2. Research Objectives

Both blue and red light are necessary for the growth of plants in various aspects, however, for the plants which are adapted to growing places with low light conditions or places with lesser daylight hours, there is a need to increase the blue light ratio for optimal growth of such plants throughout the year. Hence, the research objectives have been designed as follows:

1. Green metal oxides synthesis by using plant, fruit, and vegetable waste.
2. Tuning of Energy band gap of metal oxide for grow light.
3. Characterization of the material to study the impact of mixing metal oxide on structural and luminescent properties.
4. Qualitative analysis of the metal oxide and metal oxide composite for the grow light.

References:

1. M. Thakur, and R. Kumar, "Microclimatic buffering on medicinal and aromatic plants: A review," Industrial Crops and Products **160**, 113144 (2020).
2. B.W. Pratima, F. Glenn, W. Atmadja, S. Liawatimena, and R. Susanto, "Design and implementation of artificial grow light for germination and vegetative growth," IOP Conference Series Earth and Environmental Science **426**(1), 012144 (2020).
3. D.C.J. Neo, M.M.X. Ong, Y.Y. Lee, E.J. Teo, Q. Ong, H. Tanoto, J. Xu, K.S. Ong, and V. Suresh, "Shaping and tuning lighting Conditions in Controlled Environment Agriculture: A review," ACS Agricultural Science & Technology **2**(1), 3–16 (2022).
4. M. Pessarakli, "Plant responses to extended Photosynthetically active radiation (EPAR)," Advances in Plants & Agriculture Research **7**(3), (2017).
5. G.-W. Bang, and Y.-H. Kim, "LED for plant growth regulators for the study of Light on the device," Journal of Digital Convergence **10**(7), 267–272 (2012).
6. E.G. Kulikova, S.Yu. Efremova, N. Politaeva, and Y. Smyatskaya, "Efficiency of an alternative LED-based grow light system," IOP Conference Series Earth and Environmental Science **288**(1), 012064 (2019).
7. H.M. Wollaeger, and E.S. Runkle, "Growth responses of ornamental annual seedlings under different wavelengths of red light provided by light-emitting diodes," HortScience **48**(12), 1478–1483 (2013).
8. G. Proksch, *Creating Urban Agricultural Systems: An Integrated Approach to Design* (2016).
9. S.E. Bilodeau, B.-S. Wu, A.-S. Rufyikiri, S. MacPherson, and M. Lefsrud, "An update on plant photobiology and implications for cannabis production," Frontiers in Plant Science **10**, (2019).
10. K.J. McCree, "The action spectrum, absorptance and quantum yield of photosynthesis in crop plants," Agricultural Meteorology **9**, 191–216 (1971).
11. A.A. Kalabkin, E.A. Kuznetsov, S.N. Ivliyev, A.A. Ashryatov, V.A. Kalabkin,

and A.S. Musatov, “The development of LED grow light for greenhouse cultivation,” Engineering Technologies and Systems **4**(33), 585–598 (2023).

12. D.C.J. Neo, M.M.X. Ong, Y.Y. Lee, E.J. Teo, Q. Ong, H. Tanoto, J. Xu, K.S. Ong, and V. Suresh, “Shaping and tuning lighting Conditions in Controlled Environment Agriculture: A review,” ACS Agricultural Science & Technology **2**(1), 3–16 (2022).
13. G. Massa, J.C. Emmerich, R. Morrow, C. Bourget, and C. Mitchell, “Plant-growth lighting for space life support: a review.” Gravitational and space biology, **19**(2), 19-30 (2007).
14. S.D. Gupta, and A. Agarwal, “Artificial lighting system for plant growth and Development: chronological advancement, working principles, and comparative assessment,” Light Emitting Diodes for Agriculture: Smart Lighting, 1–25 (2017).
15. P. Dąbrowski, M. Kusaka, and I.A. Samborska, “Measuring light spectrum as a main indicator of artificial sources quality,” Journal of Coastal Life Medicine **3**(5), (2015).
16. B.-S. Wu, A.-S. Rufyikiri, V. Orsat, and M.G. Lefsrud, “Re-interpreting the photosynthetically action radiation (PAR) curve in plants,” Plant Science **289**, 110272 (2019).
17. A. Kutschera, and J.J. Lamb, “Light meter for measuring photosynthetically active radiation,” American Journal of Plant Sciences **09**(12), 2420–2428 (2018).
18. E. Młodzińska, “Survey of plant pigments: molecular and environmental determinants of plant colors.,” Acta Biologica Cracoviensia S Botanica **51**(1), 7–16 (2009).
19. T. Tan, S. Li, Y. Fan, Z. Wang, M.A. Raza, I. Shafiq, B. Wang, X. Wu, T. Yong, X. Wang, Y. Wu, F. Yang, and W. Yang, “Far-red light: A regulator of plant morphology and photosynthetic capacity,” The Crop Journal **10**(2), 300–309 (2021).
20. V.P. Aswathi, S. Meera, C.G.A. Maria, and M. Nidhin, “Green synthesis of nanoparticles from biodegradable waste extracts and their applications: a critical

review," Nanotechnology for Environmental Engineering **8**(2), 377–397 (2022).

21. A. Gour, and N.K. Jain, "Advances in green synthesis of nanoparticles," Artificial Cells Nanomedicine and Biotechnology **47**(1), 844–851 (2019).
22. P. Kuppusamy, M.M. Yusoff, G.P. Maniam, and N. Govindan, "Biosynthesis of metallic nanoparticles using plant derivatives and their new avenues in pharmacological applications – An updated report," Saudi Pharmaceutical Journal **24**(4), 473–484 (2014).
23. D. Strong, K. Heneman, S. Zidenberg-Cherr, B. Halliwell, J. Gutteridge, A. Kaulmann, T. Bohn, A. Adlercreutz, F. Kiuchi, Y. Goto, N. Sugimoto, B. Aggarwal, and K. Harikumar, "Aspects of Nutrition," Phytonutrients (2021).
24. H.B.H. Rahuman, R. Dhandapani, S. Narayanan, V. Palanivel, R. Paramasivam, R. Subbarayalu, S. Thangavelu, and S. Muthupandian, "Medicinal plants mediated the green synthesis of silver nanoparticles and their biomedical applications," IET Nanobiotechnology **16**(4), 115–144 (2022).
25. S. Ying, Z. Guan, P.C. Ofoegbu, P. Clubb, C. Rico, F. He, and J. Hong, "Green synthesis of nanoparticles: Current developments and limitations," Environmental Technology & Innovation **26**, 102336 (2022).
26. Md.R. Islam, Md.M. Kamal, Md.R. Kabir, Md.M. Hasan, A.R. Haque, and S.M.K. Hasan, "Phenolic compounds and antioxidants activity of banana peel extracts: Testing and optimization of enzyme-assisted conditions," Measurement Food **10**, 100085 (2023).
27. H.T. Vu, C.J. Scarlett, and Q.V. Vuong, "Phenolic compounds within banana peel and their potential uses:A review,"Journal of Functional Foods **40**, 238–248 (2017).
28. M. Friedman, N. Kozukue, H.-J. Kim, S.-H. Choi, and M. Mizuno, "Glycoalkaloid, phenolic, and flavonoid content and antioxidative activities of conventional nonorganic and organic potato peel powders from commercial gold, red, and Russet potatoes," Journal of Food Composition and Analysis **62**, 69–75 (2017).

29. W. Hidayat, I. Sufiawati, M. Satari, R. Lesmana, and S. Ichwan, “Pharmacological Activity of Chemical Compounds of Potato Peel Waste (Solanum tuberosum L.) in vitro: A Scoping Review,” Journal of Experimental Pharmacology **16**, 61–69 (2024).
30. J.R. Fahim, E.Z. Attia, and M.S. Kamel, “The phenolic profile of pea (Pisum sativum): a phytochemical and pharmacological overview,” Phytochemistry Reviews **18**(1), 173–198 (2018).
31. L. Castaldo, L. Izzo, A. Gaspari, S. Lombardi, Y. Rodríguez-Carrasco, A. Narváez, M. Grosso, and A. Ritieni, “Chemical Composition of Green Pea (Pisum sativum L.) Pods Extracts and Their Potential Exploitation as Ingredients in Nutraceutical Formulations,” Antioxidants **11**(1), 105 (2021).
32. J. Singh, T. Dutta, K.-H. Kim, M. Rawat, P. Samddar, and P. Kumar, “‘Green’ synthesis of metals and their oxide nanoparticles: Applications for environmental remediation,” Journal of Nanobiotechnology **16**(1), (2018).
33. K. Illath, S. Wankhar, L. Mohan, M. Nagai, and T.S. Santra, “Metallic nanoparticles for biomedical applications,” Springer Series in Biomaterials Science and Engineering, 29–81 (2021).
34. G. Priyadarshana, N. Kottegoda, A. Senaratne, A. De Alwis, and V. Karunaratne, “Synthesis of Magnetite Nanoparticles by Top-Down Approach from a High Purity Ore,” Journal of Nanomaterials **2015**(1), (2015).
35. M. Rawat, J. Singh, and H. Kaur, “A uncanny potential of plants for metal nanoparticles synthesis,” Journal of Nanomedicine Research **7**(2), (2018).
36. Y. Yoon, P.L. Truong, D. Lee, and S.H. Ko, “Metal-Oxide nanomaterials synthesis and applications in flexible and wearable sensors,” ACS Nanoscience Au **2**(2), 64–92 (2021).
37. M.L. Grilli, “Metal oxides,” Metals **10**(6), 820 (2020).
38. K. Narasimharao, and T.T. Ali, “Influence of synthesis conditions on physico-chemical and photocatalytic properties of rare earth (Ho, Nd and Sm) oxides,” Journal of Materials Research and Technology **9**(2), 1819–1830 (2019).

39. M.W. Aladailah, O.L. Tashlykov, T.P. Volozheninov, D.O. Kaskov, K.S. Iuzbashieva, R. Al-Abed, A. Acikgoz, N. Yorulmaz, M.M. Yaşar, W. Al-Tamimi, and M. Alshipli, "Exploration of physical and optical properties of ZnO nanopowders filled with polydimethylsiloxane (PDMS) for radiation shielding applications. Simulation and theoretical study," Optical Materials **134**, 113197 (2022).
40. N. Mursal, N. Irhamni, N. Bukhari, and Z. Jalil, "Structural and Optical Properties of Zinc Oxide (ZnO) based Thin Films Deposited by Sol-Gel Spin Coating Method," Journal of Physics Conference Series **1116**, 032020 (2018).
41. G.G. Welegergs, R. Akoba, J. Sacky, and Z.Y. Nuru, "Structural and optical properties of copper oxide (CuO) nanocoatings as selective solar absorber," Materials Today Proceedings **36**, 509–513 (2020).
42. S. Saleem, A.H. Jabbar, M.H. Jameel, A. Rehman, Z.H. Kareem, A.H. Abbas, Z. Ghaffar, S.A. Razzaq, R.A. Pashameah, E. Alzahrani, E.-P. Ng, and S.M. Sapuan, "Enhancement in structural, morphological, and optical properties of copper oxide for optoelectronic device applications," Nanotechnology Reviews **11**(1), 2827–2838 (2022).
43. PubChem, "Copper oxide," PubChem, (n.d.).
44. G. Balakrishnan, R. Velavan, K.M. Batoo, and E.H. Raslan, "Microstructure, optical and photocatalytic properties of MgO nanoparticles," Results in Physics **16**, 103013 (2020).
45. M.A. Asl, M.R. Benam, R.P. Shahri, A. Feyzi, and F. Kafi, "Two-dimensional quantum confinement effects on thermoelectric properties of MgO monolayers: A first principle study," Micro and Nanostructures **163**, 107134 (2021).
46. PubChem, "Magnesium oxide," PubChem, (n.d.).
47. S. Yousaf, S. Zulfiqar, M.N. Shahi, M.F. Warsi, N.F. Al-Khalli, M.F.A. Aboud, and I. Shakir, "Tuning the structural, optical and electrical properties of NiO nanoparticles prepared by wet chemical route," Ceramics International **46**(3), 3750–3758 (2019).

48. G.A. El-Shobaky, I.F. Hewaidy, and Th. El-Nabarawy, “Sintering of non-stoichiometric NiO, CoO and Co3O4 catalysts,” Surface Technology **12**(4), 309–315 (1981).
49. I. Sulania, J. Kaswan, V. Attatappa, R.K. Karn, D.C. Agarwal, and D. Kanjilal, “Investigations of electrical and optical properties of low energy ion irradiated α-Fe2O3 (hematite) thin films,” AIP Conference Proceedings, (2016).
50. T. Saragi, A.S. Santika, B. Permana, N. Syakir, M. Kartawidjaja, and N. Risdiana, “Synthesis and properties of iron oxide particles prepared by hidrothermal method,” IOP Conference Series Materials Science and Engineering **196**, 012025 (2017).
51. P. Makuła, M. Pacia, and W. Macyk, “How to correctly determine the band gap energy of modified semiconductor photocatalysts based on UV–VIS spectra,” The Journal of Physical Chemistry Letters **9**(23), 6814–6817 (2018).
52. A. Dolgonos, T.O. Mason, and K.R. Poeppelmeier, “Direct optical band gap measurement in polycrystalline semiconductors: A critical look at the Tauc method,” Journal of Solid-State Chemistry **240**, 43–48 (2016).
53. C. Ku, and P.H. Sit, “Evaluation of optical band gaps and dopant state energies in transition metal oxides using oxidation-state constrained density functional theory,” Journal of Physics Condensed Matter **33**(36), 365901 (2021).
54. J. Schanda, “CIE u′, v′ Uniform Chromaticity Scale Diagram and CIELUV Color Space,” in *Springer eBooks*, (2016), pp. 185–188.
55. C.-C. Lin, and K.-C. Huang, “Effects of Color Combination and Ambient Illumination on Visual Perception Time with TFT-LCD,” Perceptual and Motor Skills **109**(2), 607–625 (2009).
56. Y. Park, and E.S. Runkle, “Spectral effects of light-emitting diodes on plant growth, visual color quality, and photosynthetic photon efficacy: White versus blue plus red radiation,” PLoS ONE **13**(8), e0202386 (2018).
57. S. Vb, “An overview on the preparation, Characterization and properties of Electrodeposited-Metal Matrix Nanocomposites,” Nanoscience & Technology

Open Access **1**(3), (2014).

58. M. Malaki, W. Xu, A. Kasar, P. Menezes, H. Dieringa, R. Varma, and M. Gupta, "Advanced Metal Matrix Nanocomposites," Metals **9**(3), 330 (2019).
59. R.R. Kumar, K.U. Kumar, and D. Haranath, "Synthesis, characterization, and applications of ZnO–TiO2 nanocomposites," Elsevier eBooks, 271–314 (2022).
60. A.G. Bekru, L.T. Tufa, O.A. Zelekew, M. Goddati, J. Lee, and F.K. Sabir, "Green synthesis of a CUO–ZNO nanocomposite for efficient photodegradation of methylene blue and reduction of 4-Nitrophenol," ACS Omega **7**(35), 30908–30919 (2022).
61. Z. Zahid, S. Saeed, S. Arif, M. Waseem, S. Haq, A. Syed, F. Menaa, A.H. Bahkali, and L.S. Wong, "Green synthesis of NIO/ZNO nanocomposites for the adsorption of various dyes," Materials Research Express **11**(3), 035007 (2024).
62. A. Bojinova, N. Kaneva, K. Papazova, A. Eliyas, E. Stoyanova-Eliyas, and D. Dimitrov, "Green synthesis of UV and visible light active TiO2/WO3 powders and films for malachite green and ethylene photodegradation," Reaction Kinetics Mechanisms and Catalysis **120**(2), 821–832 (2017).
63. J. Pachiyappan, N. Gnanasundaram, and G.L. Rao, "Preparation and characterization of ZnO, MgO and ZnO–MgO hybrid nanomaterials using green chemistry approach," Results in Materials **7**, 100104 (2020).
64. P. Dwivedi, H. Satiya, and S.K. Sharma, "Novel green approach for the synthesis of Co3O4/ZnO nanocomposite, characterization and antimicrobial activity," Materials Today Proceedings **79**, 80–86 (2022).
65. M. Bredol, K. Matras, A. Szatkowski, J. Sanetra, and A. Prodi-Schwab, "P3HT/ZnS: A new hybrid bulk heterojunction photovoltaic system with very high open circuit voltage," Solar Energy Materials and Solar Cells **93**(5), 662–666 (2009).
66. J. Lucas, P. Lucas, T.L. Mercier, A. Rollat, and W. Davenport, "Introduction to rare Earth luminescent materials," Elseiver, 251–280 (2015).
67. S.M.U. Hassan, W. Akram, A. Noureen, F. Ahmed, A. Hassan, and A. Ullah,

"Advances in transition metals and rare earth elements doped ZnO as thermoluminescence dosimetry material," Radiation Physics and Chemistry **223**, 111929 (2024).

68. B. Suresh, M.S. Reddy, J. Ashok, A.S.S. Reddy, P.V. Rao, V.R. Kumar, and N. Veeraiah, "Enhancement of orange emission of Co 2+ ions with Bi 3+ ions in lead silicate glasses," Journal of Luminescence **172**, 47–52 (2015).

Chapter 2

REVIEW OF LITERATURE

The following review has discussed the approach of green synthesis and characterization of different metal oxides and related nanocomposites with a focus on the application of various techniques to examine their structural, optical, and chemical characteristics. Additionally, this review also provides insights into their possible applications in a variety of industries. The review has also examined the processes and outcomes of both green and chemical methods, offering insights into their environmental impact, efficiency, and practicality.

Barzegar et al. (2024) used the sol-gel technique to create magnesium oxide nanoparticles (MgO-NPs) from a plant extract called *Caccinia macranthera*. UV-Vis spectra upon characterization showed a band of absorption at 357 nm, while XRD examination revealed it to be cubical along with 34nm as the average crystal size. Existence of elements like oxygen and magnesium was confirmed by EDX, and spherical nanoparticles were visible in FESEM pictures. Functional molecules indulged in the production of nanoparticles were seen by FTIR analysis. MgO-NPs, then, were assessed for their cytotoxicity against cancer cells Huh-7, demonstrating IC50 value 223 μg/mL. Then, after 120 minutes, MgO-NPs showed strong photocatalytic activity, reducing methylene blue by 87% [1].

Dat et al. (2024) used *Mangifera Indica* aqueous abstract in the study. It was used as a reducing agent to create nanoparticles of copper oxide, or CuONPs. Particle sizes ranged widely, from 20 to 80 nm as found during characterization. Also, a zeta potential of 40.5 mV was found to have good stability. CuONPs showed superior photocatalytic breakdown of malachite green dye, sustaining performance throughout five recycling cycles and achieving 95.39% efficiency under the visible light spectrum. CuONPs also showed good antimicrobial activity against different bacteria and its effect was even better in the presence of light than in the absence of it. According to these findings, applications involving environmental remediation show promise for green-synthesized CuONPs [2].

Duan et l. (2024) use leaf extract from *Nicotiana plumbaginifolia* (NiP) for synthesis of nanoparticles of iron oxide in an environmentally friendly manner. The results were analyzed by SEM, UV, TGA/DSC and FTIR. Significant zones of inhibition showed that FeO_NPs had high antibacterial efficacy against Pseudomonas aeruginosa, Bacillus subtilis, Escherichia coli, and Staphylococcus aureus. Using the DPPH test, they showed antioxidant activity by capturing up to 80% of free radicals. FeO NPs also demonstrated the ability to bind DNA and bovine serum albumin (BSA), with up to 50% binding capability, indicating that they are acceptable for use in medical applications [3].

Idris et al. (2024) addressed issues brought on by the huge mass as well as the radius of sodium ions by investigating the usage of nanoparticles of zinc oxide (ZnO-NPs) as the anodes in sodium-ion batteries (SIBs). This green synthesis approach, which uses leaf extract of MCV, is a safe and affordable substitute for chemical synthesis. Alkaloids, flavonoids, and phenols are present in MCV. ZnO-NP formation was verified by FTIR and X-ray diffraction following the calcination at 700, 800, and 900°C. SEM revealed agglomerated, irregularly shaped particles with 38–65 nm particle diameters. Higher temperatures resulted in reduced pore size and volume through nitrogen gas adsorption. ZnO-NPs with a 700°C calcine showed good discharge power initially, suggesting that they could be used as silicon-ion battery anodes [4]

Islam et al. (2024), as a more environmentally friendly option to complicated organic HTLs, used aloe vera (AV) leaf extract for green synthesis of NiOx thin films for perovskite solar cells (PSCs). Three different calcination temperatures—300, 400, and 500 degrees Celsius—were investigated. Higher temperatures were shown to have better crystallinity by XRD examination, and EDX and Raman spectroscopy showed minimal carbon content. At 300°C, the good morphology was confirmed by FESEM pictures. The band gap changed as the temperature rose, moving from 3.83 eV to 3.73 eV. At 500°C (20.3 cm^2/Vs), electrical characterization revealed the maximum hole mobility. The PCE, Voc, and FF values that peaked at 500°C (16.04%, 1.70 V, and

67.35%) were revealed via numerical simulation, while Jsc peaked at 300°C (14.95 mA/cm²) [5].

Prabu and Losetty (2024) used *Macroptilium lathyroides* for creating nanoparticles of Copper Oxide (CuO NPs) in an economical and environmentally friendly manner. The CuO NPs were identified by UV-visible, FTIR, SEM, XRD, TEM, and XPS techniques. Their crystallite size was 18.9 nm, and they exhibited a monoclinic structure. Under sunlight, they showed a 98% degradation of the Methylene Blue dye. Significant antibacterial (Escherichia coli and Staphylococcus aureus), antifungal (*Candida albicans* and *Trichoderma viride*), cytotoxic (IC50 = 71.02 µg/mL) and antioxidant (IC50 = 86.96 µg/mL) activity were demonstrated in biological assays. From the investigation of this synthesis copper oxide nanoparticles are used for various applications in the field of medicine and bioremediation [6].

Ali et al. (2023) used bark extract from *Abrus precatorius* L. to create magnesium oxide (MgO) nanoparticles in an environmentally friendly manner. XRD, FTIR, SEM, etc. analysis was used for describing nanoparticles of MgO. These nanoparticles demonstrated strong antioxidant and dye degradation properties, as well as remarkable free radical scavenging capabilities. The safety of MgO NPs was confirmed by the lack of toxicity observed in zebrafish eggs. Apoptosis and necrosis were seen in a typical human melanoma cell line (A375) while testing the anticancer characteristics, which were verified using genotoxicity experiments. The paper presents a green production technique and shows the prospect of MgO NPs as a therapeutic medication for melanoma cancer [7].

Ashraf et al. (2023) greenly synthesized nanoparticles of iron oxide (IO-NPs) using aqueous extract of Amla seeds. This extract functioned as a stabilizing and bio-reducing agent. The structural properties are used to analyze produced nanoparticles such as XRD, FTIR, TEM. Nanoparticles' average diameter was determined by TEM examination to be 4-5 nm. From the XRD AND FTIR, the present stabilizing and capping agents were confirmed FTIR. The elimination of Methylene Blue (MB) dye was observed using UV-Visible spectroscopy, proving that IO NPs produced from

Amla seed extract can function as an efficient catalyst for dye removal [8].

MuthuKathija et al. (2023) extracted material from leaves of *Pisonia alba w*hich is utilized as a capping and reducing agent for environmentally friendly ZnO nanoparticle production and further characterized. ZnO nanoparticle production was verified by UV-Vis. According to FTIR, the leaf extract's proteins, terpenoids, alkaloids, and phenolic chemicals, all aid in nucleation and stability. ZnO hexagonal structure (JCPDS-file: 89–1397) and lack of impurities were verified by XRD. SEM showed that the shape resembled aloe vera leaves, while XPS determined the degree of oxidation. Strong antibacterial activity was demonstrated by the ZnO nanoparticles against different bacteria [9].

Alhili (2022) used an extract from the leaves of *Eucalyptus globulus* to create nanoparticles of copper oxide. These spherical nanoparticles had a zeta potential of -16.9 mV, measuring about 88 nm, according to SEM and DLS analysis. Its crystalline and monoclinic structure, having a size of about 85.80 nm, is confirmed by XRD. Methyl orange dye was efficiently absorbed by CuO NPs, with an efficiency of 95 mg/g at pH 4.5. The model's R2 of 0.99 indicated its great accuracy [10].

Al Zaqri et al. (2022) synthesized nickel oxide nanoparticles utilizing flower extract of *Senna auriculata* in this study, and then their photocatalytic and antibacterial properties were assessed. The crystalline nature, direct bandgap of 3.25 eV, stability (53 nm, -24 mV), and area of surface analysis of nanoparticles were shown via their characterization using different techniques. HR-TEM revealed a uniformly distributed spherical structure. FTIR techniques are used to confirm the reducing and capping agents present in the sample material such as Surface proteins, carboxyl and hydroxyl groups. Antimicrobial efficacy against Escherichia coli was greater. Under visible light, catalyst activity demonstrated a 97% degradation of the methylene blue dye. *Senna auriculata* exhibits potential for manufacturing environmentally benign nanoparticles that can be used in the medical and environmental fields [11].

Kumar et al. (2022) used an extract of *Camellia sinensis* (tea leaves) as a reducing agent to present synthesis, characterization, and photocatalytic action of nanoparticles

of magnesium oxide for the first time. From the XRD the phase of MgO was confirmed as cubic phase. The crystallographic parameters were found, and lattice flaws were investigated using Rietveld refinement analysis. Lattice stress, energy density, and microstrain were computed using the Williamson-Hall method. The efficacy of the nanoparticles in breaking down the dye called methylene blue was over 97%. Its degradation is due to O radicals that develop on the MgO (001) surface, according to density functional theory (DFT) calculations [12].

Rafique et al. (2022) used leaf extract from *Syzygium cumini* to synthesize zinc oxide using a green synthesis method. The synthesis was validated by UV-Visible spectroscopy, and the crystalline hexagonal and spherical forms of nanoparticles of ZnO were disclosed by XRD and SEM, respectively. Flavonoids, phenolic acids, steroids, and enzymes were detected in the extract using Fourier-transform infrared spectroscopy; these components assisted in reducing zinc salt into ions and capping the NPs. In *Pennisetum glaucum*, the ZnO-NPs improved seed germination and successfully broke Rhodamine B dye, attaining 98% degradation. ZnO-NPs' potential for water filtration was highlighted by the study, which optimized parameters like temperature, pH, and length of light irradiation [13].

Ananthi et al. (2021) produces iron oxide nanoparticles (FeO NPs) by a green tea-mediated combustion synthesizing method. Green tea's natural tannic acid and chemical ferric nitrate are utilized in the synthesis process, which is then baked at 350°C. FeO NPs' crystal structure and phases are revealed by XRD examination; the produced sample's mean crystallite size was around 23.4 nm, whereas the sample when annealed was 30.1 nm. Shape, content was characterized by SEM and EDX, and particle size (25 nm for produced, 32 nm for annealed) is determined by TEM. Zeta potential, which has remarkable values (prepared: -58.3 in mV, annealed: -60.1 in mV for annealed) shows colloidal stability. 2.24 eV was a band gap for samples that were prepared and 2.78 eV for annealed samples are revealed by UV-Vis spectra [14].

El-Belely et al. (2021) synthesized nanoparticles of zinc oxide, which were characterized by many different techniques like EDX, XPS etc. using metabolites

from *Arthrospira platensis* microalgae. With an absorbance peak at 370 nm, cyanobacterial metabolites efficiently generated spherical ZnO-NPs with diameters ranging from 30.0 to 55.0 nm. XPS verified Zn (II)O existence, while FT-IR showed absorption peaks associated with nanoparticle production. The biosynthesized ZnO-NPs were shown to have dose-dependent antibacterial action against a range of pathogens, with minimum inhibitory concentrations (MIC values) spanning from 12.5 to 50 ppm. Furthermore, ZnO-NPs demonstrated a greater degree of cytotoxic activity (IC50 values of 9.95 ppm and 53.34 ppm, respectively) against malignant (Caco-2) cells as opposed to normal (WI38) cells [15].

Khan et al. (2021) investigated Ag@MgO nanocomposite green synthesis by employing leaf extract from *Olea cuspidata*. Its structure was discovered through characterization using HRTEM, etc. Strong antioxidant capabilities against DPPH radicals, effective photocatalytic methylene blue degradation, and antimicrobial properties against some bacterial pathogens, have been observed. Citric acid, an organic acid found in *Olea Cuspidata*, helps to stabilize the nanocomposite and improves its characteristics. The work emphasizes how green chemistry plays a special role in creating multifunctional nanoparticles for use in nanobiotechnology [16].

Sabouri et al. (2021) produced nanoparticles of nickel oxide (NiO-NPs). This was done by extracting the seeds of *Salvia hispanica* L. (chia), with an emphasis on the chemical along with the physical characteristics of particles. The NiO-NPs were characterized by spectroscopy and other studies. FESEM/PSA showed spherical particles about 30 nm in size, which EDAX corroborated by finding components of nickel and oxygen. Peaks corresponding to the crystal structure of these NPs were seen by XRD. Superparamagnetic behavior was revealed by VSM analysis, although cytotoxicity did not depend on concentration. NiO-NPs have potential for usage in different fields, such as disease prevention and toxin removal, due to their strong photocatalytic activity and low cytotoxicity [17].

Siddiqui et al. (2021) created nanoparticles of copper oxide (CuO NPs) utilizing a

low-cost, environmentally friendly sol-gel process with peel extract from *Punica granatum* as a reducing agent. When the peel extract was combined with copper acetate monohydrate, a color shift signaled the creation of nanoparticles. CuO NPs had a size of about 35.80 nm and were seen to have a crystalline, monoclinic structure, as validated by characterization methods including FTIR, SEM, and XRD. Substantial zones of inhibition in disk diffusion tests indicated that the produced nanoparticles had outstanding antibacterial effects against *Escherichia coli*, demonstrating their potential as strong antimicrobial agents [18].

Haider et al. (2020) focused on reducing chemical toxicity, especially in the textile industry, by employing extracts of ginger and garlic to create nickel oxide nanoparticles via green synthesis. Various characterization techniques were used, including UV-Vis, XRD, XPS, FTIR, EDS, SEM, and TEM. Strong absorption was seen at 350 nm in spectra of UV-Vis, and garlic and ginger particle sizes varied from 11 to 59 nm and 16 to 52 nm, respectively. The pleomorphism of the nanoparticles, which showed spherical and cubic forms, was confirmed by electron microscopy. The exact inclusion of the ginger and garlic extracts was confirmed by FTIR. NiO-NPs made from garlic demonstrated effective degradation of methylene blue dye and increased bactericidal act in contradiction of drug-resistant Staphylococcus aureus. On an industrial scale, these green-synthesized NiO-NPs have the potential to resolve drug resistance and act as environmentally benign catalysts [19].

Ifeanyichukwu et al. (2020) produced nanoparticles of ZnO, utilizing aqueous extracts from pomegranate leaves and blossoms. The antibacterial efficacy of these particles was assessed in this study. Spectroscopic methods were employed to characterize the nanoparticles. Their crystalline nature was confirmed by XRD analysis. Further, an irregular spherical shape was seen by electron microscopy. By using FTIR Spectroscopy, functional groups associated with reduction and stabilization were found. The leaf and flower extracts absorption bands are present at 284 nm and 357 nm, respectively, according to UV-Vis analysis. Significant antimicrobial activity was shown by the ZnO-NPs. To learn more about their toxicity

and modes of action, more research is required [20].

Jamzad et al. (2020) used an environmentally friendly technique to produce iron nanoparticles (α-Fe2O3) by using the leaf extract of *Laurus nobilis* L. Analyzed using techniques like TEM, XRD, EDS, etc., particles were found to be almost spherical, crystalline, and hexagon-shaped, and had size of about 8.03 ± 8.99 in nm. Tests using antimicrobial agents against *Penicillium spinulosum*, *Aspergillus flavus*, and *Listeria monocytogenes* displayed a modest level of efficacy. These green-synthesized nanoparticles have potential uses in light photocatalysis, semiconductors, and gas sensing, and can be used in antifungal and antibacterial agents [21].

Mohamed (2020) created a green way to synthesize nanoparticles of copper/copper oxide (Cu/Cu2O NPs) utilizing date extract as an agent reducing in nature since they have phenolic and flavonoid content. Spherical particles with a mean size of about 78 nm and a value of zeta potential of approximately +41 mV, suggesting good stability, were found by TEM and DLS studies. The distinctive copper peaks were validated by XRD, and a plasmonic resonance peak was detected at 576 nm by UV-Vis spectroscopy. The phenolic chemicals in charge of the reduction process were found using FTIR. This is a straightforward, economical, and eco-friendly way to create Cu/Cu2O NPs [22].

Roy et al. (2024) investigated the co-precipitation approach of synthesizing silver-copper oxide nanoparticles utilizing carica papaya fruit extract. As a reference, a silver-copper combination composite was also made using the traditional co-precipitation technique. By breaking down methylene blue dye, the materials' photocatalytic efficacy was evaluated. The composite was encapsulated using fishbone hydroxyapatite. Various characterization techniques were used, including TEM, XPS, FT-IR, SEM-EDS, and XRD. The encapsulated composites effectively destroyed other dyes, indicating their potential as potent photocatalysts, while the unencapsulated composites broke down 90.12% and 91.5% of methylene blue in 60 minutes [23].

Masho et al. (2024) focussed on employing leaf extract from *Croton macrostachyus*

to facilitate the production of ZnO, Ag2O, and CuO nanoparticles including their nanocomposites. There was no need for extra fuel during the synthesis process. PXRD, XPS, SEM, FTIR, TEM, EDX, UV-Vis spectroscopy, HRTEM, and SAED were among the characterization techniques that verified the metal ions reduction and the creation of metal oxides. All produced nanocomposites showed strong antioxidant properties scavenging 96% of free radicals of DPPH and effective photocatalytic breakdown of methylene blue dye under sunshine in 60 minutes. The study emphasizes how these ternary nanocomposites can be used effectively for antibacterial and environmental applications [24].

Varshini et al. (2024) have presented a synthetic procedure of a SnO2:Ce/rGO nanocomposite employing fruit pulp extract from *Cassia fistula* as a green reducing agent in this work. With degradation efficiencies of 97% for anionic dyes (Rose Bengal) and 98% for cationic dyes (Methylene Blue), the nanocomposite showed high photocatalytic activity. An extended hetero junction among the composite partners was visible in Transmission Electron Microscopy (TEM) pictures, which enabled desirable carrier transport and charge recombination delay. By collaborating with rGO, the nanocomposite demonstrated visible light responsiveness because of its lowered band gap. Furthermore, it demonstrated notable antioxidant activity and α-glucosidase enzyme inhibition, suggesting its potential in the biomedical applications field. [25].

Jansanthea et al. (2024) synthesized CuO/Fe2O3/ZnO (CFZ) ternary composite photocatalyst for environmentally friendly synthesis utilizing grape extract. The process incorporates grape extract as a green reducing agent along with copper acetate, zinc acetate, and ferric nitrate. The appropriate composite material is created by carefully applying microwave treatment and regulating the calcination process. Comprehensive evaluation using techniques such as UV-DRS, PL spectroscopy, XRD, FT-IR, EDXS, SEM, BET surface area analysis, and UV-DRS indicates good physical, chemical, and optical properties for effective photocatalysis. The 1.91 eV smaller bandgap of CFZ–10mc is essential for improving photocatalytic efficacy.

Evaluation of CFZ's effectiveness in decomposing Rhodamine B reveals remarkable efficiency, demonstrating its potential for long-term water remediation [26].

Pandey et al. (2024) prepared ZnO@CuO Nanocomposites (NCPs) by extracting the leaves of the *Achyranthes aspera* plant in different weight percentages of ZnO. Distilled water was used to make the leaf extract, which was then combined with copper and zinc nitrate. ZnO@CuO NCPs were produced and studied by UV–vis spectrophotometry, FTIR, FESEM, and XRD after calcination at 400°C. ZnO displayed nano capsule-like morphology, while CuO and ZnO@CuO NCPs had spherical morphology as seen by FESEM pictures. The development of a single-phase crystalline structure was validated by FTIR and XRD. The phases of CuO and ZnO were both existing in the nanocomposite. The range of band gap energies had been 1.54–3.05 eV. Higher values in dielectric constants were found in dielectric experiments for ZnO@CuO NCPs, particularly at 50 weight percent ZnO, indicating possible uses in high K value devices such as capacitors [27].

Idris et al. (2024) made use of peels of cabbage and used their extract to make iron-silver oxide bimetallic NPs sustainably. A thorough examination by EDX, FESEM, and various spectroscopy techniques verified nanoparticles' effective production. A silver-core iron-shell structure with a mean size of 22.3 nm was revealed by the results. Strong antioxidant characteristics and effective methyl red and phenol red dye degradation were demonstrated by the nanoparticles, and the obtained results from the study demonstrate these nanoparticles' potential for use in environmental remediation projects [28].

Reyes-Pérez et al. (2023) presented a new nanocomposite of FeO/ZnO nanoparticles complemented by spent coffee grounds in this work. Due to the abundance of antioxidants in them, trumpet and eucalyptus leaves function as bio-reducing agents for green synthesis. Through FTIR, SEM, EDS, XRD, and TEM characterization, stable NPs having a size range from about 5 to 30 nm were discovered. These nanoparticles act as catalysts in wastewater-based Fenton-like processes to break down dyes. Under specific conditions, the optimal removal efficiency which was

established using the Box Behnken experimental design produced a notable reduction in COD (56%) and a high discoloration ratio (88%) of indigo carmine in less than 120 minutes [29].

Faaizatunnisa et al. (2023) described a solvent-free pre-grinding process that yields a magnetic MOF composite, Fe3O4@SiO2@HKUST-1, using green synthesis. TEM and SEM studies revealed that the resultant core-shell structure was spherical and non-agglomerated. Fe3O4@SiO2 magnetic particles were added to HKUST-1, causing the composite to show larger pores and the development of mesopores. In comparison to pure HKUST-1 (188.7 mg/g), the composite exhibited a much higher capacity for adsorption (434.78 mg/g) when assessed as an adsorption medium for synthetic dyes. A pseudo 2nd order model along with Langmuir isotherm model was used for the description of the adsorption process. Additionally, the composite displayed improved stability, holding onto 71.95% of its adsorption capability even after five recycling cycles [30].

Ganesan et al. (2023) showed new hetero-structured V2O5/ZnO nanomaterials with effective photocatalytic activity at various ratios of composite ratios. 1:1 ratio of V2O5/ZnO nanocomposite, which was created using a high-energy ball miller technique and V2O5 and ZnO through physicochemical synthesis, showed the greatest potential (99.9% methylene blue colour eradication) for degrading organic contaminants by activating reactive hydroxyls in aqueous solutions. Furthermore, using the microdilution method, this ratio showed improved effectiveness against the pathogenic bacteria Staphylococcus aureus, with an MIC (minimum inhibitory concentration) of 400 µg/mL, indicating significant bacterial resistance. Overall, the work presents an easy-to-use, inexpensive, environmentally friendly approach for creating V2O5/ZnO nanohybrid composite materials that can be used for antibacterial and environmental remediation purposes [31].

Salem et al. (2023) worked on improving the photocatalytic characteristics of n-p heterojunction ZnO-based composites for methylene blue degradation in natural sun radiation presence. The composites of zinc oxide/metal oxide synthesized by the

hydrothermal method were subjected to extensive structural, morphological, and optical analysis using methods such as EDX, DRS, scanning electron microscopy (SEM), etc. The MO = Mn3O4; Fe3O4; CuO; NiO. The findings verified the existence of two pure phases in every sample, with MO evenly distributed across ZnO's surface. The better efficiency of the ZnO/ Fe3O4 nano-catalyst was evaluated using photocatalytic evaluation on the MB solution. This is ascribed to the development of ferrous oxide/zinc oxide p-n heterojunction, which caused reduction recombination of electron-hole pair and broadens the solar spectrum response, hence boosting photocatalytic activity [32].

Bhat and Chisti (2023) synthesized and presented a new ternary metal oxide composite with strong photocatalytic activity, ZnO/CuO/SnO2 to address the issue of contamination of aquatic environments because of the release of dyes from textile industries. The composition and optical properties of the composite were examined using structural and optical techniques. The bandgap in eV of ZnO was 3.18, for CuO it was 1.3, for SnO2 it was 3.5, and for the complex of three, it was 2.0. After four cycles, the composite showed remarkable photostability, maintaining a 93.68% efficiency of degradation of the fast-green dye in the presence of visible light [33].

Panchal et al. (2022) examined the antibacterial and photocatalytic properties of Ag/MgO nanocomposites (NCs) and MgO nanoparticles (NPs) produced from Aloe Vera extract in this study. Techniques for characterization verify their optical and structural characteristics. Ag/MgO-NCs work exceptionally well; in 120 minutes, they can break down 80.67% of phenol and 90.18% of dye when exposed to sunlight. With a 25-minute inactivation time and a 24 mm bacterial growth suppression zone, they also successfully fight E. coli. These results demonstrate the improved antibacterial and photocatalytic properties of Ag/MgO-NCs, indicating their potential as environmentally acceptable solutions for bacterial control and water purification [34].

Luo et al. (2022) investigated how well MCW composites, made by environmentally friendly ball milling, work to activate peroxymonosulfate (PMS) and break down doxycycline (DC) in water. The composites are reusable and show excellent catalytic

activity over a broad pH range (4–9). Singlet oxygen, oxygen vacancies, and superoxide free radicals for storing electrons inside the MCW structure all aid in the breakdown of DC. Furthermore, the study uses the ECOSAR tool to evaluate the toxicity of eighteen intermediates that are produced during the degradation of DC. All things considered, MCW composites show great promise for antibiotic decontamination [35].

Mahdi et al. (2022) explored the photocatalytic activity and activity against bacteria of nanocomposite DyBa2Fe3O7.988-DyFeO3 for sustainable uses by looking at their dual functionality. Energy efficiency was guaranteed by using ultrasonic synthesis, and the natural reagent properties of almond core extract contributed to the process's ecological credentials. With a 2.6 eV band gap, the nanocomposites showed promise as visible-active photocatalysts. They exhibited strong photocatalytic activity, degrading Rhodamin-B dye by 72% when exposed to visible light. Disc diffusion experiments verify their strong antibacterial effectiveness against Gram-negative bacteria, including *Escherichia coli* and *K. pneumonia*. The properties of the product are validated through characterization using spectroscopy and microscopy analysis [36].

Lin et al. (2022) improved the absorption of oxytetracycline hydrochloride (OTC), by using cyclodextrins (CDs) as modifiers for graphene-based nanoparticles of iron (GO@Fe NPs). This work tackled the environmental dangers associated with residual antibiotics. The removal efficiency surpasses bare GO and Fe NPs in a specific order. The influence of CDs on the structure and removal efficiency of GO@Fe NPs was clarified by characterization approaches. GO functioned as a transporter for Fe NPs within grafted cyclodextrin, improving elimination, according to Raman and X-ray diffraction investigations. The GO@Fe NPs modified with cyclodextrin had a large surface area (61.7 m2 · g−1) and small-sized particles (15 nm), with CDs serving as capping and stabilizing agents during green production. Testing on wastewater validates the potential of γCD-GO@Fe NPs in real-world applications [37].

Sackey et al. (2022) explored the interaction between nanocomposite of CuO-MgO

and methylene blue (MB) dye using Molecular Dynamics (MD) simulation and green nano chemistry, a first for the field. The nanocomposite, which was created using a natural extract from date pits in Africa, showed both monoclinic and cubic structures with distinct particle sizes. The cubic shape was verified by high-resolution TEM examination, and lattice fringes were shown to correlate with certain reflections. The MD analysis demonstrated the hydrophobic nature of MB dye and its significant affinity for surface interaction with the nanocomposite. The nanocomposite showed significant photocatalytic power against methylene blue in experimental validation, providing a feasible method for purifying dye-contaminated water [38].

Al-Zahrani et al. (2022) used a green technique to synthesize Ag/Fe2O3 nanocomposites from *Buddleja lindleyana* extract. Particle sizes between 25 and 174 nm were confirmed by characterization techniques, and their shape was proven to be triangular and spherical. The nanocomposite was stabilized by organic metabolites, according to FTIR analysis. Antibacterial testing revealed broad-spectrum action with inhibition zones ranging from 19.5 to 23.4 mm against different bacterial pathogens. Because of these biosynthesized nanocomposites' remarkable antibacterial capabilities against human pathogens, the study emphasizes their potential use in medicinal applications [39].

Basak et al. (2021) used extract from peels of *Punica granatum* as a bio-reducing agent to manufacture MnO-FeO nanocomposites. XRD, UV spectroscopy, FE-SEM, EDAX, FTIR, and DLS were among the characterization methods used, in comparison to iron oxide nanoparticles. These nanocomposites showed increased nanozyme activity and a greater affinity for binding to human serum albumin. In a dose-dependent manner, they demonstrated minimal cytotoxicity towards the human hepatic cell line (WRL-68) and substantial toxicity towards the human hepatocellular carcinoma (HUH-7) cells. The activities of the IONPs were influenced by the different percentages of MnO present in their lattice [40].

Ma et al. (2021) used pine needle extract to create composite particles of iron-copper oxides, which is an environmentally acceptable adsorbent to remove ofloxacin

(OFLX) along with norfloxacin (NOR) out of water. Particles of composite were studied by utilizing surface analytic techniques which include SEM, EDS, TEM, XPS, BET, and FTIR. Variables like pH, strength at the ionic level, temperature, etc. were some major factors that affected the adsorption of OFLX and NOR onto composites. While equilibrium data matched Redlich-Peterson, Koble-Corrigan, and Dubinin-Radushkevich models, kinetic data obeyed the Double-constant rate equation. The Langmuir model yielded different maximum adsorption capabilities in mmol/g for NOR and OFLX at a temperature 293 Kelvin. Thermodynamic studies showed that there occurred spontaneous and endothermic adsorption, most likely including hydrophobic, hydrogen bonding, electrostatic interactions, surface complexation, and π-π stacking [41].

Zelekew et al. (2021) used extract from water hyacinth extract to generate composite catalysts of chromium oxide and zinc oxide with different concentrations of precursors of chromium (0.02CrZn, 0.04CrZn and so on) while maintaining a constant Zn precursor (0.1 M). Tests and characterization for MB dye degradation showed that 0.08CrZn catalyst degraded 85% of the dye after 90 minutes of radiation. The percentages of degradation for the following catalysts were lower: ZnO (52%), Cr2O3 (74%), 0.1CrZ (80%), 0.06CrZ (74%), 0.04CrZ (79%), and 0.02CrZ (76%). The inclusion of chromium precursors at the ideal amount increased catalytic activity, possibly as a result of the plant extract's ability to promote porosity and better separating f electron and hole pair [42].

Ramzan et al. (2021) utilized rich phenolic content of *Cedrus deodara* extract, the formation of Cu@TiO2 nanoparticles can be achieved in a chemical-free, ecologically friendly, and time-efficient manner. TiO2 can be doped with copper to improve its energy band gap engineering capabilities and decrease photogenerated electron/hole pair recombination. Improved photocatalytic and antibacterial properties, as shown by characterization studies, hold promise for degrading methylene blue dye and stifling bacterial development. The recombination rate and energy band gap of titanium dioxide is lowered by the slow addition of copper dopant. This green synthesis

method, which makes use of plant extract, guarantees the manufacture of nanoparticles with dependability, sustainability, and speed [43].

Kumar et al. (2020) combined precursors of Zn (NO3)2.6H2O and Cu (NO3)2.3H2O with *Calotropis gigantea* leaf extract in this study to create a nanocomposite of ZnO–CuO using the method of solution combustion. Its content, shape, and crystalline nature were all validated by characterization using XRD, SEM-EDAX, HR-TEM, and FT-IR. The mean size of particles varied from about 10 to 40 nm. ZnO, CuO, −OH, −C–O, and C–H are examples of functional groups that were found, according to FT-IR analysis. Its capacity as a photocatalyst was indicated by an optical band gap estimate. The nanocomposite had strong antimicrobial activity against bacterial pathogens, and good photocatalytic activity, consuming methylene blue dye by 97.93% [44].

Lin et al. (2020) used the absorption capacity of GO, i.e. graphene oxide, and the optical characteristics of ZnO nanocrystals, and explained the precipitation technique of creating ZnO-GO nanocomposites. The homogenous loading of ZnO on the surface of GO with efficient interface coupling was confirmed by characterization techniques. The effectiveness of photocatalysis is increased by this connection, which makes the transfer of electrons from ZnO to GO easier. The composites showed a rate constant in 1st order reaction of exactly 0.04401 and a photodegradation efficiency of 97.6%. These results demonstrate the photocatalytic capability of ZnO-GO composites and point to possible uses in environmental cleanup. They also provide a basis for the development of sophisticated semiconductor composites based on graphene [45].

Liao et al. (2020) used a suspension of pure GO/MnSO4 and offered a simple and environmentally friendly way to create graphene oxide (GO) adorned with MnFe2O4 composites. The GO-MnFe2O4 composites' effective production was verified by characterization methods. Excellent adsorption characteristics for Pb2+ and Cu2+ ions in aqueous solutions were shown by these composites. The pseudo 2nd order model explained kinetics of adsorption, and the model named Langmuir isotherm provided a good description of the adsorption process. The adsorption process appears

to be spontaneous and endothermic, as revealed by thermodynamic studies. At 318 K, Pb2+ and Cu2+ were found to have maximal adsorption capabilities of 263.85 and 103.41 mg/g, respectively. The efficacy of GO-MnFe2O4 composites as effective adsorbents for the elimination of heavy metal ions.[46].

Ayodhya et al. (2020) presented a new method for synthesizing Ag@CeO2 composites stabilized with garlic extract, which effectively uses the surface plasmon resonance phenomenon to facilitate solar light conversion and absorption. With an average size of roughly 5–15 nm, characterization procedures verified the produced composites' high purity and well-crystalline nature. Fast electron transport and surface plasmon resonance are responsible for the composites' exceptional photocatalytic efficiency in the degradation of a single dye that is methylene blue and mixed that is methyl orange under solar as well as ultrasonic radiation. They also showed outstanding recyclability and stability. The composites' multifunctional qualities were further demonstrated by their improved antibacterial activity which acts against the bacterial and fungal strains when contrasted with pure CeO2 and Ag NPs [47].

Bhavyasree et al. (2020) used an extract of leaves of *Adhatoda vasica*, which serves as a capping, reducing agent, and a carbon source to create CuO/C nanocomposites. This new method combines room-temperature plant extract with pentahydrate of copper sulphate. Using XRD, UV-Vis, FTIR, FE-SEM, EDS, XPS, and TGA characterization, it was determined that 7–11 nm thick functionalized graphene-like carbon nanoflakes and copper oxide had formed. Significant antibacterial and antifungal activity was shown by the nanocomposites against *A. niger* and *Candida albicans* as well as *E. Coli*, *P. aeruginosa*, *K. pneumoniae*, and *S. aureus.* Additionally, the MIC and MFC/MBC values for Candida albicans and K. pneumonia were ascertained [48].

Ijaz et al. (2020) delved into the realm of nanotechnology, concentrating on nanoparticles having sizes ranging between 1 to 100 nm. Four main categories of nanoparticles, that is, inorganic, organic, ceramic, and carbon-based have been studied. The review has covered physical, chemical, and green synthesis processes

using quantitative (TEM, HAADF, ICP) and qualitative (UV-Vis, AFM, FT-IR, SEM, XRD) techniques, highlighting differences in the methods. It illustrates the range of uses for artificial nanoparticles [49].

Khan et al. (2020) have covered the usage of nanoparticles of silver (Ag) (NPs) in electronics, biomedicine along catalysis in this study, with a focus on the necessity of environmentally friendly and reasonably priced synthetic processes. Although it uses hazardous chemicals, chemical synthesis gives one control over characteristics like shape, crystallinity, and size of the particles. Also, even if bio-inspired techniques are less precise in regulating shape and crystallinity, they are more ecologically friendly. The review describes the function of Phyto molecules in nanoparticle creation and compares chemical synthesis with environmentally friendly techniques utilizing plant extracts. It has also provided an overview of the ways by which Phyto molecules surface-functionalized Ag NPs for use in biological applications [50].

Peralta-Videa et al. (2016) acknowledged the environmental risks associated with existing industrial synthesis methods while highlighting the growing production and utilization of metallic nanoparticles (MNPs) in a variety of goods. Using organic chemicals, microorganisms, plants, and materials derived from plants as reducing agents to avoid harsh conditions and toxic compounds, green synthesis has evolved as a more environmentally friendly option. Green synthesis offers several advantages as compared to conventional methods, and this has been highlighted in many academic papers; nonetheless, the practical scaling of green synthesized nanoparticles is still a challenge. The review has focussed on the challenges impeding the commercial feasibility of plant-based synthesis and covers both conventional and environmentally friendly synthesis methods as well as MNP applications [51].

Amooaghaie et al. (2015) conducted a study on the effects of green synthesis and chemical synthesis on human health and the environment. While in the chemical procedure, chemicals of sodium and silver were used, *Nigella sativa* leaf extract was applied as a reducing as well as capping agent in the green synthesis method. Brown AgNPs had been generated by both techniques, as shown by UV–visible spectra.

Nanosized crystallites were discovered by SEM, while functional groups required for synthesis were found by FTIR. According to toxicity testing, green AgNPs were less harmful than chemical AgNPs to mouse bone-forming stem cells and for the growth and germination of six plant species. Green-synthesized AgNPs are therefore safer and more environmentally benign [52].

Table 2.1. Summary of work done in green synthesis approach of metal oxides production and their uses.

S. No.	**Nanoparticle/Nanocomposites**	**Source**	**Morphology**	**Application**	**References**
1.	MgO	Hyphaene thebaica	Quasi-spherical	Photocatalytic efficiency: Potential in environmental remediation	[53]
2.	MgO	Metabolites of Lactobacillus gasseri	Spherical	High inhibitory effect against fungal strains	[54]
3.	CuO	Seed extract of Annona squamosa	Semi-globular	*B. alexandrina* snails' biological activity was damaged, thus can be made use of as a molluscicidal base	[55]
4.	CuO	Aqueous extract from Parthenium	Spherical	Degradation of Antibiotic Rifampicin, thus	[56]

		hysterophorus		can be used in environmental remediation	
5.	ZnO	Leaves extract from Hardwickia binata	Hexagonal	Anticancer activity against cancer cell lines (HepG2, (A431)	[57]
6.	ZnO	Myrtus communis extract	Spherical, Irregular	Methylene blue degradation	[58]
7.	Fe_3O_4	Plant extract of Aegle marmelos	Rhombohedral	Reduction in toxicity caused by Cr stress leading to chlorophyll content improvement and that of enzyme activities of antioxidants.	[59]
8.	Fe_3O_4	Extracts of Allium sativum seeds and cloves	Spherical	Antifungal activity against *Candida albicans*: Potential in landscape enhancement	[60]
9.	NiO	Hagenia abyssinica plant extract	Cubic	Adsorption of lead from aqueous solution	[61]
10.	NiO	Acacia nilotica leaf	Spherical	Inhibition effect against *B. subtilis*	[62]

		extracts			
11.	GS-Fe_3O_4/Cdots	Moringa oleifera extract, Extract of watermelon peel	Semi-spherical	Methylene Blue degradation	[63]
12.	Fe_3O_4-cellulose-Cu	Ceratonia siliqua aqueous extract	Spherical	Reduction of organic pollutants	[64]
13.	Ag/ZnO@Biochar	Persicaria salicifolia biomass	Spherical	Antimicrobial agent against *Klebsiella pneumonia* and good promising antioxidant material.	[65]
14.	ZnO@CdS	Leaf extract of Azadirachta indica	Irregular	Removal of pesticides	[66]
15.	CuO–ZnO	Aqueous extract of Verbascum sinaiticum Benth	Plate-like	Methylene blue degradation and 4-nitrophenol reduction: Potential for elimination of	[67]

				organic pollutants	
16.	$ZnO/BaMg_2$	Lemon peel extract	Hexagonal	Decomposition of dyes: rose bengal and methyl orange	[68]
17.	$MgFe_2O_4$@ $CoCr_2O_4$	Tragacanth Gum	Spinel cubic	Degradation of RB222 dye	[69]
18.	NiO/NiCo2 O4	Urtica extract	Cubic	Detection of Dopamine	[70]
19.	RGO/NiO	Psidium guajava (guava) leaves and Graphite Flakes	Irregular	Methylene Blue photodegradation	[71]
20.	Fe_3O_4@CN C/Cu)	Leaf extract of Petasites hybridus	Spherical	Venlafaxine Electrochemical detection	[72]

The review has extensively discussed the green synthesis method and characterization of various metal oxides as well as nanocomposites for numerous applications. There is a clear research gap in this field because there hasn't been much done on the formation of grow lights employing metal oxides and nanocomposites made using environmentally friendly processes. This lack of research offers a chance to investigate how these processes might be used to increase plant growth using artificial lighting. Thus, we developed our research goals with an emphasis on the environmentally friendly production of metal oxides and nanocomposites, and then use those materials to create efficient grow lights.

References:

1. M. Barzegar, D. Ahmadvand, Z. Sabouri, and M. Darroudi, “Phytoextract-mediated synthesis of magnesium oxide nanoparticles using Caccinia macranthera extract and examination of their photocatalytic and anticancer effects,” Materials Research Bulletin **169**, 112514 (2023).
2. L.T. Tai, N.M. Dat, N.T.H. Nam, H. An, L.M. Huong, C.Q. Cong, N.D. Hai, M.T. Phong, and N.H. Hieu, “Green synthesis of copper oxide nanoparticles for photodegradation of malachite green and antibacterial properties under visible light,” Optical Materials **136**, 113489 (2023).
3. Y.-T. Duan, K. Soni, D. Patel, H. Choksi, C.B. Sangani, W.S. Saeed, K.L. Ameta, and R.K. Ameta, “Green synthesis of iron oxide nanoparticles using Nicotiana plumbaginifolia and their biological evaluation,” Journal of Molecular Liquids **396**, 123985 (2024).
4. N.A. Idris, H.M. Yusoff, N.H. Idris, N. Badar, K. Elong, S.U. Muhamad, N.F.M. Yusoff, and C.P. Wai, “Green Synthesis of Zinc Oxide Nanoparticles Using Leaves Extract of Mariposa Christia vespertilionis and its Potential as Anode Materials in Sodium-Ion Batteries (SIBs),” Arabian Journal for Science and Engineering **49**(1), 623–635 (2023).
5. Md.A. Islam, V. Selvanathan, P. Chelvanathan, M.M. Haque, M. Mottakin, I.A. Alnaser, M.R. Karim, M.A. Ibrahim, T. Suemasu, and Md. Akhtaruzzaman, “Green synthesis of nickel oxide hole transport layer via aloe vera extract-assisted sol-gel process,” Journal of Sol-Gel Science and Technology **109**(2), 580–593 (2024).
6. P. Prabu, and V. Losetty, “Green synthesis of copper oxide nanoparticles using Macroptilium Lathyroides (L) leaf extract and their spectroscopic characterization, biological activity and photocatalytic dye degradation study,” Journal of Molecular Structure **1301**, 137404 (2023).
7. S. Ali, K.G. Sudha, N. Thirumalaivasan, M. Ahamed, S. Pandiaraj, V.D. Rajeswari, Y. Vinayagam, M. Thiruvengadam, and R. Govindasamy, “Green

Synthesis of Magnesium Oxide Nanoparticles by Using Abrus precatorius Bark Extract and Their Photocatalytic, Antioxidant, Antibacterial, and Cytotoxicity Activities," Bioengineering **10**(3), 302 (2023).

8. I. Ashraf, N.B. Singh, and A. Agarwal, "Green synthesis of iron oxide nanoparticles using Amla seed for methylene blue dye removal from water," Materials Today Proceedings **72**, 311–316 (2022).
9. M. MuthuKathija, M.S.M. Badhusha, and V. Rama, "Green synthesis of zinc oxide nanoparticles using Pisonia Alba leaf extract and its antibacterial activity," Applied Surface Science Advances **15**, 100400 (2023).
10. Z. Alhalili, "Green synthesis of copper oxide nanoparticles CuO NPs from Eucalyptus Globoulus leaf extract: Adsorption and design of experiments," Arabian Journal of Chemistry **15**(5), 103739 (2022).
11. N. Al-Zaqri, K. Umamakeshvari, V. Mohana, A. Muthuvel, and A. Boshaala, "Green synthesis of nickel oxide nanoparticles and its photocatalytic degradation and antibacterial activity," Journal of Materials Science Materials in Electronics **33**(15), 11864–11880 (2022).
12. S.A. Kumar, M. Jarvin, S.S.R. Inbanathan, A. Umar, N.P. Lalla, N.Y. Dzade, H. Algadi, Q.I. Rahman, and S. Baskoutas, "Facile green synthesis of magnesium oxide nanoparticles using tea (Camellia sinensis) extract for efficient photocatalytic degradation of methylene blue dye," Environmental Technology & Innovation **28**, 102746 (2022).
13. M. Rafique, R. Tahir, S.S.A. Gillani, M.B. Tahir, M. Shakil, T. Iqbal, and M.O. Abdellahi, "Plant-mediated green synthesis of zinc oxide nanoparticles fromSyzygium Cuminifor seed germination and wastewater purification," International Journal of Environmental & Analytical Chemistry **102**(1), 23–38 (2020).
14. S. Ananthi, M. Kavitha, E.R. Kumar, A. Balamurugan, Y. Al-Douri, H.K. Alzahrani, A.A. Keshk, T.M. Habeebullah, S.H. Abdel-Hafez, and N.M. El-Metwaly, "Natural tannic acid (green tea) mediated synthesis of ethanol sensor

based Fe3O4 nanoparticles: Investigation of structural, morphological, optical properties and colloidal stability for gas sensor application," Sensors and Actuators B Chemical **352**, 131071 (2021).

15. E.F. El-Belely, M.M.S. Farag, H.A. Said, A.S. Amin, E. Azab, A.A. Gobouri, and A. Fouda, "Green Synthesis of Zinc Oxide Nanoparticles (ZnO-NPs) Using Arthrospira platensis (Class: Cyanophyceae) and Evaluation of their Biomedical Activities," Nanomaterials **11**(1), 95 (2021).
16. A.U. Khan, A.U. Khan, B. Li, M.H. Mahnashi, B.A. Alyami, Y.S. Alqahtani, A.O. Alqarni, Z.U.H. Khan, S. Ullah, M. Wasim, Q.U. Khan, and W. Ahmad, "Biosynthesis of silver capped magnesium oxide nanocomposite using Olea cuspidata leaf extract and their photocatalytic, antioxidant and antibacterial activity," Photodiagnosis and Photodynamic Therapy **33**, 102153 (2020).
17. Z. Sabouri, A. Rangrazi, M.S. Amiri, M. Khatami, and M. Darroudi, "Green synthesis of nickel oxide nanoparticles using Salvia hispanica L. (chia) seeds extract and studies of their photocatalytic activity and cytotoxicity effects," Bioprocess and Biosystems Engineering **44**(11), 2407–2415 (2021).
18. V.U. Siddiqui, A. Ansari, R. Chauhan, and W.A. Siddiqi, "Green synthesis of copper oxide (CuO) nanoparticles by Punica granatum peel extract," Materials Today Proceedings **36**, 751–755 (2020).
19. A. Haider, M. Ijaz, S. Ali, J. Haider, M. Imran, H. Majeed, I. Shahzadi, M.M. Ali, J.A. Khan, and M. Ikram, "Green Synthesized Phytochemically (Zingiber officinale and Allium sativum) Reduced Nickel Oxide Nanoparticles Confirmed Bactericidal and Catalytic Potential," Nanoscale Research Letters **15**(1), (2020).
20. U.L. Ifeanyichukwu, O.E. Fayemi, and C.N. Ateba, "Green Synthesis of Zinc Oxide Nanoparticles from Pomegranate (Punica granatum) Extracts and Characterization of Their Antibacterial Activity," Molecules **25**(19), 4521 (2020).
21. M. Jamzad, and M.K. Bidkorpeh, "Green synthesis of iron oxide nanoparticles by the aqueous extract of Laurus nobilis L. leaves and evaluation of the antimicrobial activity," Journal of Nanostructure in Chemistry **10**(3), 193–201 (2020).

22. E.A. Mohamed, “Green synthesis of copper & copper oxide nanoparticles using the extract of seedless dates,” Heliyon **6**(1), e03123 (2020).
23. S.D. Roy, K.C. Das, and S.S. Dhar, “Facile synthesis of CuO-Ag2O hybrid metal oxide composite using carica papaya, cocooning with hydroxyapatite, and photocatalytic degradation of organic dyes,” Materials Science and Engineering B **303**, 117331 (2024).
24. T.J. Masho, P.T. Arasu, R.F. Bogale, E. AmareZerrefa, and S. Ramamurthy, “Green synthesis, characterization of Ag2O/CuO/ZnO nano composites using aqueous extract of Croton macrostachyus leaf for Photo degradation, anti-microbial and antioxidant activities,” Results in Chemistry, 101369 (2024).
25. M. Varshini, K. Ravichandran, P.K. Praseetha, M. Ayyanar, S.J. Ramalingam, A. Viji, and R. Manimekalai, “Effective composite partnering of green synthesized rGO with SnO2:Ce: An eco-friendly approach using Cassia fistula fruit pulp for photocatalytic and biomedical applications,” Ceramics International **50**(9), 14253–14267 (2024).
26. P. Pandey, and A.K. Choubey, “Green synthesized ZnO@CuO nanocomposites using Achyranthes aspera leaves extract for dielectric applications,” Journal of Alloys and Compounds **970**, 172492 (2023).
27. D.M. Nzilu, E.S. Madivoli, D.S. Makhanu, S.I. Wanakai, G.K. Kiprono, and P.G. Kareru, “Green synthesis of copper oxide nanoparticles and its efficiency in degradation of rifampicin antibiotic,” Scientific Reports **13**(1), (2023).
28. D.S. Idris, and A. Roy, “Antioxidant and dye degradation activity of green synthesized silver-iron oxide (Ag-Fe2O3) bimetallic nanoparticles,” Nano-Structures & Nano-Objects **38**, 101142 (2024).
29. J.A. Reyes-Pérez, G. Roa-Morales, C.A. De León-Condes, and P. Balderas-Hernández, “Nanocomposites from spent coffee grounds and iron/zinc oxide: green synthesis, characterization, and application in textile wastewater treatment,” Water Science & Technology **88**(6), 1547–1563 (2023).
30. N. Faaizatunnisa, R. Ediati, H. Fansuri, H. Juwono, S. Suprapto, A.R.P. Hidayat,

and L.L. Zulfa, “Facile green synthesis of core–shell magnetic MOF composites (Fe3O4@SiO2@HKUST-1) for enhanced adsorption capacity of methylene blue,” Nano-Structures & Nano-Objects **34**, 100968 (2023).

31. S. Ganesan, R. Gurunathan, R.R. Pasupuleti, H.-U. Dahms, L.A. Pragasan, K. SenthilKannan, and V.K. Ponnusamy, “Green synthesis of V2O5/ZnO nanocomposite materials for efficient photocatalytic and anti-bacterial applications,” Applied Nanoscience **13**(1), 859–869 (2021).
32. B.B. Salem, G. Essalah, S.B. Ameur, B. Duponchel, H. Guermazi, S. Guermazi, and G. Leroy, “Synthesis and comparative study of the structural and optical properties of binary ZnO-based composites for environmental applications,” RSC Advances **13**(9), 6287–6303 (2023).
33. A.H. Bhat, and H.-T.-N. Chisti, “Facile fabrication of ternary metal oxide ZnO/CuO/SnO 2 nanocomposite for excellent photocatalytic degradation of fast green dye,” International Journal of Environmental & Analytical Chemistry **103**(20), 9594–9615 (2021).
34. P. Panchal, D.R. Paul, S. Gautam, P. Meena, S.P. Nehra, S. Maken, and A. Sharma, “Photocatalytic and antibacterial activities of green synthesized Ag doped MgO nanocomposites towards environmental sustainability,” Chemosphere **297**, 134182 (2022).
35. X. Luo, Y. You, M. Zhong, L. Zhao, Y. Liu, R. Qiu, and Z. Huang, “Green synthesis of manganese–cobalt–tungsten composite oxides for degradation of doxycycline via efficient activation of peroxymonosulfate,” Journal of Hazardous Materials **426**, 127803 (2021).
36. M.A. Mahdi, S.R. Yousefi, L.S. Jasim, and M. Salavati-Niasari, “Green synthesis of DyBa2Fe3O7.988/DyFeO3 nanocomposites using almond extract with dual eco-friendly applications: Photocatalytic and antibacterial activities,” International Journal of Hydrogen Energy **47**(31), 14319–14330 (2022).
37. X. Lin, Q. Xu, L. Gan, G. Owens, and Z. Chen, “Cyclodextrin modified green synthesized graphene oxide@iron nanoparticle composites for enhanced removal

of oxytetracycline," Journal of Colloid and Interface Science **608**, 3159–3167 (2021).

38. J. Sackey, M. Akbari, N. Tandjigora, K.J. Cloete, A.K.H. Bashir, R. Morad, and M. Maaza, "Industrial textile removal using date pit assisted CuO-MgO nanocomposite: Molecular dynamics and biosynthesis analysis," Journal of King Saud University - Science **34**(3), 101840 (2022).
39. F. a. M. Al-Zahrani, S.S. Salem, H.A. Al-Ghamdi, L.M. Nhari, L. Lin, and R.M. El-Shishtawy, "Green Synthesis and Antibacterial Activity of Ag/Fe2O3 Nanocomposite Using Buddleja lindleyana Extract," Bioengineering **9**(9), 452 (2022).
40. S. Basak, S. Ali, M. Mondal, D. Roy, A. Dutta, A. Kumar, S. Sikdar, and M.N. Roy, "Green synthesis and characterization of heterostructure MnO-FeO nanocomposites to study the effect on oxidase enzyme mimicking, HSA binding interaction and cytotoxicity," Chemical Physics Letters **785**, 139163 (2021).
41. P. Ma, Q. Liu, P. Liu, H. Li, X. Han, L. Liu, and W. Zou, "Green synthesis of Fe/Cu oxides composite particles stabilized by pine needle extract and investigation of their adsorption activity for norfloxacin and ofloxacin," Journal of Dispersion Science and Technology **42**(9), 1350–1367 (2020).
42. O.A. Zelekew, P.A. Fufa, F.K. Sabir, and A.D. Duma, "Water hyacinth plant extract mediated green synthesis of Cr2O3/ZnO composite photocatalyst for the degradation of organic dye," Heliyon **7**(7), e07652 (2021).
43. M. Ramzan, R.M. Obodo, M.I. Shahzad, S. Mukhtar, S.Z. Ilyas, and T. Mahmood, "Green synthesis of Cu@TiO2 via cedrus deodara leaf extract: A novel composite with high photocatalytic and antibacterial activity," Current Research in Green and Sustainable Chemistry **4**, 100137 (2021).
44. C.R.R. Kumar, V.S. Betageri, G. Nagaraju, G.H. Pujar, O.H. S, and L.M. S, "One-pot green synthesis of ZnO–CuO nanocomposite and their enhanced photocatalytic and antibacterial activity," Advances in Natural Sciences Nanoscience and Nanotechnology **11**(1), 015009 (2020).

45. Y. Lin, R. Hong, H. Chen, D. Zhang, and J. Xu, “Green synthesis of ZNO-GO composites for the photocatalytic degradation of methylene blue,” Journal of Nanomaterials **2020**, 1–11 (2020).
46. F. Liao, G. Diao, and H. Li, “Green synthesis of graphene oxide-MnFe 2 O 4 composites and their application in removing heavy metal ions,” Micro & Nano Letters **15**(1), 7–12 (2019).
47. D. Ayodhya, and G. Veerabhadram, “Green synthesis of garlic extract stabilized Ag@CeO2 composites for photocatalytic and sonocatalytic degradation of mixed dyes and antimicrobial studies,” Journal of Molecular Structure **1205**, 127611 (2019).
48. P.G. Bhavyasree, and T.S. Xavier, “Green synthesis of Copper Oxide/Carbon nanocomposites using the leaf extract of Adhatoda vasica Nees, their characterization and antimicrobial activity,” Heliyon **6**(2), e03323 (2020).
49. I. Ijaz, E. Gilani, A. Nazir, and A. Bukhari, “Detail review on chemical, physical and green synthesis, classification, characterizations and applications of nanoparticles,” Green Chemistry Letters and Reviews **13**(3), 223–245 (2020).
50. M. Khan, M.R. Shaik, S.F. Adil, S.T. Khan, A. Al-Warthan, M.R.H. Siddiqui, M.N. Tahir, and W. Tremel, “Plant extracts as green reductants for the synthesis of silver nanoparticles: lessons from chemical synthesis,” Dalton Transactions **47**(35), 11988–12010 (2018).
51. J.R. Peralta-Videa, Y. Huang, J.G. Parsons, L. Zhao, L. Lopez-Moreno, J.A. Hernandez-Viezcas, and J.L. Gardea-Torresdey, “Plant-based green synthesis of metallic nanoparticles: scientific curiosity or a realistic alternative to chemical synthesis?,” Nanotechnology for Environmental Engineering **1**(1), (2016).
52. R. Amooaghaie, M.R. Saeri, and M. Azizi, “Synthesis, characterization and biocompatibility of silver nanoparticles synthesized from Nigella sativa leaf extract in comparison with chemical silver nanoparticles,” Ecotoxicology and Environmental Safety **120**, 400–408 (2015).
53. A. Muhaymin, H.E.A. Mohamed, K. Hkiri, A. Safdar, S. Azizi, and M. Maaza,

"Green synthesis of magnesium oxide nanoparticles using Hyphaene thebaica extract and their photocatalytic activities," Scientific Reports **14**(1), (2024).

54. G. Abdel-Maksoud, M. Abdel-Nasser, S.E.-D. Hassan, A. Eid, A. Abdel-Nasser, and A. Fouda, "Green synthesis of magnesium oxide nanoparticles using probiotic strain Lactobacillus gasseri and their activity against fungal strains isolated from historical manuscripts," Egyptian Journal of Chemistry **66**(10) (2023).
55. A. a. A. Hussein, M.B.A. El-Latif, M.I.S. El-Din, N.S. El-Shenawy, O. Hammam, and A.M. Ibrahim, "The Molluscicidal Activity of Green Synthesized Copper Oxide–Based Annona squamosa Seed Extract Nanoparticles on the Feeding Behavior, Biochemical, Molecular, and Immunohistochemical Alterations of Biomphalaria alexandrina Snails," Biological Trace Element Research **202**(5), 2327–2337 (2023).
56. D.M. Nzilu, E.S. Madivoli, D.S. Makhanu, S.I. Wanakai, G.K. Kiprono, and P.G. Kareru, "Green synthesis of copper oxide nanoparticles and its efficiency in degradation of rifampicin antibiotic," Scientific Reports **13**(1), (2023).
57. P. Manimegalai, K. Selvam, S. Loganathan, D. Kirubakaran, M.S. Shivakumar, M. Govindasamy, U. Rajaji, and A.A.A. Bahajjaj, "Green synthesis of zinc oxide (ZnO) nanoparticles using aqueous leaf extract of Hardwickia binata: their characterizations and biological applications," Biomass Conversion and Biorefinery, (2023).
58. N. Sedefoglu, "Characterization and photocatalytic activity of ZnO nanoparticles by green synthesis method," Optik **288**, 171217 (2023).
59. S. Zafar, A. Farooq, S. Batool, T. Tariq, M. Hasan, and G. Mustafa, "Green synthesis of iron oxide nanoparticles for mitigation of chromium stress and anti-oxidative potential in Triticum aestivum," Hybrid Advances, 100156 (2024).
60. L. Liu, Y. Li, A.A. Al-Huqail, E. Ali, T. Alkhalifah, F. Alturise, and H.E. Ali, "Green synthesis of Fe3O4 nanoparticles using Alliaceae waste (Allium sativum) for a sustainable landscape enhancement using support vector regression," Chemosphere **334**, 138638 (2023).

61. A.E. Ferenji, Y.E. Hassen, S.L. Mekuria, and W.M. Girma, “Biogenic mediated green synthesis of NiO nanoparticles for adsorptive removal of lead from aqueous solution,” Heliyon **10**(11), e31669 (2024).
62. S. Hussain, M.A. Muazzam, M. Ahmed, M. Ahmad, Z. Mustafa, S. Murtaza, J. Ali, M. Ibrar, M. Shahid, and M. Imran, “Green synthesis of nickel oxide nanoparticles using Acacia nilotica leaf extracts and investigation of their electrochemical and biological properties,” Journal of Taibah University for Science **17**(1), (2023).
63. E.K. Sari, R.M. Tumbelaka, H. Ardiyanti, N.I. Istiqomah, N. Chotimah, and E. Suharyadi, “Green synthesis of magnetically separable and reusable Fe3O4/Cdots nanocomposites photocatalyst utilizing Moringa oleifera extract and watermelon peel for rapid dye degradation,” Carbon Resources Conversion **6**(4), 274–286 (2023).
64. E. Kalantari, M.A. Khalilzadeh, D. Zareyee, and M. Shokouhimehr, “Catalytic degradation of organic dyes using green synthesized Fe3O4-cellulose-copper nanocomposites,” Journal of Molecular Structure **1218**, 128488 (2020).
65. M. Hosny, M. Fawzy, and A.S. Eltaweil, “Green synthesis of bimetallic Ag/ZnO@Biohar nanocomposite for photocatalytic degradation of tetracycline, antibacterial and antioxidant activities,” Scientific Reports **12**(1), (2022).
66. M. Rani, J. Yadav, N. Keshu, and U. Shanker, “Green synthesis of sunlight responsive zinc oxide coupled cadmium sulfide nanostructures for efficient photodegradation of pesticides,” Journal of Colloid and Interface Science **601**, 689–703 (2021).
67. A.G. Bekru, L.T. Tufa, O.A. Zelekew, M. Goddati, J. Lee, and F.K. Sabir, “Green synthesis of a CUO–ZNO nanocomposite for efficient photodegradation of methylene blue and reduction of 4-Nitrophenol,” ACS Omega **7**(35), 30908–30919 (2022).
68. I. Kir, S.E. Laouini, S. Meneceur, A. Bouafia, and H.A.M. Mohammed, “Biosynthesis and characterization of novel nanocomposite ZnO/BaMg2

efficiency for high-speed adsorption of AZO dye," Biomass Conversion and Biorefinery, (2023).

69. S.T. Fardood, F. Moradnia, R. Forootan, R. Abbassi, S. Jalalifar, A. Ramazani, and M. Sillanpää, "Facile green synthesis, characterization and visible light photocatalytic activity of MgFe2O4@CoCr2O4 magnetic nanocomposite," Journal of Photochemistry and Photobiology a Chemistry **423**, 113621 (2021).
70. M. Amiri, H.A. Javar, and H. Mahmoudi-Moghaddam, "Facile green synthesis of NIO/NICO2O4 nanocomposite as an efficient electrochemical platform for determination of dopamine," Electroanalysis **33**(5), 1205–1214 (2021).
71. S. Sadhukhan, A. Bhattacharyya, D. Rana, T.K. Ghosh, J.T. Orasugh, S. Khatua, K. Acharya, and D. Chattopadhyay, "Synthesis of RGO/NiO nanocomposites adopting a green approach and its photocatalytic and antibacterial properties," Materials Chemistry and Physics **247**, 122906 (2020).
72. M.A. Khalilzadeh, S. Tajik, H. Beitollahi, and R.A. Venditti, "Green Synthesis of Magnetic Nanocomposite with Iron Oxide Deposited on Cellulose Nanocrystals with Copper (Fe3O4@CNC/Cu): Investigation of Catalytic Activity for the Development of a Venlafaxine Electrochemical Sensor," Industrial & Engineering Chemistry Research **59**(10), 4219–4228 (2020).

Chapter 3

SYNTHESIS AND CHARACTERIZATION

3.1. Introduction

In the presented research, the synthesis of metal oxides, their nanocomposites, and rare earth-dopant terbium was conducted using a green synthesis approach utilizing waste peels from fruits and vegetables. Green synthesis approaches are being researched for a range of applications due to the growing need for environmentally friendly and sustainable materials. Utilizing these materials to produce grow lights, which are essential for promoting plant development in controlled conditions, is one interesting area of study. The green synthesis method of metal oxides minimizes the use of hazardous chemicals and has a lower environmental impact than conventional processes, offering a sustainable substitute. Our research has focused on the environmentally friendly synthesis of metal oxides from organic waste materials, like potato and banana peels. In the present study of potato *Solanum tuberosum*, banana (*Musa*.), and peas (*Pisum sativum*) peels, along with various kitchen waste materials, which can be effectively utilized. These peels are available in excess throughout the year due to the consistent demand. By utilizing these peels effectively, we can reduce waste and promote environmental sustainability. The reducing potential of plant extract has been known for many years, but it has only been exploited in the last two decades to reduce metal salts. Plant leaves, flowers, fruits, and seeds include phytochemicals like phenols, flavonoids, ascorbic acid, terpenes, citric acid and alkaloids which are reducing agents. Green synthesis of NPs using plants is an important and useful field of nanotechnology since phytochemicals found in plants work as both reducing and capping agents. [1-2]

This research aims to explore sustainable methods for repurposing these organic waste products, highlighting their potential applications. Because of the reducing and stabilizing effects of these natural sources, metal oxides with useful properties for grow light production are formed. The procedure is environmentally benign and energy-efficient, supporting the objectives of sustainable development. However, very

little research has been done on growing light generation from metal oxides and their nanocomposites, particularly when green synthesis techniques are employed. This research aims to fill this gap by investigating sustainable methods for creating effective materials specifically suited for plant growth applications. The synthesis of metallic oxides and their nanocomposites, which can be utilized in grow light production that maximizes light absorption for plant growth, is the area that has been focussed in the research. Using methods namely UV spectroscopy, X-ray diffraction, Fluorescence spectroscopy, FE-SEM, and Fourier-transform infrared spectroscopy, this study investigates structural, optical and morphological aspects of produced materials. Characterization was performed at the Department of MNIT Jaipur, as well as the central instrumental facility Lovely Professional University (Phagwara).

3.2 Mechanism behind metal oxide synthesis from plant waste

For green synthesis of metal nanoparticles, precursor metal ions are mixed along with plant extract. Table 3.1 lists the various metal salts which are utilized for synthesis of the metal nanoparticles. The plant extracts consist of phytochemicals that can act as reducing as well as stabilizing agents for nanoparticle synthesis. There are many such bioactive substances like flavonoids, alkaloids, polyphenols, etc. present in plants. Fig. 3.1 represents the reaction between precursor metal ions and flavonoids present in the banana peel extract. Banana peels contain flavonoids like quercetin and kaempferol, known for their antioxidant and anti-inflammatory properties. Potato peels are rich in chlorogenic acid and rutin, which also exhibit significant antioxidant effects [3,4]. Peas peels contain catechin and epicatechin, further enhancing their role in promoting cardiovascular health. Similarly, peels of potato and peas consist of other bioactive substances which cause bio-reduction of metal ion precursors.

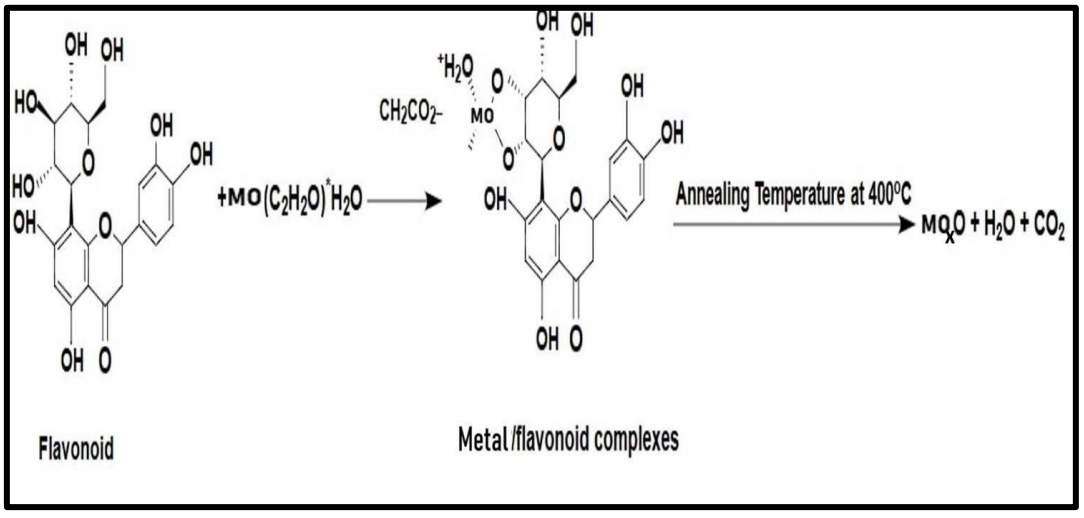

Fig 3.1 Describing the mechanism of green synthesis of MOs from green waste.

3.3. Material and chemical details

Table 3.1 Details of the chemicals used for the preparation of metal oxide.

S. No.	Chemical Name	Chemical Formula	Molecular Weight (g/mol)	Chemical Purity	Manufacturer
1.	Nickel Acetate Tetrahydrate	$(CH_3.COO)2Ni.4H_2O$	248.84	98%	LOBA Chemicals
2.	Cupric Nitrate Tetrahydrate	$Cu\ (NO_3)_2.3H_2O$	241.60	99.5%	LOBA Chemicals
3.	Magnesium Acetate Tetrahydrate	$(CH_3.COO)2Mg.4H_2O$	214.45	98%	LOBA Chemicals
4.	Zinc Nitrate Hexahydrate	$Zn\ (NO_3)_2.6H_2O$	297.48	96%	LOBA Chemicals
5.	Ferric Nitrate Nonahydrate	$Fe\ (NO_3)_3.9H_2O$	404.00	98%	LOBA Chemicals
6.	Terbium Nitrate	$Tb\ (NO_3)_3.xH_2O$	453.00	99%	Alfa Aesar

	Hydrate				
7.	Cobalt Nitrate	$Co(NO_3)_3.9H_2O$	400.15	98%	LOBA Chemicals

Table 3.2. Comprehensive overview of various waste peels used for the synthesis of metal oxides.

S.no	Waste Peels	Collected From	Mass of peels used
1.	Banana	Juice Bar of LPU	30 g per sample
2.	Potato	Kitchen Waste	30 g per sample
3.	Peas	Kitchen waste	30 g per sample

3.4. Synthesis of Metal Oxide

3.4.1. Synthesis of metal oxide from Banana peels

In this synthesis we used banana potatoes, peas peels were collected from the juice bar and kitchen waste then cleaned with deionized water to get rid of impurities and dust. The peels were dried completely, and then 30 g of peels were cooked for 30 min on a magnetic stirrer in 100 ml of purified water. They were then cooled at room temperature. Then, peels were filtered using filter paper named Whatman No. 1. This extract obtained was then kept in the refrigerator at 4°C for subsequent usage. Table 3.3 provides information on metal oxides (MOs), yield obtained from peels, metal precursor salt content, and the amount of waste peels used. The same procedure was followed to prepare extract from peels of potatoes and peas.

Using banana peels, we created nanoparticles of copper oxide, nickel oxide, zinc oxide, iron oxide, and magnesium oxide. Fig. 3.2 and 3.3 depicts schematic steps required for the synthesis of metal oxides. 30 g of peels were taken out of the stock to be used in the metal oxide synthesis. This solution then was stirred in exactly 30 ml of distilled water for 3 hours at 70°C. Then, copper nitrate trihydrate measuring 1g was added which resulted in peels almost instantaneously turning to brownish green. The sample material was boiled to create a brown paste. After drying, the paste was put in the muffle furnace and heated to 400°C for four hours. The method was repeated utilizing precursors such as cupric nitrate trihydrate, nickel acetate, zinc nitrate hexahydrate, magnesium nitrate hexahydrate, and iron nitrate hexahydrate to prepare other metal oxides like NiO, ZnO, Fe_3O_4, and MgO. To create metal oxides, similar reactions between the salts of metals including zinc, nickel, iron, and magnesium were performed with the extract of banana peel.

This procedure was also followed for synthesizing all the above-mentioned metal oxides from the extract of peels of potatoes and peas.

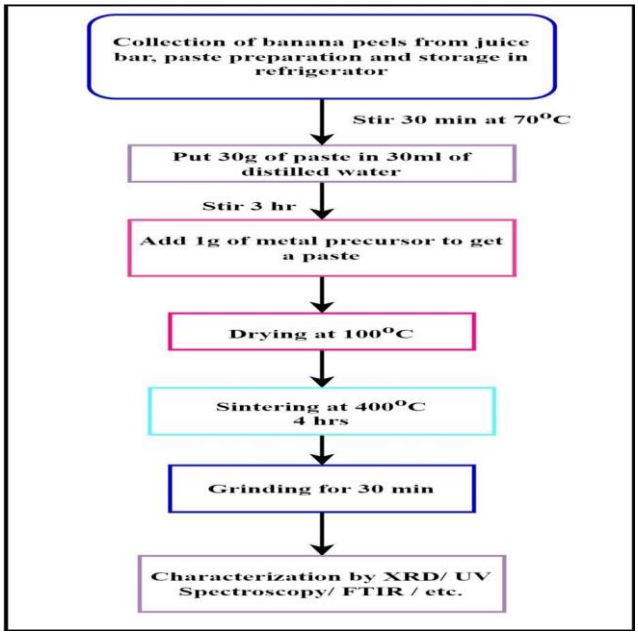

Fig 3.2. Steps involved in metal oxides synthesis made from waste banana peels.

Table 3.3. Components and their quantities used for preparation of metal oxides (MO).

Name of Metal Oxide	Name of Metal Precursor Salt	Metal Precursor mass(g)	Paste of Potato/Banana /pea Peel (g)	Yield from Potato peel (g)	Yield from Banana peel (g)	Yield from Peas peel (g)
CuO	Cupric Nitrate Trihydrate	1.00	30	0.65	0.8	0.5
NiO	Nickel Acetate	1.00	30	0.72	0.7	0.6
ZnO	Zinc Hexahydrate	1.00	30	0.62	0.5	0.4
MgO	Magnesium Nitrate	1.00	30	0.75	0.6	0.5
Fe_3O_4	Ferric Nitrate	1.00	30	0.64	0.7	0.6

d

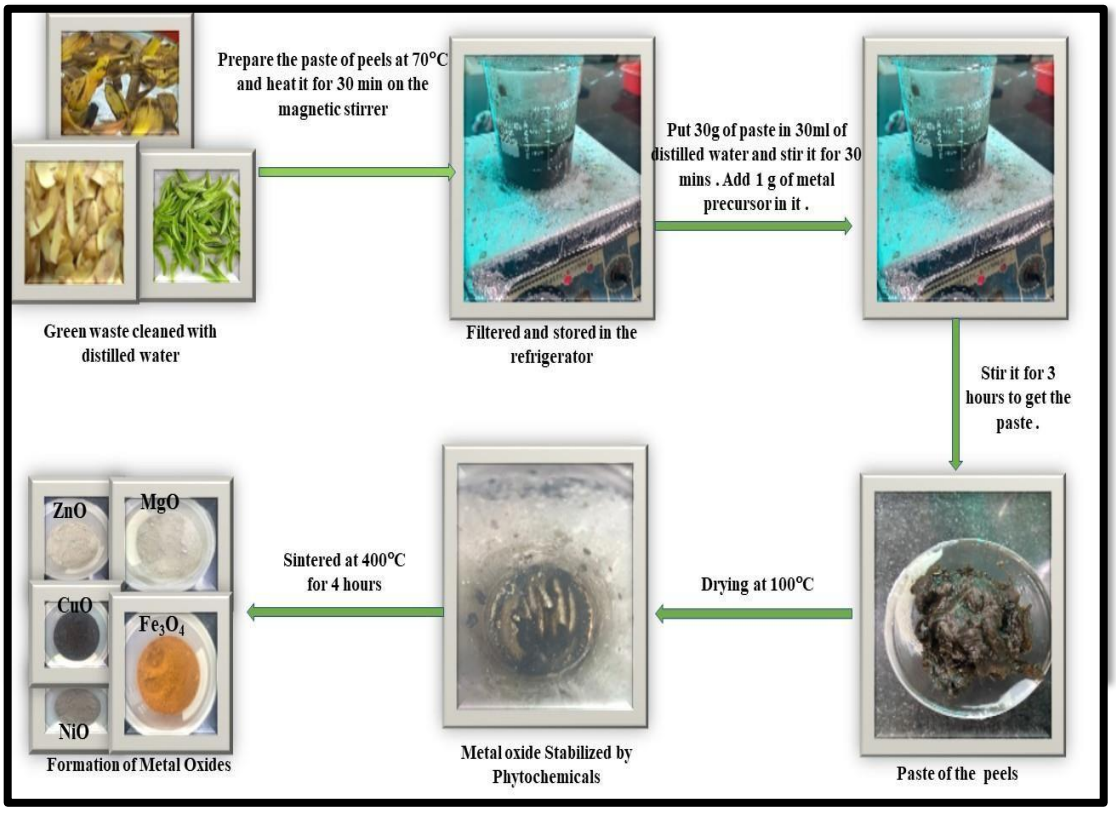

Fig 3.3. Pictorial representation of the synthesis from waste peels of banana, peas, potato using the green synthesis method

3.4.2. Synthesis of nanocomposite from metal oxides (MOs)

To make nanocomposite, several weight ratios of CuO to ZnO as mentioned in Table 3.4 were obtained by mixing copper and zinc acetate, which were dissolved in distilled water measuring 30 ml, with banana peels weighing 30 gm. Table 3.4 shows the proportion of Copper and Zinc used in nanocomposite preparation.

After that, the nanocomposite samples were dried at a temperature of 100°C, then sintering was done for 4 h at a temperature of 400°C, and then ground for about 30 min with a mortar and pestle. Then, XRD, FESEM, EDX, UV-Vis, FTIR and fluorescence spectroscopy were used for the characterization process. Fig. 3.4 depicts the flowchart representing steps involved in the synthesis of metal nanocomposites.

As discussed in Fig. 1.11, all other nanocomposites studied in this work were synthesized using the same steps involved in the synthesis of CuO/ZnO. This consistent methodology ensures uniformity in the synthesis process across different nanocomposites.

Table 3.4 Proportion of Copper and Zinc used in nanocomposite preparation**.**

S. No.	**Cupric Nitrate Trihydrate(g)**	**Zinc Hexahydrate (g)**	**Mass of peels (g)**	**Sintering Temp.(°C)**	**Yield (g) of CuO/ZnO nanocomposite**
1.	0.2	0.8	30	400	0.8
2.	0.4	0.6	30	400	0.7
3.	0.6	0.4	30	400	0.6
4.	0.8	0.2	30	400	0.6

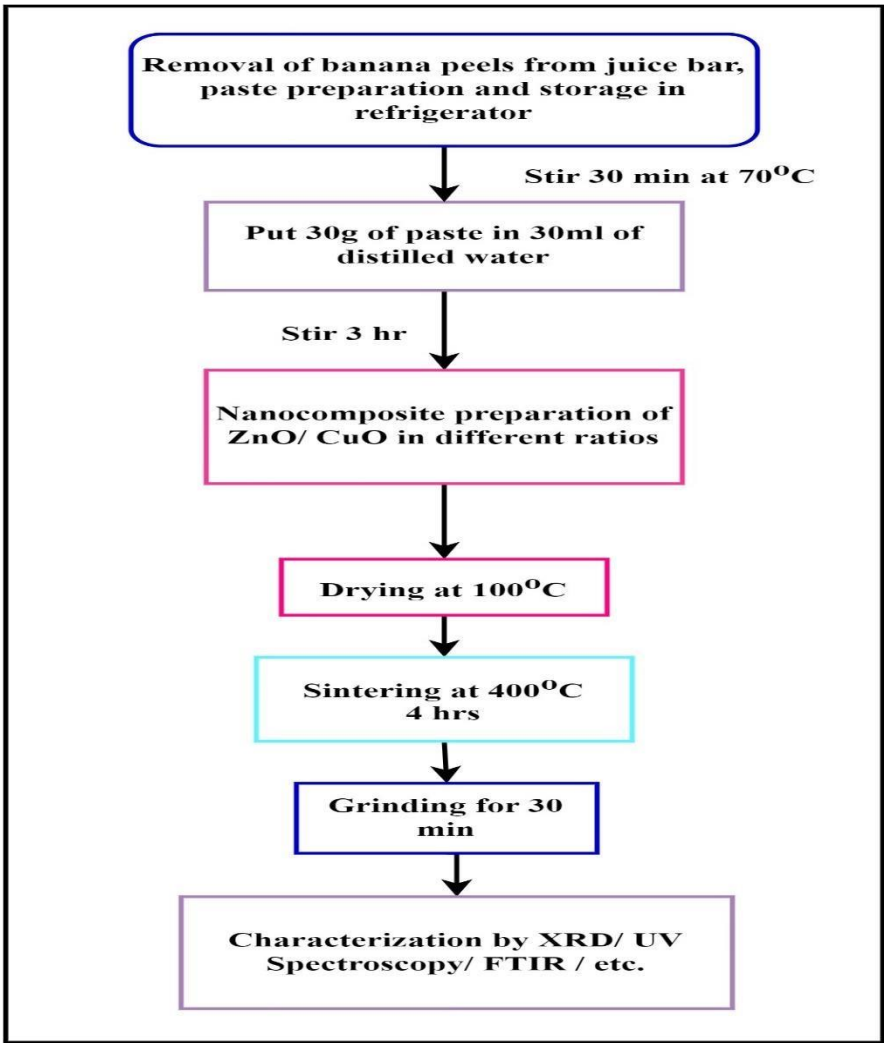

Fig 3.4. Typical flowchart for the synthesis of nanocomposite of CuO-ZnO by green synthesis method.

3.4.3. Synthesis of terbium-doped CuO/ZnO and cobalt-doped CuO/ZnO metal oxides nanocomposite.

The synthesis involved the use of various chemical precursors in carefully controlled amounts to prepare doped materials. A constant mass of 30 grams of organic peels was utilized as a sustainable base material in each batch. The primary metal precursors included cupric nitrate trihydrate ($Cu(NO_3)2{\cdot}3H_2O$and zinc nitrate hexahydrate ($Zn(NO_3)_2{\cdot}6H_2O$), which were varied in concentration depending on the desired dopant level. For the synthesis of ZnO/CuO nanocomposite (ZnO 20 wt% and 80 wt%) , 0.18 g of cupric nitrate trihydrate and 0.72 g of zinc nitrate hexahydrate

were used, corresponding to a dopant concentration of 0.1 % terbium/cobalt (Tb/Co) as describe in table 3.5. Similarly for the other proportions of ZnO/CuO nanocomposites as describe in table 3.5. Figure 3.5 also, depicts the schematic steps involved in doped Tb in CuO/ZnO synthesis. 30 g of banana peels were added in the 30 ml of distilled water and was stirred for 3 hours at 70℃. The obtained paste was dried at a temperature of 100℃ to obtain a powder. This dried powder was then sintered at 400℃ for 4 hours and later hand ground for 30 min. XRD, FESEM, EDX, UV-Vis, FTIR and fluorescence spectroscopy techniques were then used for characterization process. The synthesis of cobalt-doped CuO/ZnO nanocomposite follows similar steps, as mentioned above for the terbium- doped CuO/ZnO.

Table 3.5. Summary of amount of precursor used and yield of Tb/Co-doped CuO/ZnO nanocomposite sintered at 400^0C.

S. No.	**Mass of peels (g)**	**Cupric Nitrate Trihydrate(g)**	**Zinc Nitrate Hexahydrate(g)**	**Dopant Tb/Co mol %**	**Yield (g) Tb doped CuO/ZnO**	**Yield(g) Co-doped CuO/ZnO**
1.	30	0.18	0.72	0.1	0.8	0.7
2.	30	0.14	0.56	0.3	0.7	0.8
3.	30	0.10	0.50	0.5	0.7	0.5
4.	30	0.06	0.24	0.7	0.6	0.6

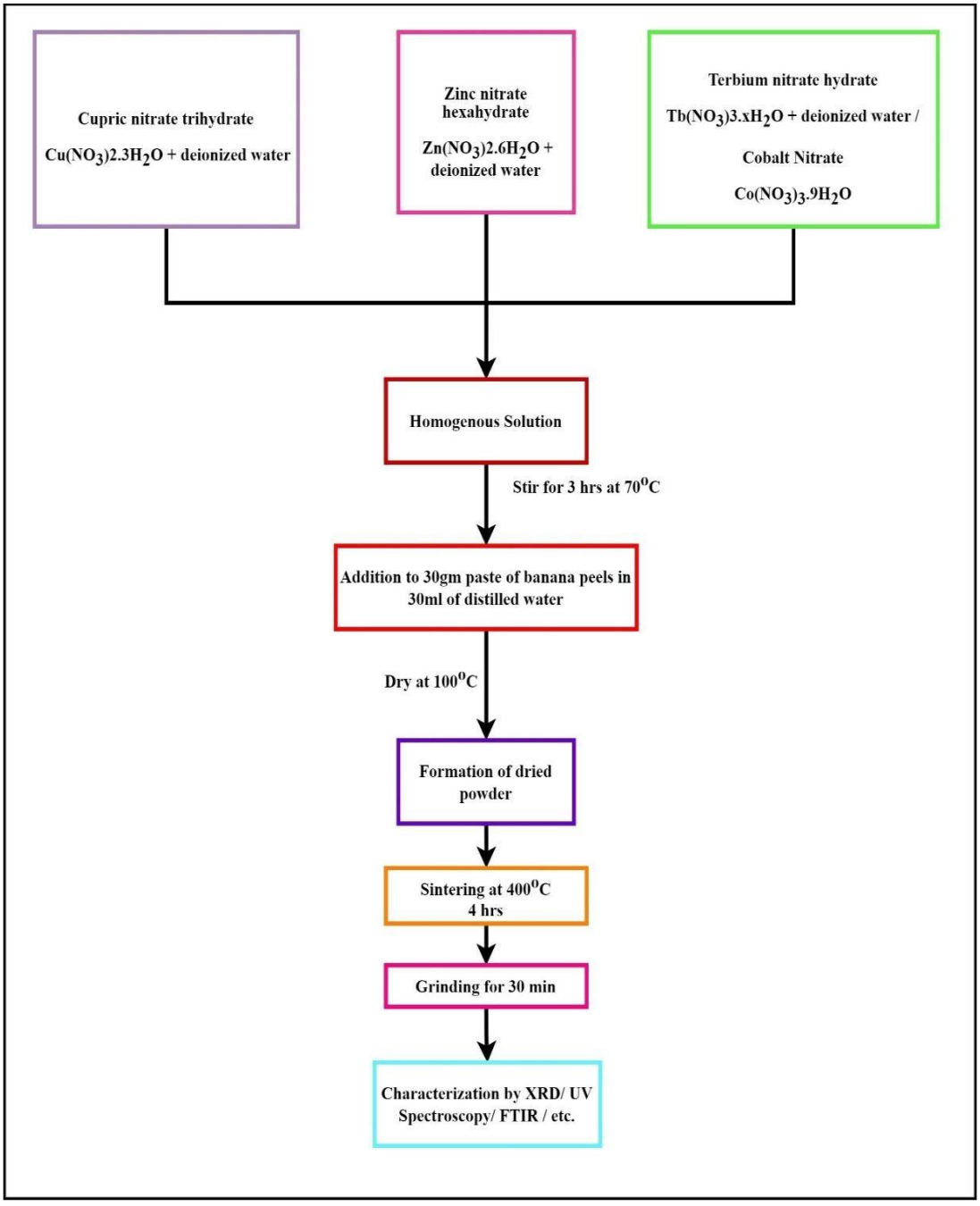

Fig 3.5. Flowchart representation of the synthesis of Terbium/Cobalt doped CuO/ZnO nanocomposite

3.5. Characterization techniques

All these experiments have been performed in the research Lab of Lovely Professional University (LPU) ,Phagwara,Punjab. Characterization was done at CIF of

LPU. Both structural as well as optical properties were evaluated using several techniques such as FTIR, XRD, UV-VIS absorption spectroscopy, SEM, EDX, and Fluorescence spectroscopy techniques. Various instruments that were used for characterization are outlined in the sections below.

3.5.1. X-Ray Diffraction

X-ray diffractometer:

This instrument is used in the field of materials sciences that determine the crystallographic structure of a material. XRD functions by irradiating a material with X-rays, which are later measured for their intensity and scattering angles. The major application of the technique is to identify materials based on diffraction patterns. XRD technique helps to study the shape, size of crystallite size and internal stress in the material technique based on the principle of Bragg's Law. It explains the interference pattern of scattered X-rays through a crystal. In 1912 Max von Laue and his team, a ground-breaking finding that materials crystalline in nature serve as 3-D X-ray diffraction gratings with wavelengths like distances between planes in crystal lattice [5]. XRD is a commonly utilized method for atomic spacing calculations and crystal structure analysis nowadays. If all the conditions of Bragg's law are satisfied, constructive interference, also known as diffracted rays, is obtained from the interaction between the sample and X-rays [6]:

$$n\lambda = 2d \sin\theta \text{ ---------- (3.1)}$$

In this equation,

d stands for distance between diffracting planes

θ stands for incident angle

n stands for integer

λ stands for beam wavelength.

In X-ray crystallography, the **Scherrer equation** is a formula which helps to find size of crystallite in any solid. The equation can be represented as:

$$D = k\lambda/\beta\cos\theta \text{ ---------- (3.2)}$$

Here

D stands for crystallite's size,

k stands for dimensionless shape factors.

The value of k is approximately 0.9, though it can differ depending on the specific crystallite shape. λ refers to wavelength and is equal to 1.54 Å. Full width at half maximum β; the value of β should always be expressed in radians.

The link between a crystalline material's wavelength, diffraction angle, and lattice spacing is established by Bragg's law which is the working principle of XRD. There is a detection, processing, and counting of the diffracted X-rays. Because of the powdered sample's random orientation, all potential diffraction directions are investigated by scanning a range of 2θ angles. It is possible to transform the resultant diffraction peaks into d-spacings, which are particular to every compound. To identify the compound, these values are compared to industry standard reference patterns. Fig. 3.6 shows the working principle of X-ray diffraction.

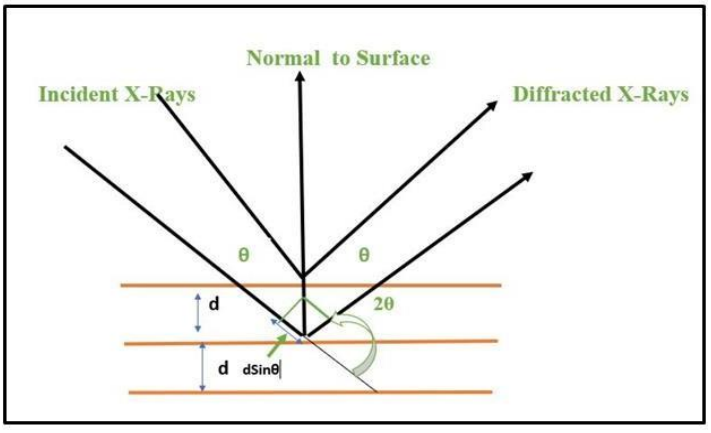

Fig 3.6. Working principle of X-Ray diffraction

XRD utilizing Cu-Kα radiations was conducted with a Bruker Diffractometer in the 20^{o}–80^{o} range. Fig. 3.7 displays the image of the Diffractometer along with the XRD pattern that was obtained from the sample.

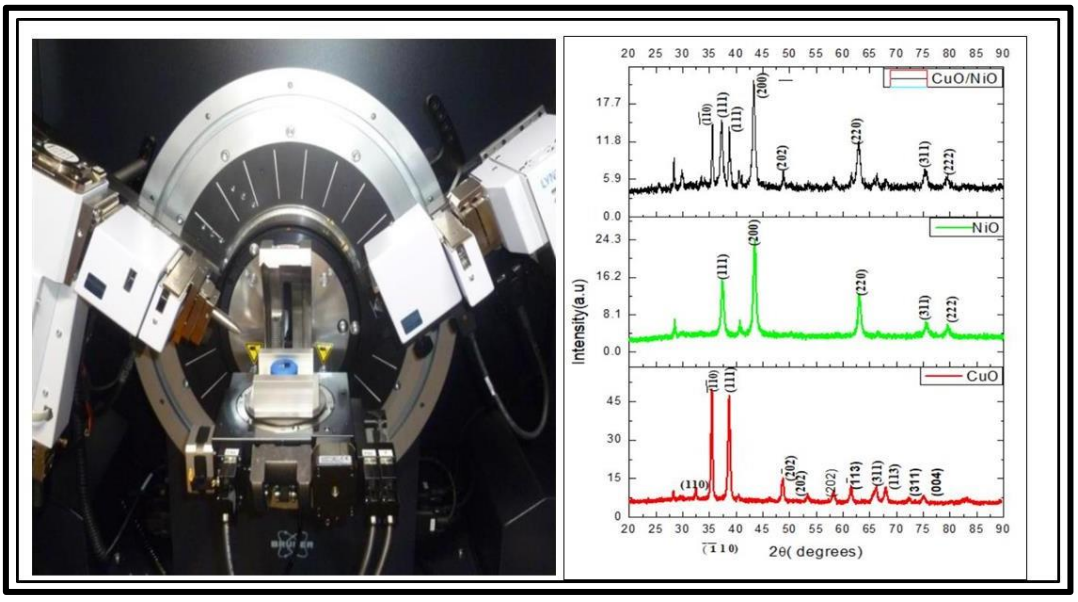

Fig 3.7. Instrumental image of X-ray Diffractometer and results of XRD pattern of CuO, NiO and CuO/NiO nanocomposite at 400℃ [11, 12]

3.5.2 Fourier-Transform Infrared Spectroscopy (FTIR)

FTIR technique is a method which is utilized to evaluate basically the absorption/emission of infrared light by a material of any state [7]. Dispersive spectrometers measure across a limited frequency range, but FTIR spectrometers concurrently collect comprehensive data over a broad spectral range (from 4000 to 400 cm^{-1}). FTIR estimate the amount of light absorbed by the sample by using a wide range of frequencies at once. After that, another data point is obtained by adjusting the light to consist of different frequency combinations. Fig. 3.8 represents the working principle of FTIR

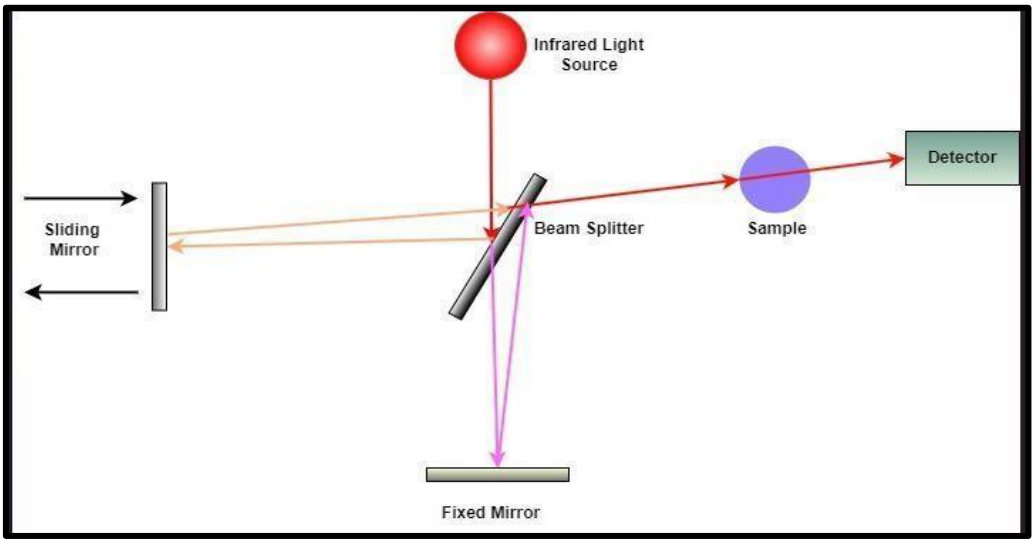

Fig 3.8. Working Principle of FTIR

A broadband light source containing all the frequencies to be measured is used to create an interferogram. A Michelson interferometer is used to measure light intensity. It consists of a set of mirrors, one of which is motorized. The output light beam changes its frequency composition every time the mirror moves because each light frequency is either blocked, changed, or transmitted at different rates.

To record the FTIR spectra, the PERKIN ELMER spectrometer was used. The spectrum was recorded in the range of 400-4000 cm^{-1} in air by pressing a combination of sample and KBr in the form of a pellet, following the conventional KBr pellet method. Infrared spectroscopy, also known as vibrational spectroscopy, is employed for investigating the chemical composition of samples. IR radiation interacts with the sample, resulting in an infrared spectrum. This approach is primarily utilized to identify the functional groups within molecules. IR spectroscopy detects atomic vibrations, which allows for the identification of functional groups based on those vibrational patterns. For example – If IR rays pass through ZnO two regions will be seen in the graph, functional group region and Fig print region. FTIR spectroscopy helps us to identify the fingerprint region because every compound has its unique fingerprint region. FTIR provide excellent analysis at both quantitative and qualitative

levels for inorganic as well as organic samples. FTIR is applied in the identification of chemical bonds and this information is used for finding functional groups and for the analysis of covalent bond-related information. When different approaches are used FTIR can provide additional information about the molecular structure of the particle. FTIR analysis has been used to discover unknown materials. Fig. 3.9 displays the image of the FTIR spectrometer along with the FTIR spectrum that was obtained from the sample.

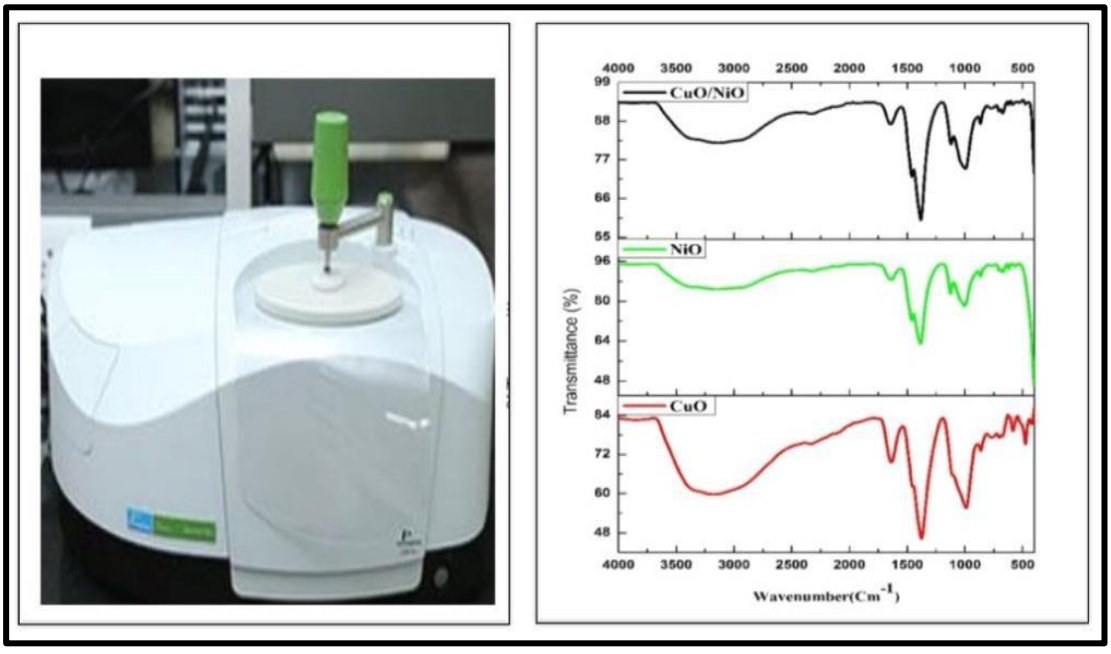

Fig 3.9. Instrumental image of FTIR spectrometer and results of FTIR spectrum of CuO, NiO and the nanocomposite of CuO/NiO at 400°C [11, 12]

3.5.3. FESEM

FESEM is an advanced technique that produces a three to six times better spatial resolution image of the material than traditional Scanning Electron Microscopy (SEM), with a clearer and less distorted image at high magnification and unlimited depth of field [8]. In addition, FESEM can use Energy Dispersive Spectroscopy (EDX) to investigate contaminant areas with a smaller area at electron-accelerating voltages. Using an Electron Back Scattered Detection System (BDS) mounted on a microscope, EDX is also utilized to provide information on crystalline materials at a

few nanometers below the surface. The JEOL JSM-7610F plus Field Emission Scanning Electron Microscope (FESEM), with a magnification range of 25 to 1,000,000, was used to assess the morphology of the produced samples. Fig. 3.10 below shows the image of the FESEM instrument together with the material's matching data.

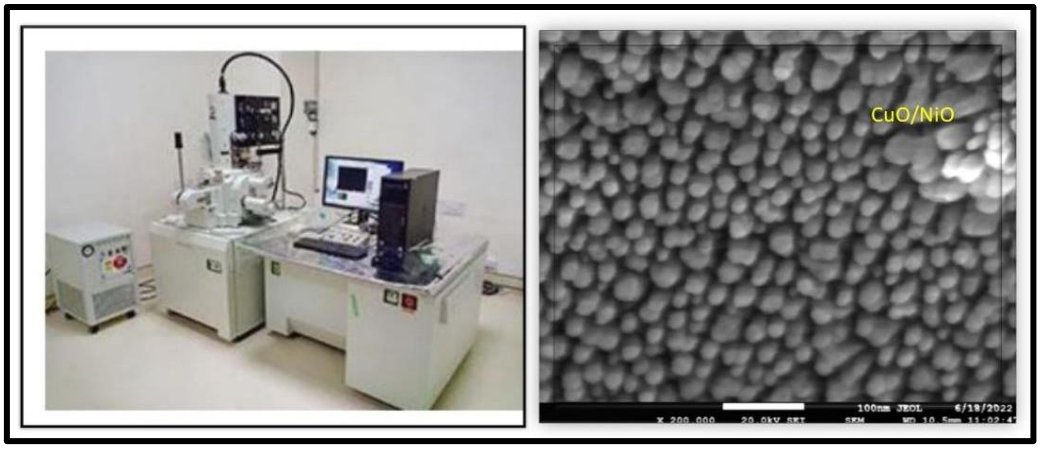

Fig 3.10. Instrumental Image of FESEM and view of results obtained from SEM of CuO/NiO nanocomposite at 400^0 C [11]

3.5.4 Ultraviolet-Visible (UV-Vis) Spectroscopy

This is a type of absorption spectroscopy in part of two regions of the electromagnetic spectrum - ultraviolet and visible. Absorption shown by visible rays affects the chemicals' color [9]. Both atoms as well as molecules of this region of the spectrum undergo electronic transition. UV range extends from 180-400nm. The visible range extends from 400-800 nm. Most of the instruments cover 180-800nm region. The technique is known as molecular absorption spectrophotometry or spectrophotometry. The color of the wavelength emitted in the visible region is due to the absorption or reflectance due to the chemicals used. It frames the premise of examination of different substances, for example, inorganic, organic and biochemical. Fig 3.11 represents the working principle of the UV-Vis absorption detector.

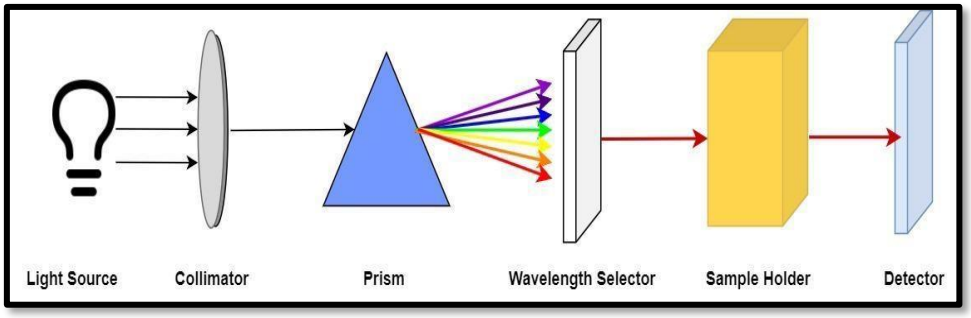

Fig 3.11. Working principle of UV-Vis absorption detector .

The energy needed for raising an electron from a lower energy level to a higher one is carried by the wavelength of absorbed light. Since the absorbance of light is proportional to the sample's concentration and path length, Beer-Lambert's equation shows that a wider difference between both energy levels will demand a higher quantity of energy for transition.

$\alpha = \varepsilon L c$ …… (3.3)

where L is the path length or the distance that light travelled through the material, ε is the proportionality coefficient, c is the amount of sample or the concentration of absorbing species, and α is the amount of light absorbed. The optical band gap was calculated using the Wood-Tauc method and the Kubekla-Munk function, which was developed from the theory of researchers, F. Munk. and P. Kubelka.

The wood-Tauc formula is as follows:

$\alpha h\nu = A(h\upsilon - Eg)^{\eta}$ ..... (3.4)

Here in the equation, α is the coefficient of linear absorption, E_g refers to optical bandgap energy, whereas A is constant. "n" value determines the type of transition; for example, if the number is ½, it indicates a direct transition; if the value is 2, it indicates an indirect transition.

The Shimadzu UV-Vis Spectrophotometer has been utilized in the UV-Vis spectroscopy characterization of different samples. The image of the apparatus and its corresponding results are given in Fig 3.12.

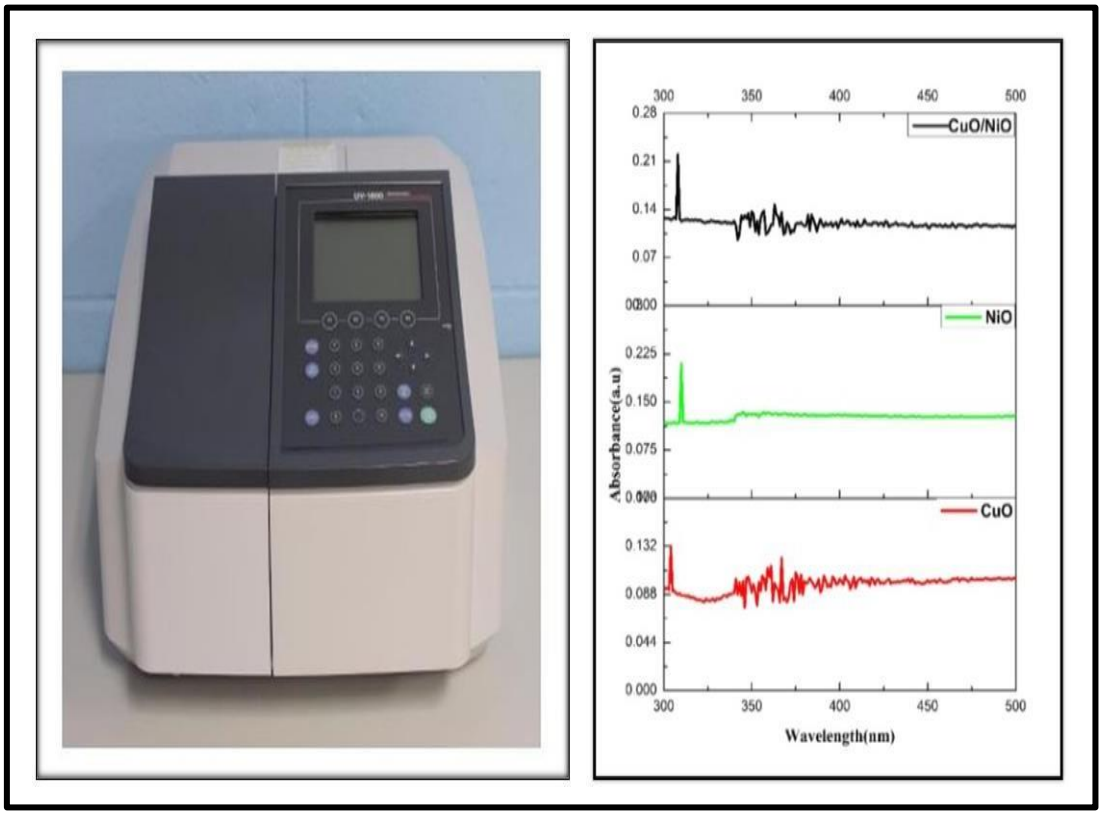

Fig 3.12 Instrumental image of UV-Vis spectrometer and results of the absorption spectrum of CuO-NiO at 400℃ [11]

3.5.5. Fluorescence Spectroscopy

Fluorescence spectrophotometry operates on the principle that when a substance absorbs light, its molecules become energized and transition from their ground state to an elevated energy state [10]. Usually, heat is released by the molecules as they approach their ground state. A part of the absorbed energy does, occasionally, reemerge as light, usually with a larger wavelength than the initial excitation light. We call this type of light emission fluorescence. This reemitted light is measured using fluorescence spectrophotometry, which analyses the substance's characteristics. Fig 3.13 shows the working principle of Fluorescence spectrophotometry and

Jablonski’s diagram.

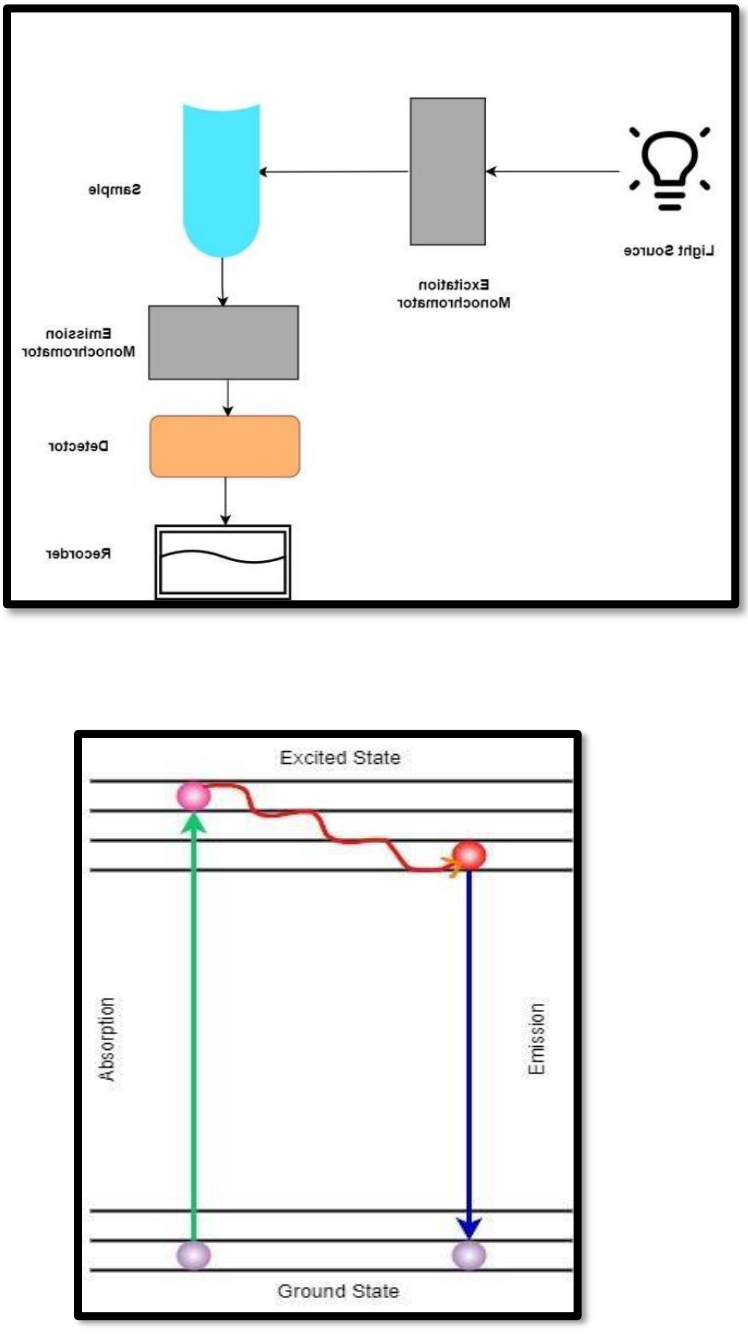

Fig 3.13 (a) Working principle of fluorescence spectrophotometer (b) Jablonski “s diagram

Fluorescence spectrophotometers can be divided into two categories: those that measure fluorescence lifetimes and those that measure steady-state fluorescence. Both versions have the same fundamental architecture, despite the differences in measurement. After passing via a monochromator to determine excitation wavelength, the light source is straight away focused onto a given sample. To prevent detecting light that goes through the sample directly, fluorescence is detected at a 90-degree angle from the excitation light. After that, fluorescence is focused on a second monochromator to choose a desirable wavelength, and a photomultiplier tube (PMT) is employed for measuring it. The intensity of light as well as bandwidth is controlled by movable slits on both the emission and excitation sides.

All the produced materials had their fluorescence characterized using a PERKIN ELMER spectrometer, which uses a xenon lamp with an excitation and emission range of 200–900 nm. The image of the apparatus and its corresponding results are given in Fig 3.14.

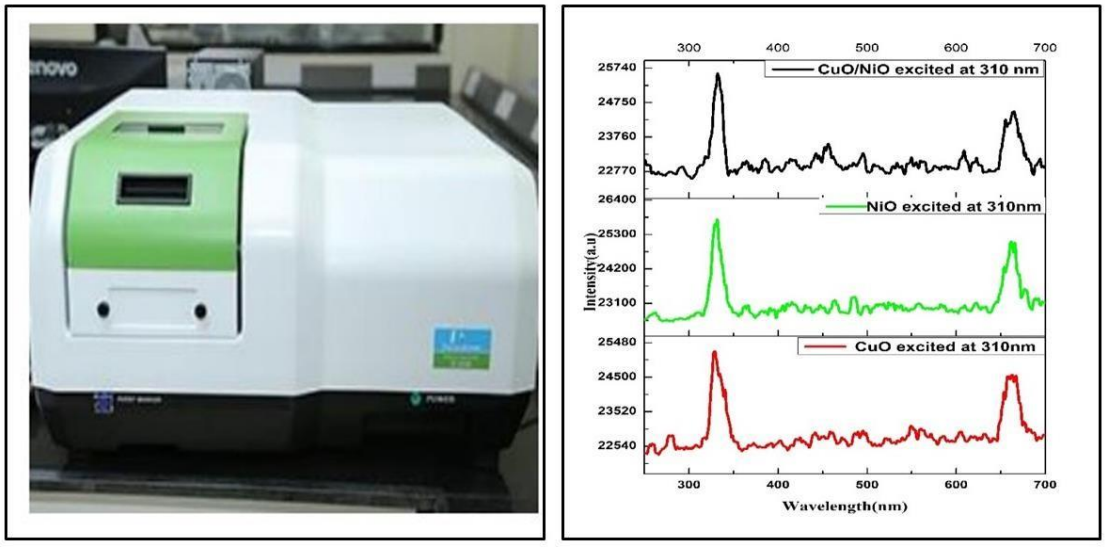

Fig 3.14 Instrumental image of fluorescence spectrophotometer and results of spectrum of CuO-NiO at 400℃ [11]

References:

1. N.A.N. Mohamad, N.A. Arham, J. Jai, and A. Hadi, “Plant extract as reducing agent in synthesis of metallic nanoparticles: a review,” Advanced Materials Research **832**, 350–355 (2013).
2. S. Yallappa, and J. Manjanna, “Biological Evaluation of Silver Nanoparticles Obtained from T. arjuna Bark Extract as Both Reducing and Capping Agent,” Journal of Cluster Science **25**(5), 1449–1462 (2014).
3. H.A. Mahfouze, N.K. El-Dougdoug, and S.A. Mahfouze, “Virucidal activity of silver nanoparticles against Banana bunchy top virus (BBTV) in banana plants,” Bulletin of the National Research Centre/Bulletin of the National Research Center **44**(1), (2020).
4. N.P. T-Thienprasert, J. T-Thienprasert, J. Ruangtong, T. Jaithon, P.S. Huehne, and O. Piasai, “Large Scale Synthesis of Green Synthesized Zinc Oxide Nanoparticles from Banana Peel Extracts and Their Inhibitory Effects against Colletotrichum sp., Isolate KUFC 021, Causal Agent of Anthracnose on Dendrobium Orchid,” Journal of Nanomaterials **2021**, 1–10 (2021).
5. A. Authier, “Dynamical theory of X-ray diffraction,” International Union of Crystallography, 534–551 (2006).
6. G.E.M. Jauncey, “The scattering of X-Rays and Bragg’s law,” Proceedings of the National Academy of Sciences **10**(2), 57–60 (1924).
7. P.R. Griffiths, “Fourier Transform Infrared Spectrometry,” Science **222**(4621), 297–302 (1983).
8. R.P. Jaya, “Porous concrete pavement containing nanosilica from black rice husk ash,” Elsevier eBooks, 493–527 (2020).
9. H.-H. Perkampus, “UV-VIS spectroscopy and its applications,” Choice Reviews Online **30**(11), 30–6183 (1993).
10. M.J. Sanderson, I. Smith, I. Parker, and M.D. Bootman, “Fluorescence microscopy,” Cold Spring Harbor Protocols **2014**(10), 071795 (2014).
11. https://www.lpu.in/cif/ Lovely Professional University, “central Instrumentation

facility, assessed on 20th September 2024”

12. https://mrc.mnit.ac.in/Mnit_mrc/facilities Malaviya National Institute of Technology, “Materials Research centre accessed on 20th September 2024”

Chapter 4
METAL OXIDES FROM GREEN WASTE

4.1 Metal Oxides Synthesized from Potato Peels

In this chapter, we present the synthesis of metal oxides derived from the waste of various plant materials, specifically potato peels, banana peels, and peas peels. We discuss the significance of these metal oxides, which demonstrate distinct band gaps in the blue and red spectra, reflecting the properties outlined in Chapter 1. Additionally, Chapter 3 provides a thorough overview of the synthesis processes employed for the metal oxides, detailing the methodologies used to prepare the different metal oxides, which were subsequently sintered at 400°C. This approach not only highlights the potential of utilizing agricultural waste but is also suitable for the optical properties of the various metal oxides. The current research focuses on exploring the grow light applications. Using potato peels MOs such as CuO, NiO, ZnO, MgO, and Fe_3O_4 are synthesized and sintered at 400^0C. To study the structural and optical properties the samples are studied by using the techniques XRD, FTIR, fluorescence spectroscopy, UV absorption, and FESEM. Similarly, in chapter 4.2, we discuss the results obtained from metal oxides prepared using banana peels. The research highlights the large optical band gaps identified through UV absorption tests to enhance these metal oxides' optical characteristics for grow light applications. From our investigations, it was determined that banana peels yield the highest quantity of metal oxides compared to other plant waste materials. Given this advantageous yield, we have focused our research on developing nanocomposites exclusively from banana peels. The larger yield and exploring the unique properties of the metal oxides derived from banana peels could enhance the performance and applicability of the resulting nanocomposites. By concentrating on this material, we aim to optimize the synthesis processes characterize the resulting nanocomposites and study the structural and optical properties of the prepared samples. This targeted approach not only maximizes resource efficiency but also positions our research to make significant contributions to the field of sustainable materials development.

4.1.1 XRD Spectroscopy

The X-ray diffraction (XRD) patterns for the prepared metal oxides are shown in Fig 4.1, where the diffraction data was collected within a 2θ range of 20° to 90°. To calculate the crystallite size (D) of the materials, the Debye-Scherrer equation, presented in Equation 3.2, was employed. This formula provides an estimate of the average crystallite size based on the broadening of diffraction peaks in the XRD pattern. Additional information regarding the preparation of these metal oxides including the metal precursor salts used, the role of potato peel in the synthesis, and the resulting average crystallite size and crystal structures is summarized in Table 4.1. This table presents the details of the materials' synthesis process and the characteristics of the resulting metal oxide structures.

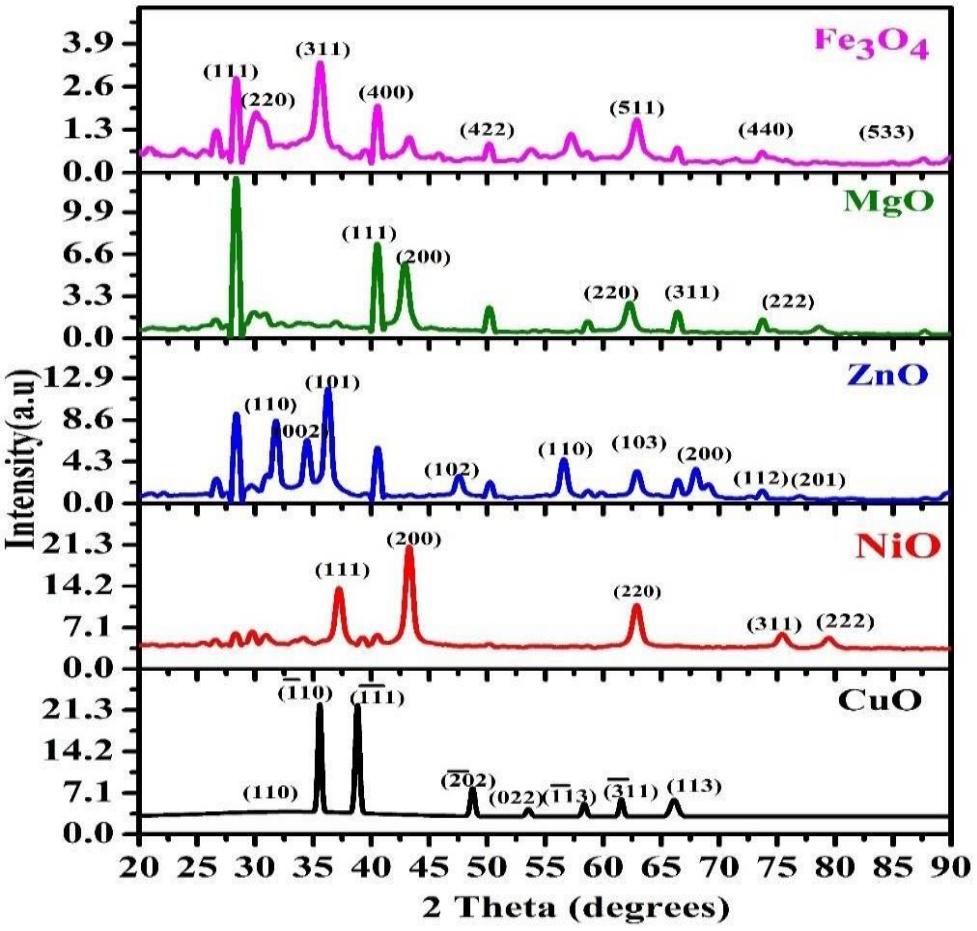

Fig. 4.1 XRD spectra of CuO, NiO, ZnO, MgO Fe_3O_4 metal oxides prepared from

potato peels and sintered at 400^0C

Table 4.1. Details of metal oxide prepared from potato peel, metal precursor Salt, average crystallite size and structure of the metal oxides.

S. No.	Metal Precursor	Metal oxide	Average crystalline Size(nm)	Crystal Structure	JCDPS Card no.
1	Cupric Nitrate Trihydrate	CuO	21.62	Monoclinic	80-1268 [1-4]
2	Nickel Acetate	NiO	12.34	face-centred cubic	00-0021216 [5-6]
3	Zinc Hexahydrate	ZnO	16.89	Hexagonal	00-036-1451 [7-9]
4	Magnesium Nitrate	MgO	19.59	Cubic	89-7746 [10]
5	Ferric Nitrate	Fe_3O_4	18.39	Cubic	85-1436 [11]

4.1.2 FESEM Analysis

The morphology of the prepared material is shown in Fig 4.2 and the FESEM data was used to determine the average grain size. For CuO, NiO, ZnO, and Fe_3O_4, the average particle size was determined to be 18.93 nm, 18.43 nm, 19.97 nm, 29.90 nm, and 20.22 nm, respectively. Metal oxides have spherical granules. As observed, the average grain size is marginally larger than the crystallite size, implying the presence of significant magnetic interactions. The morphology of all the synthesized materials is spherical, as shown in Fig 4.2. Fig 4.3 compares the crystallite size derived from

XRD with the particle size calculated via FESEM. From the analysis, the average particle size in the FESEM images is slightly greater than the crystallite size, indicating that varying crystal sizes interact magnetically, resulting in the formation of particles with diverse sizes.

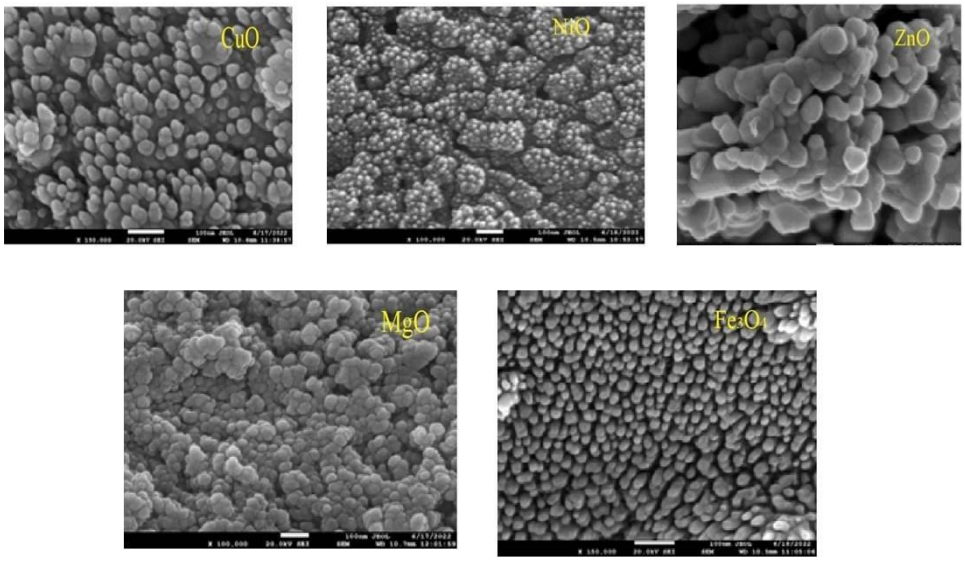

Fig. 4.2. FE-SEM micrographs of CuO, NiO, ZnO, MgO, and Fe_3O_4 metal oxides synthesized from potato peels and sintered at 400°C.

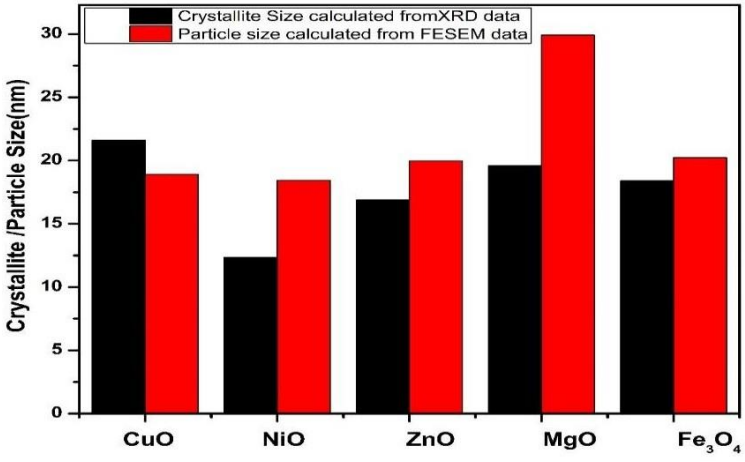

Fig. 4.3 FESEM micrograph and grain size distribution analysis of MOs prepared from potato peels annealed at 400^0C.

4.1.3 EDX Analysis

The elemental study of the prepared metal oxides is studied by using EDX. Additionally, elemental identification and quantitative compositional data are obtained using the EDX. The observed EDX analysis spectrum is displayed in Fig 4.4. and detailed elemental analysis are mentioned in Table 4.2. Energy-dispersive X-ray analysis is used to identify the elemental makeup of samples. Energy Dispersive X-ray Spectroscopy (EDX) was also employed to obtain quantitative compositional data of the synthesized metal oxides. Energy Dispersive X-ray (EDX) spectroscopy is a microanalytical technique that allows for the identification and quantification of elements within a sample by analyzing the characteristic X-ray emissions produced when the sample is irradiated with a high-energy electron beam. The interaction between the incident electrons and the atom in the material induces the ejection of inner-shell electrons, resulting in the excitation of the atom. When the atom returns to its ground state, X-rays are emitted, which are specific to the energy levels of the components present in the sample. By calculating the energy and intensity of these emitted X-rays, EDX provides precise information about the elemental composition, atomic distribution, and local stoichiometry, which is particularly valuable for confirming the metal-oxygen ratios and structural details in oxide materials.

Table 4.2. Elemental Composition of prepared metal oxides synthesized from potato peel.

S. No.	Element	Atomic %
1	O	47.12
	Cu	52.88
	Total	**100**
2	O	41.47
	Ni	58.53
	Total	**100**
3	O	55.80

	Zn	44.20
	Total	**100**
4	O	49.72
	Mg	50.28
	Total	**100**
5	O	52.26
	Fe	47.73
	Total	**100**

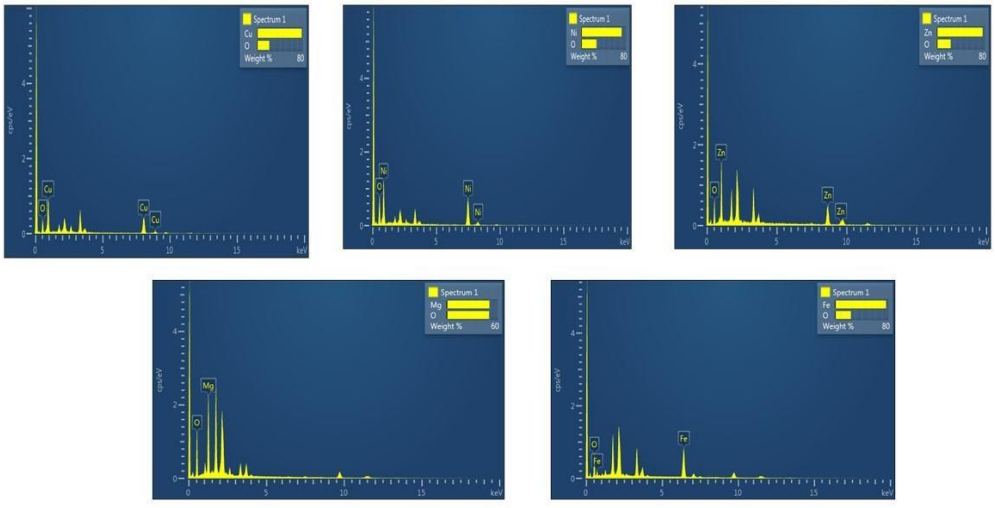

Fig. 4.4. EDX spectrum of CuO, NiO, ZnO, MgO, Fe_3O_4, metal oxides prepared from Potato peels and sintered at 400^0C.

4.1.4. FTIR Spectroscopy

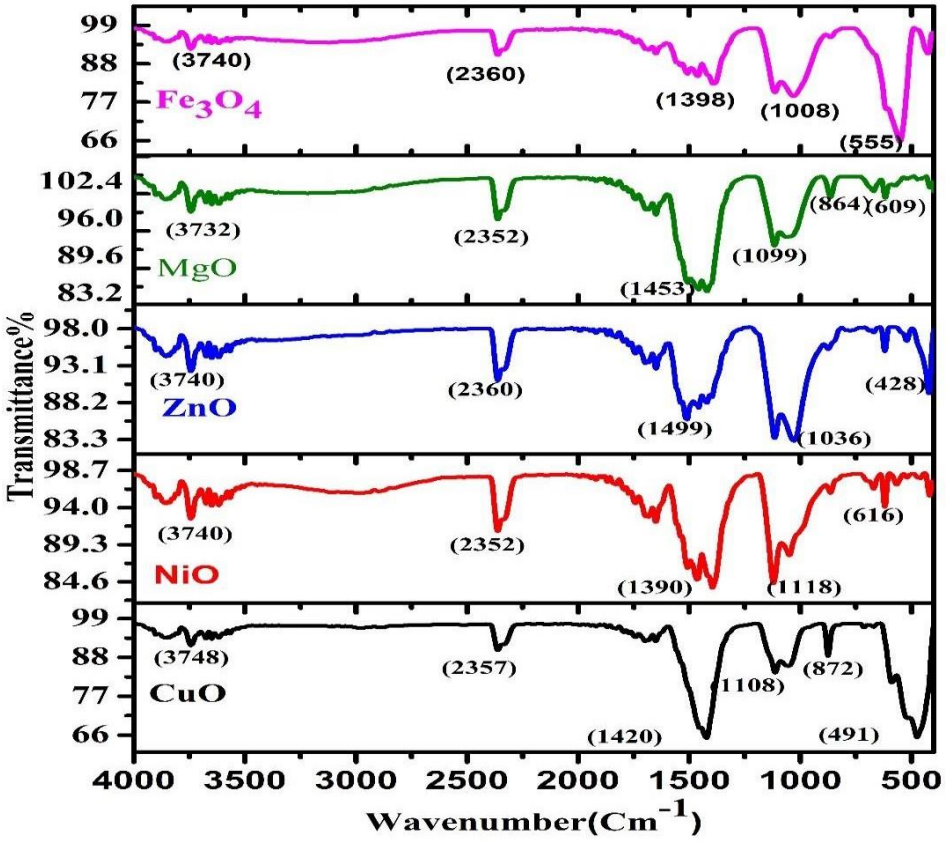

Fig. 4.5. FTIR spectra of CuO, NiO, ZnO, MgO, and Fe_3O_4 metal oxides synthesized using potato peels and sintered at 400°C.

The Perkin Elmer instrument was used to record the FTIR spectrum of metal oxides in the 4000-400 cm^{-1} region. The functional groups on the surface of the nanoparticles as well as different chemical bonds are analyzed by FTIR. Fig 4.5 displays the FTIR spectra of the metal oxides that were acquired from the potato peel extract. The creation of metal oxides is confirmed by the metal-oxygen bonds in 400–600 cm^{-1} Cu–O, Mg–O, Zn–O, Fe–O, and Ni–O. The bands at 3000–4000 represent O-H stretching cm^{-1} and O-H vibration. There are symmetric and asymmetric C-H bond peaks represented by the bands found at 2357, 2352, and 2360 [12-14].

4.1.5 UV Absorption Spectroscopy

The UV-visible absorption spectrum between 200-800 nm is recorded at room temperature and sintered at 400^0C. The metal oxides are prepared via green synthesis and the UV obtained spectra are shown in Fig 4.6. Equation 3.4 is used to calculate the optical band gap of the prepared sample material. Using Tauc's Fig 4.6 (b) the optical band gaps of the metal oxides made from potato peels were determined for CuO, NiO, ZnO, MgO, and Fe_3O_4 are 4.3, 2.7, 2.9, 3.2, 3,9 eV [15-19] respectively. Several factors, including lattice strain, structural characteristics, and the existence of various impurities present in the material, affect the material's optical band gap. It might be brought on by vacancies or chemical flaws in the intergranular regions, which would lower the band gap energy and produce a new energy level.

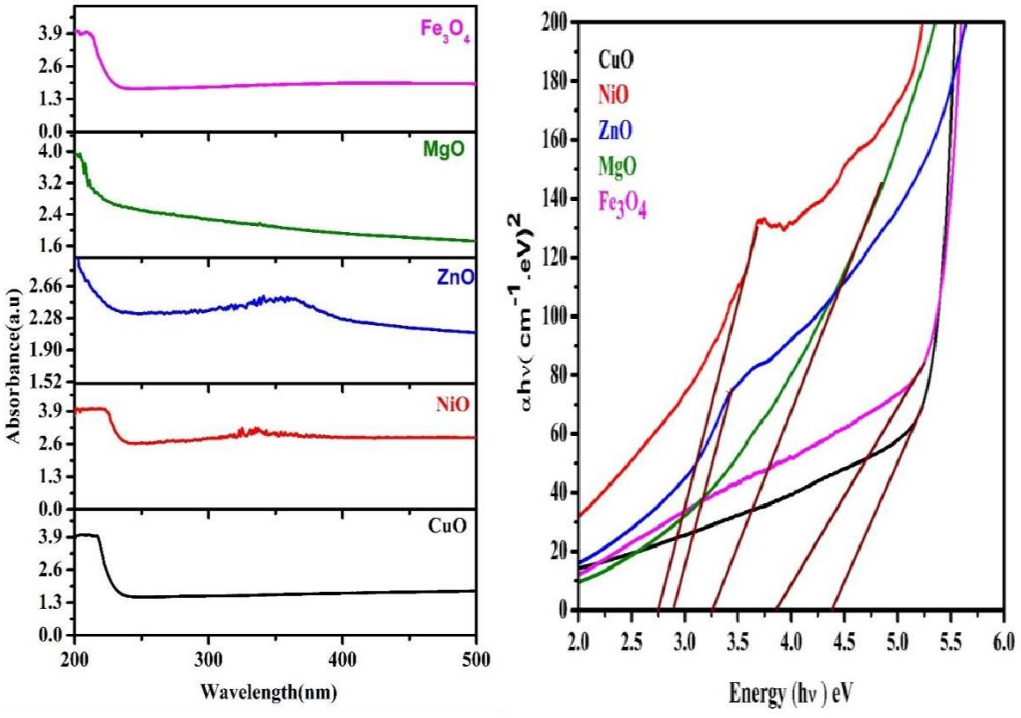

(a) **(b)**

Fig. 4.6 a) Plot of UV absorption spectra of metal oxides (b) Tauc plot of the obtained UV spectra prepared from potato peels and sintered at 400 ^{0}C.

4.1.6. Fluorescence Spectroscopy

According to the UV absorption spectra, each metal oxide is exciting at a different time. The optical characteristics of metal oxides made from potato peels are displayed in the emission spectra in Fig. 4.7. The UV emission peak for metal oxides was found to be between 400 -700 nm, and its growth light properties were investigated.

1. When excited at 210 nm, CuO exhibits emission peaks at 422 nm and 636 nm. The red-shifted peak at 636 nm and the blue-shifted peak at 422 nm suggest an increase in the bandgap due to stronger quantum confinement effects. The recombination of holes and electrons in copper oxide-free excitons, which are sensitive to particle size on the quantum scale, produces this near-band gap emission. The larger bandgap indicates that the energy gap of nanocrystalline semiconductor particles increases as the grain size decreases due to quantum confinement.
2. The emission spectra of NiO shows features associated with interstitial oxygen trapping and/or cation vacancies within the NiO lattice. The color change of NiO from greenish grey in its stoichiometric form to black in its non-stoichiometric form can be attributed to nickel vacancies and/or interstitial oxygen. Upon excitation at 335 nm, NiO displays a strong emission at 672 nm, corresponding to a red-shifted band edge at 3.58 eV.
3. The emission spectra of ZnO reveal defect-related peaks between 400 -700 nm. Excited at 400 nm, ZnO shows emission peaks at 418 nm and 437 nm, which are linked to defect states associated with zinc vacancies. Additional peaks at 466 nm and 492 nm are attributed to deep-level defect states caused by zinc interstitials and/or oxygen vacancies. The expected green emission (500-530 nm), typically attributed to singly ionized oxygen vacancies, is not observed in this study, suggesting that the sample is oxygen-rich. The absence of green emission indicates that enough oxygen is present to compensate for the singly ionized oxygen vacancies. The peak at 400 nm is thought to result from electron transitions from a localized level just below the conduction band to the valence band.
4. The fluorescence spectrum of MgO, excited at 253 nm, shows a single peak at 507 nm, confirming the formation of defect-free MgO.

5. For Fe_3O_4, when excited at 210 nm, the emission peaks are observed at 419 nm and 628 nm, corresponding to blue and red-shifted emissions, respectively. The red- shifted peak at 628 nm and the blue-shifted peak at 419 nm suggests that the bandgap has widened due to an enhanced quantum confinement effect.

The fluorescence spectra analyses indicate that the metal oxides CuO, NiO, ZnO, and Fe_3O_4 exhibit both blue and red emission, making metal oxides appropriate for the grow light spectrum. These metal oxides are being investigated further for use in grow light applications. Grow light spectrum is a type of light spectrum used in horticulture to promote plant growth and optimize plant production. These spectra are designed to provide the specific wavelengths of light that plants require for photosynthesis and growth [31-35]. For example, young seedlings need more blue light to promote vegetative growth, while flowering and fruiting plants need more red light to promote flower and fruit development. The most commonly used grow light spectra are full-spectrum, red-blue spectrum, and white light. Full-spectrum grow lights provide a wide range of wavelengths similar to natural sunlight, while red-blue spectrum grows lights provide a higher concentration of blue and red wavelengths. White grow lights provide a balanced combination of all wavelengths, which can be customized using filters or other methods. In addition to promoting plant growth, grow light spectra can also be used to manipulate plant morphology, such as increasing leaf size or promoting branching. This is accomplished by adjusting the ratio of blue to red light, which can influence plant growth and development in specific ways.[35]. All things considered, growth light spectra are a useful instrument for indoor plant cultivation and horticulture.

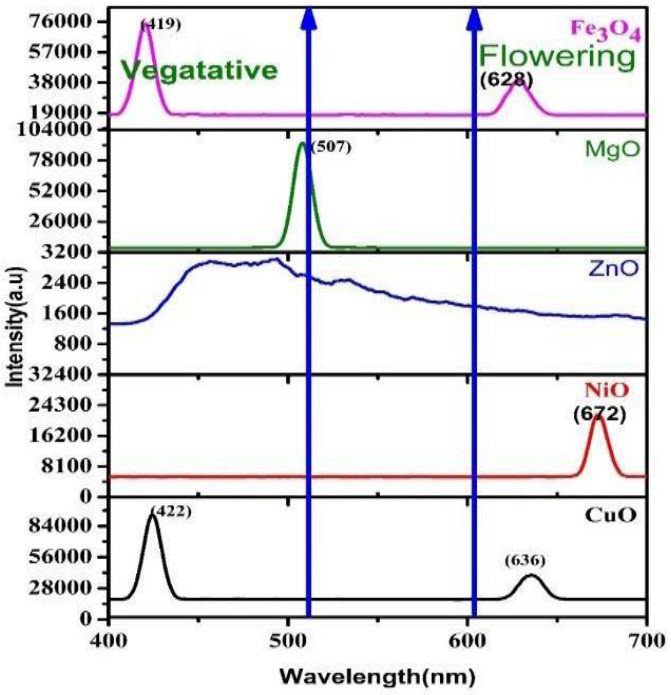

Fig. 4.7. Fluorescence Spectra of CuO, NiO, ZnO, MgO, Fe_3O_4 metal oxides prepared from potato peels excited at 210nm and sintered at 400^0C.

Nearly 20% more energy was used for household and industrial use because of the need for energy-efficient white light sources. White light sources therefore need to be made of efficient materials. The quantitative metrics used to assess the material potential as white light are CIE 1931 coordinates, CCT, and CRI. To investigate the emission property of a light source, the researcher is interested in the x-y coordinates in the CIE 1931 space chromaticity diagram. The CCT coordinates, often referred to as correlated color temperature (CCT), is expressed in degrees Kelvin (K) and are linked to a reference source, which is heated to a specific temperature. The index for color rendering CRI is a quantitative method for determining how accurate a visible spectrum light source is. associated with the ideal light of the sun. For ideal daylight CIE coordinates, CCT and CRI are (0.33,0.33),5000K, and 100 respectively. Using the fluorescence data, the MOs' CRI, CCT, and CIE 1931 coordinates are computed [36] and compiled in Table 4.3. As seen in Fig. 4.8, the potential of prepared MOs as daylight material was determined by the computed values of CIE coordinates, CCT, and CRI being extremely close to ideal daylight. [37]. The computed CIE and CCT

coordinates for CuO, NiO, ZnO, MgO, and Fe_3O_4 are displayed in Table 4.3.

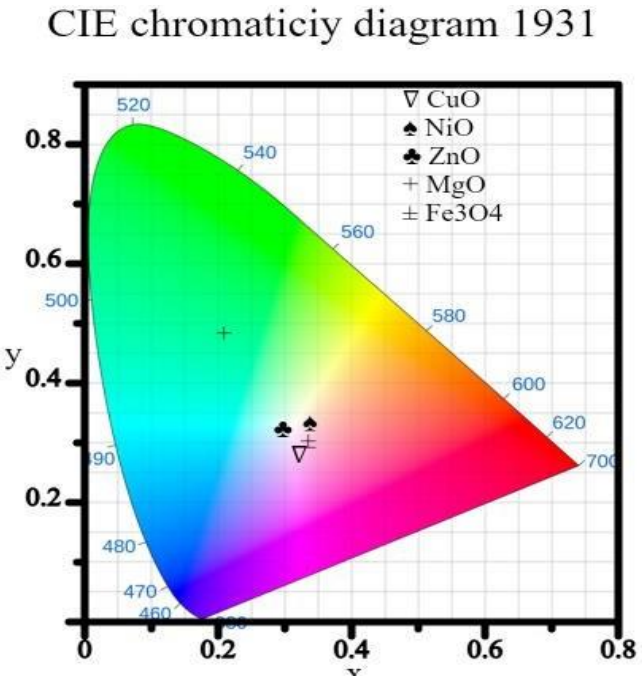

Fig 4.8 CIE coordinates of the metal oxides CuO, NiO, ZnO, MgO and Fe_3O_4.

Table 4.3 Calculated CIE and CCT coordinates of the CuO, NiO, ZnO, MgO and Fe_3O_4.

Metal Oxides NPs	**CIE (X, Y) coordinates**	**CCT (K)**	**CRI**
CuO	0.32,0.27	6360	71
NiO	0.33,0.33	5237	91
ZnO	0.33,0.33	5473	94
MgO	0.20,0.48	9021	42
Fe_3O_4	0..33,0.30	5285	77

4.1.7. Quantum Yield

Quantum yield is the ratio of emitted photons to absorbed excitation photons and is represented by φ(λ). It indicates the efficiency with which absorbed photons are converted into emitted photons. The quantum yield can be calculated using the

following equation: (4.3)

$$\varphi(\lambda) = QY_{ref} \frac{n^2}{n_{reF}^2} \frac{I}{A} \frac{A_{reF}}{I_{reF}} \text{ ---------- (4.1)}$$

where I is the integrated fluorescence intensity, QY ref is the quantum yield of the reference chemical, n is the solvent's refractive index, and A is the absorbance at the excitation wavelength. To minimize inner filter effects and provide a linear response on the intensity [38-39].

The significance of radiative to non-radiative processes of resonant emissions, such as resonance, downshifting, down-conversion, and up-conversion, is essentially stated by quantum yield. Instrument characteristics have no bearing on quantum yield, which quantifies how well a fluorophore converts the excitation light into fluorescence. When more than one molecule per photon decomposes, the quantum yield is high ($\varphi>1$); when fewer molecules per photon disintegrate, the quantum yield is low ($\varphi<1$). is less than one per photon since the quantum yield is less than 1. The predominance of the non-radiative process could be the cause. Additionally, the emission process is the outcome of down conversion, meaning that when activated by UV radiation, emission occurs in the visible region. Among all the metal oxides prepared NiO has the highest quantum yield which can be further improved by doping [40]. Fig 4.9 represents the measured quantum yield of metal oxides which were prepared from potato peels.

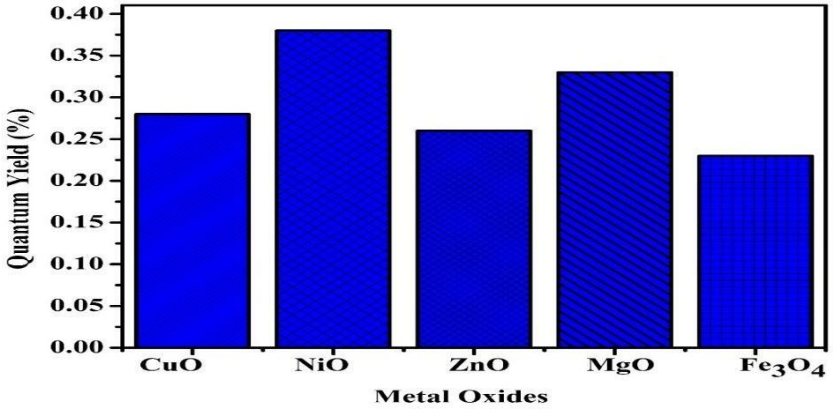

Fig. 4.9 Systematic representation of calculated quantum yield of metal oxides prepared from potato peels

4.2. Metal Oxide Synthesized from Banana Peels

4.2.1 XRD

To study the Phase analysis of prepared MOs prepared by using banana peels XRD were carried out for the samples. The XRD pattern of all the MOs has sharp peaks confirming the formation of crystalline nanomaterial. The Scherer formula was used to calculate the crystalline size of the sample material described in equation 3.2. Fig. 4.10 shows the XRD spectra of banana peels (BP) and metal oxides CuO, NiO, ZnO, Fe_3O_4 and MgO sintered at 400^oC in a muffle furnace.

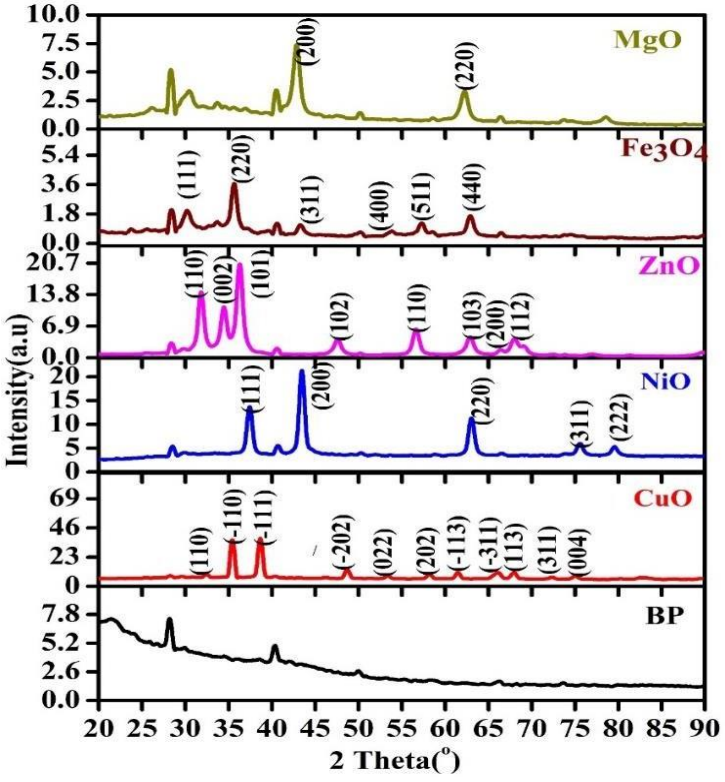

Fig. 4 .10 XRD spectra of BP, CuO, NiO, ZnO, Fe_3O_4, and MgO metal oxides annealed at 400^0C.

Table 4.4. Information on metal oxides synthesized from banana peel, including the metal precursor salt, average crystallite size, and crystal structure of the oxides.

S.no	Metal Precursor	Metal oxide	Average crystalline Size(nm)	Crystal Structure	JCDPS Card no.
1	Cupric Nitrate Trihydrate	CuO	18.89	Monoclinic	80-1268[1-4]
2	Nickel Acetate	NiO	11.27	face - centered cubic	00-0021216[5-6]
3	Zinc Hexahydrate	ZnO	10.78	Hexagonal	00-036-1451[7-9]
4	Ferric Nitrate	Fe_3O_4	16.93	Cubic	85-1436[11]
5	Magnesium Nitrate	MgO	9.84	Cubic	89-7746[10]

1. The Bragg's peaks of copper oxide CuO at 32.42, 35.43, 38.65, 48.68, 53.37, 58.20,

61.48, 66.03, 67.94 and 72.34 corresponding to the planes (110), (-110), (-111), (-202), (022), (202), (-113), (-311), (113), (311), and (004) respectively which confirmed the formation of monoclinic structure of CuO indexed by JCPDS card no. 80-1268 [1-4]. In the XRD pattern, there are no impurity peaks visible. The average crystalline size calculated by the Scherer formula (eqn.4.1) is 18.89nm.

2. In the XRD pattern of nickel oxide, the Braggs peaks lie at 37.42, 43.46, 63.04, 75.57 and 79.56 corresponding to the planes (111), (200), (220), (311) and (222), respectively. The data of the XRD pattern of NiO reveals the FCC (face-centered cubic) structure indexed by JCPDS card no. 00-002-1216 [5-6].The average

crystalline size of the sample material calculated by using Scherer's equation (4.1) is 11.27 nm.

3. The Bragg peaks observed for zinc oxide (ZnO) are located at 31.82°, 34.46°, 36.27°, 47.57°, 56.64°, 62.88°, 66.45°, 68.01°, and 69.13°, which correspond to the (110), (002), (101), (102), (110), (103), (200), (112), and (201) crystallographic planes, respectively. The XRD pattern confirms a hexagonal crystal structure for ZnO, consistent with JCPDS card no. 00-036-1451 [7-9]. Using Scherrer's equation (4.1), the average crystallite size of the sample is calculated to be 10.78 nm
4. Ferric oxide Fe_3O_4 nanoparticle prepared from the green synthesized by using the banana peel extract. The brag's peaks lie at 30.33,35.57,40.33,57.22.62.69 corresponding to the planes (220), (311), (400), (511), and (440) respectively. XRD pattern confirmed the formation of cubic inverse spinel structure of Fe_3O_4 indexed by JCPDS card no 65-3107) [11]. The average crystallite size of Fe_3O_4, is 16.93 nm.
5. The Bragg peaks of magnesium oxide MgO at 42.83 and 62.22 correspond to the planes (200) and (220) respectively. From the Obtained data of the XRD pattern, the structure of MgO reveals a cubic structure, indexed by JCPDS card no. 89-7746 [10]. The average crystalline size of MgO calculated by using Scherrer's equation is 9.84 nm.

4.2.2. FTIR Spectroscopy

The sample material contains a variety of chemical bonds that are studied using FTIR and the prepared metal oxides are studied using the FTIR spectra as shown in Fig.4.11. The absorption bands lie at various peaks, as seen in Fig 4.11. The metal-oxygen linkages, which have absorption peaks between 400 and 600 cm^{-1}, are represented by the metal-oxygen bonds Mg-O, Ni-O, Cu-O, Zn-O and Fe-O.C=O, are also present in the data, and there is broad absorption 3000-3500 Cm^{-1}, which is assigned to O-H and C-H bonds. [41-44]

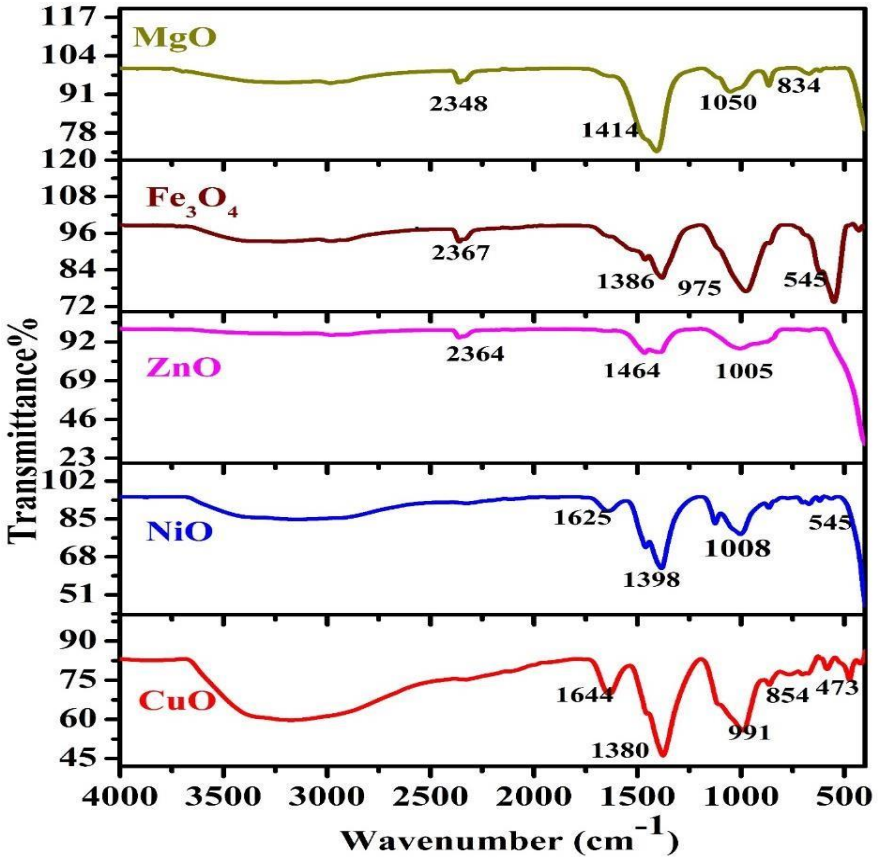

Fig. 4.11 FTIR spectroscopy of the metal oxides prepared from banana peels annealed at 400^0C.

4.2.3. FESEM study

The prepared MOs from the waste banana peels are also studied by using the structural technique FESEM which is displayed in Fig. 4.12 to examine the morphology of the metal oxides and average particle size utilizing the FESEM. The standard particle size was determined shown in Fig.4.12 by using the distribution curve which is represented in Fig 4.12. The particle size is 22.89 nm for CuO, 17.97 nm for NiO, 15 nm for ZnO, 17.96 nm for Fe_3O_4 and 13.87 nm for MgO which was calculated by ImageJ software and the histogram was plotted the origin software. The morphology of all the MOs prepared material is spherical is in shape as shown in Fig4.12 and Fig. 4.13 showing the comparison of crystallite size calculated from XRD and particle size measured from FESEM. As expected average size from the FESEM

is slightly larger than the crystallite size confirming that crystals of different crystallite sizes have strong magnetic interaction which forms particles of different sizes.

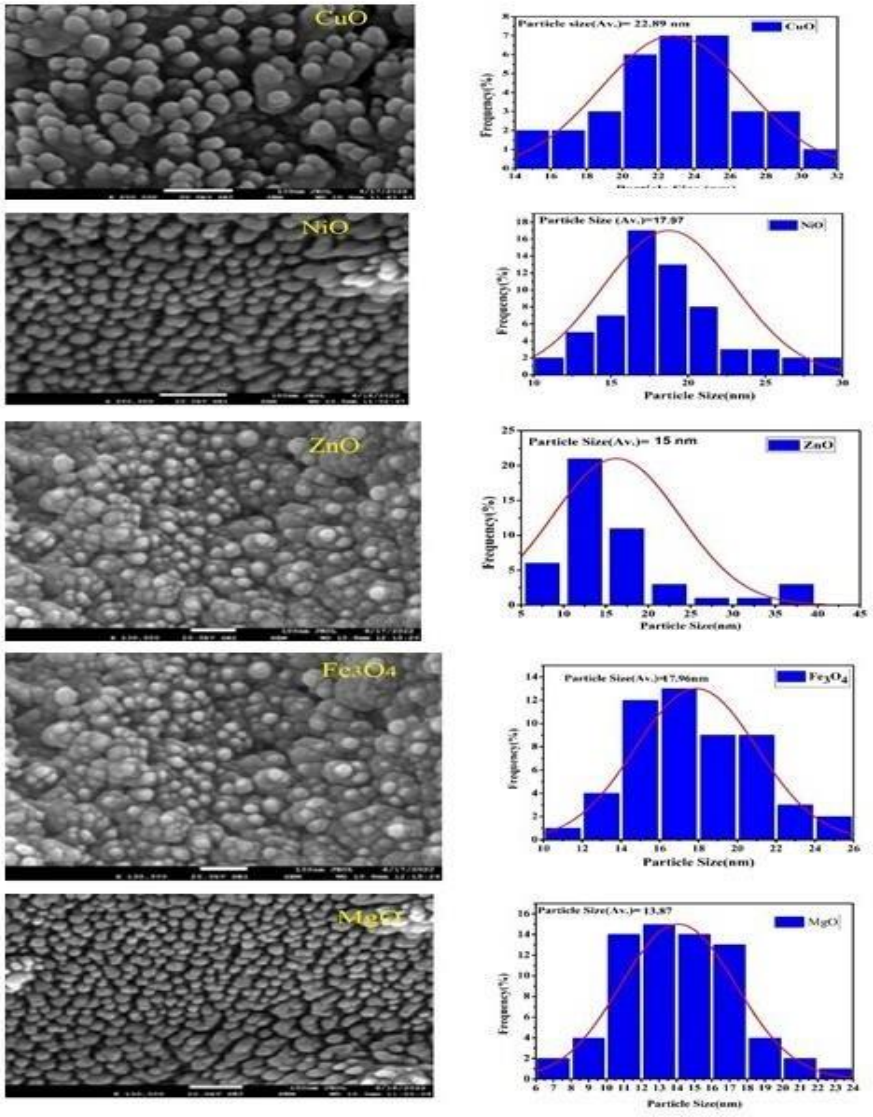

Fig. 4.12. Representation of FESEM images and distribution analysis of MOs prepared from banana peels annealed at 400^0C.

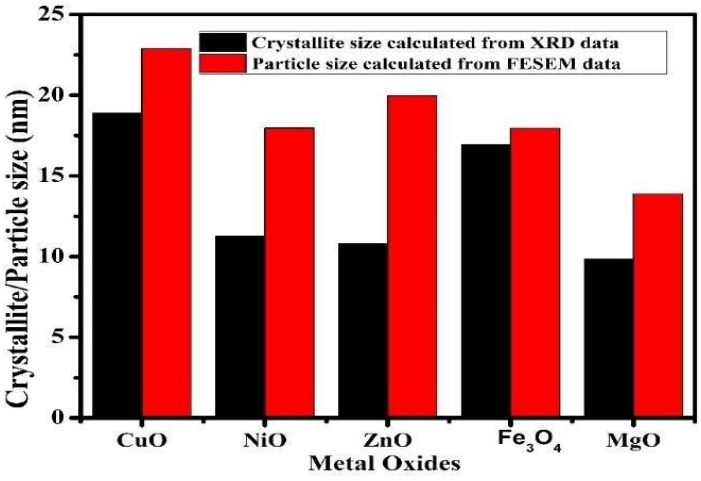

Fig. 4.13. The bar graph represents the Comparison of crystallite/particle size calculated from XRD and FESEM.

4.2.4 EDX Analysis

To determine the elemental composition of the produced samples, EDX analysis was employed. Metals, ceramics, minerals, and metal alloys can all be analyzed with EDX. Additionally, elemental identification and quantitative compositional data are obtained using the EDX. The EDX analysis observed spectrum for the prepared metal oxides CuO, NiO, ZnO, MgO, and Fe_3O_4 are shown in Fig.4.14. found that 52.89% of Cu and 47.11% of O, 58.51% of Ni and O 41.49%, Zn 44.15 %and O 55.85 %, Fe 47.73 and O-52.27, and Mg 50.23% and O 49.77% respectively. The elemental makeup of samples is determined via energy-dispersive X-ray analysis. Quantitative compositional data is also provided by EDX.

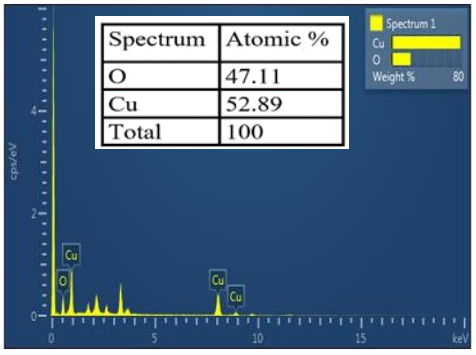

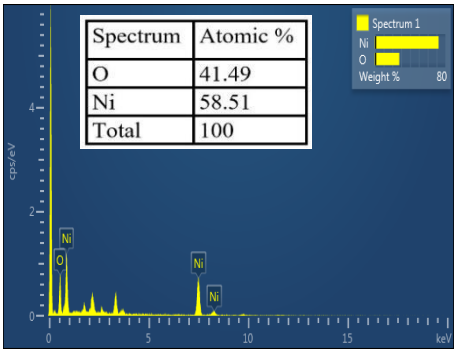

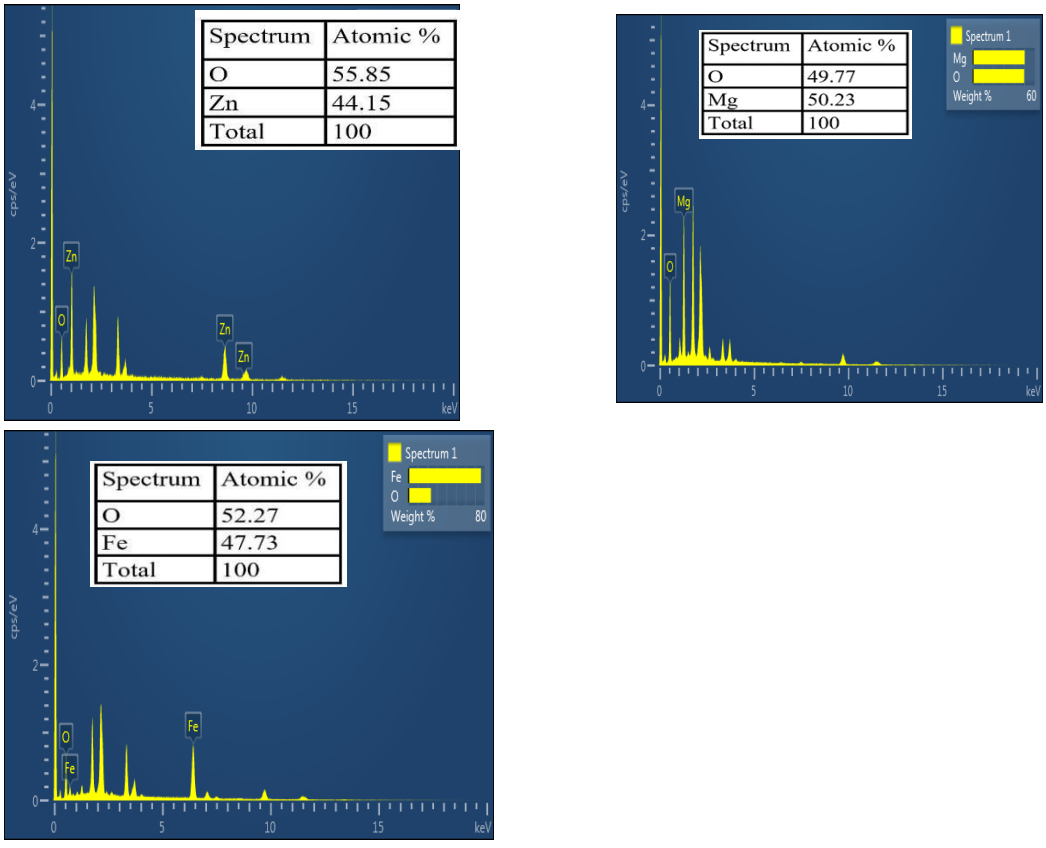

Fig. 4.14 EDX spectrum of CuO, NiO, ZnO, Fe_3O_4 and MgO metal oxides prepared from banana peels annealed at 400^0C.

4.2.5 UV Absorption

The PL and UV-Visible absorption spectra were used to optically characterize the nanoparticles. Fig 4.15 displays the nanoparticles' absorption spectra. UV-Vis absorption spectrum of the metal oxides prepared from green synthesis sintered at 400^0C. Equation 3.4 is used to determine the optical band gap energy of (Eg) of the produced nanoparticles from Tauc's plot and the obtained band gaps are listed in Table 4.4. The calculated band gap values are well-matched with the literature values.

Table 4.5. Calculated optical band gap (Eg) of the metal oxides prepared by using banana peels.

Sample	Eg(eV)	References
CuO	5.33	[44][45]
NiO	4.98	[46]
ZnO	5.0	[47] [48]
Fe $_3O_4$	5.24	[49] [50]
MgO	5.7	[51]

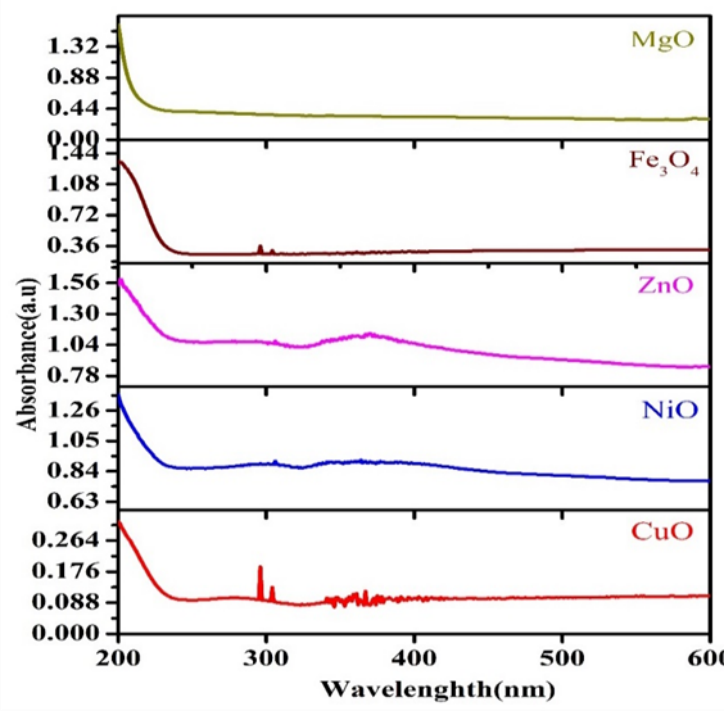

Fig. 4.15 UV-Vis spectroscopic analysis of CuO, NiO, ZnO, Fe_3O_4, and MgO metal oxide annealed at 400^0C.

4.2.6 Fluorescence Spectroscopy

The fluorescence spectroscopy of a powered sample of MOs CuO, NiO, ZnO, Fe_3O_4, and MgO made from banana peels and fused at 400°C was observed using a Perkin Elmer Spectrum in the 300-700 nm range. Fig.4.16 shows the fluorescence spectra (FS) of MOs excited by 310nm. FS has emissions from UV to visible region (300-700 nm). The visible region consists of red (620-720) nm, orange (590-620) nm, green (500-570) nm, blue (460-500) nm, and violet (400-446) nm color bands.

a) Copper Oxide (CuO)

The fluorescence spectrum shown in Fig 4.16 of CuO was examined, and the spectrum revealed a broad UV-Visible emission in the range of 200-400 nm shown in Fig 4.16. UV emission in the region 375-400 nm was caused by the recombination of electrons and holes in copper oxide and was attributed to a near band-edge emission. The emission peaks at 635-670nm red emission are less intense than the peak at 622nm [52-53].

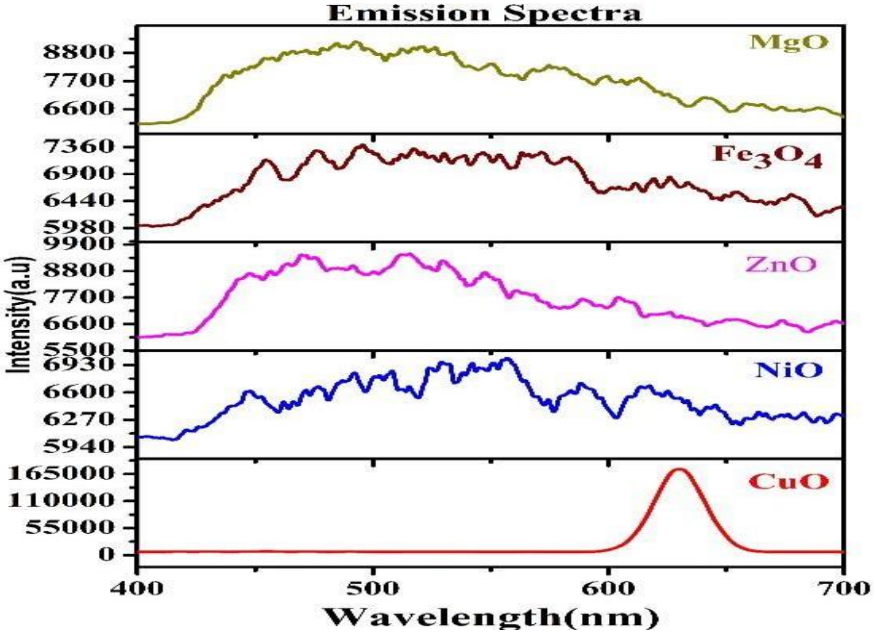

Fig. 4.16. Fluorescence Spectroscopy of CuO, NiO, ZnO, Fe_3O_4 and MgO metal oxides prepared from banana peels annealed at 400^0C.

b) Nickel Oxide (NiO)

The fluorescence Spectra of NiO was recorded at 400°C as shown in Fig 4.16 and all the prepared materials are excited at 310 nm. The observed emission spectra consist of multiple low-intensity peaks in the UV region extended to the visible region. The main high-intensity dominating peak is observed at 501nm. All these multiple peaks from the UV region extended to the visible region confirmed the presence of structural defects. Structural defects are oxygen vacancies and interstitial defects. The UV emission from the 330-400mm range originated from the excitonic recombination near the band edge(NBE). The blue emission at 470,475, 483, 489, and 501 nm arose as a result of doubly ionised Ni vacancy to holes in the valence band. In comparison to the other peaks, the intensity of the peak at 501 nm was extremely high.DLE defects states included 500, 527, 542, 548, 560, and 568 nm emissions which were attributed to the presence of Ni vacancy but green emissions due to oxygen vacancy can't be ruled out [54-59]. Ni vacancies were produced due to the charge transfer from Ni^{2+} to Ni^{3+}.

c) Zinc Oxide (ZnO)

ZnO is a well-known material with broad absorption and a tunable bandgap, which are the most important aspects of ZnO for studying its properties. ZnO has six well-known defects such as zinc and oxygen vacancies (V_0 and V_{zn}), interstitials (O_i and Z_{ni}), and antisites (Z_{no} and O_{zn}). The emission band could be caused by excitonic recombination and due to the above-defined defect states. Fig.4.16 shows the fluorescence of ZnO sintered at 400^{o}C and excited by 310nm. [59].

d) Iron Oxide (Fe_3O_4)

As indicated in Fig 4.16, the fluorescence Spectra of Fe_3O_4 was seen at wavelengths ranging from 300 to 700 nm excited by 310nm. The emission peaks in the visible area of the spectral range (300-700) nm, are the graphs from which we analyzed the defect states and emission properties. Essentially, fluorescence provided insight into surface defects such as oxygen vacancy, surface state, and the separation of photoinduced carriers, as well as the recombination of semiconductor material. The broad emission bands are visible in the 400-700nm spectral region due to intra-band gap defects such as oxygen vacancy [60-62].

e) Magnesium Oxide (MgO)

The Fluorescence spectrum of MgO sintered at 400^{o}C shown in Fig. 4.16 was acquired by stimulating the sample by 310 nm. MgO consists of one dominating peak at nm which was due to the band edge emission. Only one peak was observed in the UV region confirming the formation of defective free MgO [63].

4.2.7 Colorimetry

The colorimetry is the quantitated analysis of material for the visible light emission. This is based on color rendering index (CRI), Chromaticity Coordinates (CIE) and Color Correlated Temperature (CCT) coordinates. These color rendering indexes (CRI), Chromaticity Coordinates (CIE), and Color Correlated Temperature (CCT) coordinates are calculated for all the metal oxides prepared from banana peels and tabulated in Table 4.5, emitted in the visible region with "daylight" characteristics, which indicates the material's usefulness in the creation of white light sources [64-66]. The chromaticity color coordinates of x = 0.33 and y = 0.33, with a correlated color temperature (CCT) ranging from 5000 to 5500 K, are nearly identical to those of an ideal white light source, which has x = 0.33, y = 0.33, and a CCT of 5000 K [67]. Table 4.5 presents the CRI, CCT, and CIE 1931 coordinates of the metal oxides, which were obtained from the fluorescence data [69-71]. The calculated CIE coordinates, CCT, and CRI values are very close to those of natural daylight, suggesting that the prepared metal oxides have significant potential as daylighting materials, as shown in Fig. 4.17.

Table 4.6. Detailed colorimetry coordinates of metal oxides calculated from Fluorescence spectra obtained with 310 nm excitation.

Metal Oxides NPs	**CIE (X, Y) coordinates**	**CCT(K)**	**CRI**
CuO	0.57,0.31	1167	50
NiO	0.33,0.33	5487	97
ZnO	0.31,0.33	6273	99
Fe_3O_4	0.33,0.34	5987	99

MgO	0.32,0.33	5570	99

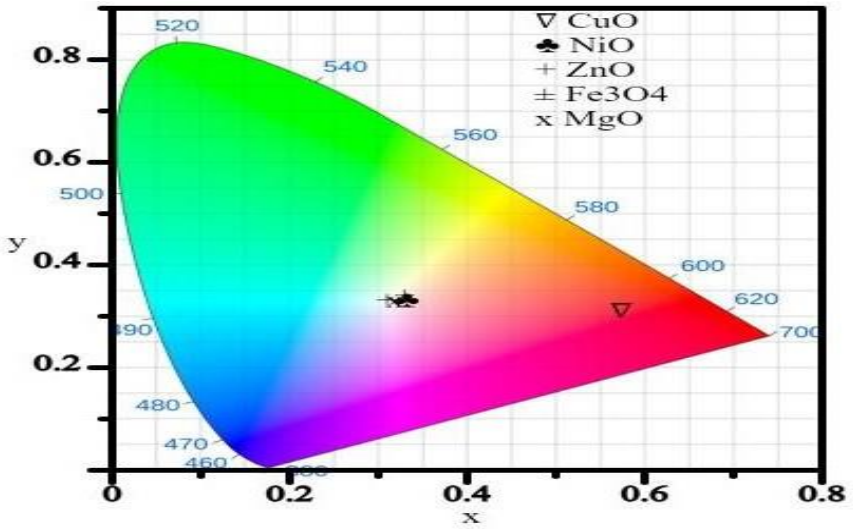

Fig. 4.17 CIE coordinates of the metal oxides NiO, ZnO, Fe_3O_4, CuO and MgO annealed at 400^0C.

4.2.8 Quantum yield in fluorescence

Quantum yield is the percentage of photons absorbed that result in fluorescence emission. From the definition of IUPAC, integral quantum yield is denoted by φ(λ) and is calculated from the formula as stated in equation 4.3 [72-74]. The calculated quantum yield of the prepared metal oxides is shown in the bar graph as shown in Fig 4.9.

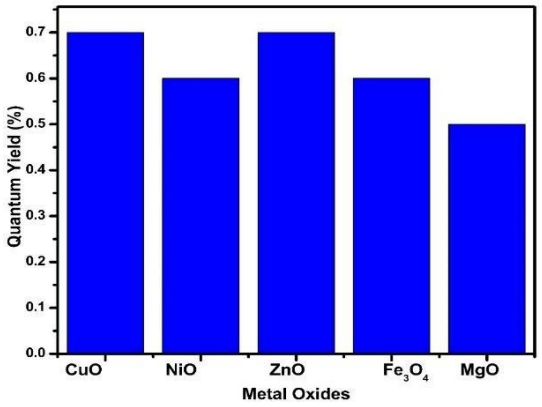

Fig. 4.18. Schematic representation of the calculated quantum yield for metal oxides synthesized from potato peels.

Conclusion

In this chapter, we successfully synthesized metal oxides (MOs) such as MgO, NiO, ZnO, CuO, NiO, ZnO and Fe_3O_4 from potato and banana peels. The structural and optical properties of the synthesized materials were thoroughly examined for both types of peels. The summary of the results is as follows:

1. X-ray diffraction (XRD) analysis confirmed the successful synthesis of these metal oxides, and the phases obtained are well compared with the literature. The average crystallite sizes confirmed the formation of nanomaterial.
2. The yield of MOs(g) was found to be higher with banana peels than those derived from potato peels.
3. Absorption spectra fall in the UV region for all the metal oxides due to defect center formation and no absorption peak was observed in the blue region.
4. The fluorescence spectra excited by UV light showed that the MOs from banana peels had higher quantum yield as compared to potato peels, suggesting enhanced optical properties of MOs.
5. The fluorescence results conclude that banana peel-derived MOs provide a better overall yield than potato peels. Also, all the metal oxides showed good emission in visible light when excited by UV light.

References:

1. O. Diachenko, J. Kováč, O. Dobrozhan, P. Novák, J. Kováč, J. Skriniarova, and A. Opanasyuk, "Structural and optical properties of CUO thin films synthesized using spray pyrolysis method," Coatings **11**(11), 1392 (2021).
2. S. Dagher, Y. Haik, A.I. Ayesh, and N. Tit, "Synthesis and optical properties of colloidal CuO nanoparticles," Journal of Luminescence **151**, 149–154 (2014).
3. D.O.B. Apriandanu, and Y. Yulizar, "Tinospora crispa leaves extract for the simple preparation method of CuO nanoparticles and its characterization," Nano-Structures & Nano-Objects **20**, 100401 (2019).
4. R.M. Mohamed, F.A. Harraz, and A. Shawky, "CuO nanobelts synthesized by a template-free hydrothermal approach with optical and magnetic characteristics," Ceramics International **40**(1), 2127–2133 (2013).
5. R. Balakarthikeyan, A. Santhanam, R. Anandhi, S. Vinoth, A.M. Al-Baradi, Z.A. Alrowaili, Al-Buriahi, and K.D.A. Kumar, "Fabrication of nanostructured NiO and NiO:Cu thin films for high-performance ultraviolet photodetector," Optical Materials **120**, 111387 (2021).
6. A. Rahdar, M. Aliahmad, and Y. Azizi, "NIO nanoparticles: synthesis and characterization," DOAJ (DOAJ: Directory of Open Access Journals), (2015).
7. P. Kaur, S. Rani, and B. Lal, "Excitation dependent photoluminescence properties of ZnO nanophosphor," Optik **192**, 162929 (2019).
8. S. Rani, B. Lal, S. Saxena, and S. Shukla, "Photoluminescence properties of Gd:ZnO nano phosphor," Journal of Sol-Gel Science and Technology **81**(2), 586–592 (2016).
9. M.S. Afzal, and J. Kaur, "Influence on the Optical properties of Green and Chemically Synthesized ZnO," Journal of Physics Conference Series **2267**(1), 012041 (2022).
10. S.T. Fardood, A. Ramazani, and S.W. Joo, "Eco-friendly Synthesis of Magnesium Oxide Nanoparticles using Arabic Gum," Journal of Applied Chemical Research. **12**(1), 8–15 (2018).
11. K. He, F.-X. Ma, C.-Y. Xu, and J. Cumings, "Mapping magnetic fields of Fe3O4 nanosphere assemblies by electron holography," Journal of Applied Physics

113(17), (2013).

12. M.T. Naznin, M. Lefsrud, V. Gravel, and X. Hao, “Using different ratios of red and blue LEDs to improve the growth of strawberry plants,” Acta Horticulturae (1134), 125–130 (2016).
13. K.S. Siddiqi, and A. Husen, “Plant response to engineered metal oxide nanoparticles,” Nanoscale Research Letters **12**(1), (2017).
14. A.C. Nwanya, S. Botha, F.I. Ezema, and M. Maaza, “Functional metal oxides synthesized using natural extracts from waste maize materials,” Current Research in Green and Sustainable Chemistry **4**, 100054 (2021).
15. S. Fakhari, M. Jamzad, and H.K. Fard, “Green synthesis of zinc oxide nanoparticles: a comparison,” Green Chemistry Letters and Reviews **12**(1), 19–24 (2019).
16. C. Campillo, R. Fortes, and M. Del Henar Prieto, “Solar radiation effect on crop production,” InTech eBooks (2012).
17. S.D. Gupta, *Light Emitting Diodes for Agriculture* (2017).
18. M.M. Helal, T. a. E.- Adawy, A.E.E.- Beltagy, A.A.E.- Bedawey, and S.M. Youssef, “Evaluation of potato peel extract as a source of antioxidant and antimicrobial substances,” Menoufia Journal of Food and Dairy Sciences **5**(6), 79–90 (2020).
19. S.L. Sampaio, S.A. Petropoulos, A. Alexopoulos, S.A. Heleno, C. Santos-Buelga, L. Barros, and I.C.F.R. Ferreira, “Potato peels as sources of functional compounds for the food industry: A review,” Trends in Food Science & Technology **103**, 118–129 (2020).
20. B. Djamila, L.S. Eddine, B. Abderrhmane, A. Nassiba, and A. Barhoum, “In vitro antioxidant activities of copper mixed oxide (CuO/Cu2O) nanoparticles produced from the leaves of Phoenix dactylifera L,” Biomass Conversion and Biorefinery, (2022).
21. R. Goel, R. Jha, M. Bhushan, R. Bhardwaj, and C. Ravikant, “Hydrothermally synthesized nickel oxide (NiO) nano petals,” Materials Today Proceedings **48**, 687–689 (2021).
22. S. Arya, P. Mahajan, S. Mahajan, A. Khosla, R. Datt, V. Gupta, S.-J. Young, and S.K. Oruganti, “Review—Influence of processing parameters to control

morphology and optical properties of Sol-Gel synthesized ZNO nanoparticles," ECS Journal of Solid State Science and Technology **10**(2), 023002 (2021).

23. P. Kaur, and S. Rani, "Defect induced emission of $MgAl_2O_4$ sintered at high temperature," Journal of Physics Conference Series **2267**(1), 012100 (2022).
24. A. Rautela, J. Rani, and M. Debnath, "Green synthesis of silver nanoparticles from Tectona grandis seeds extract: characterization and mechanism of antimicrobial action on different microorganisms," Journal of Analytical Science & Technology **10**(1), (2019).
25. G.T. Freschet, J.H.C. Cornelissen, R.S.P. Van Logtestijn, and R. Aerts, "Evidence of the 'plant economics spectrum' in a subarctic flora," Journal of Ecology **98**(2), 362–373 (2009).
26. P.B. Devaraja, D.N. Avadhani, S.C. Prashantha, H. Nagabhushana, S.C. Sharma, B.M. Nagabhushana, and H.P. Nagaswarupa, "Synthesis, structural and luminescence studies of magnesium oxide nanopowder," Spectrochimica Acta Part a Molecular and Biomolecular Spectroscopy **118**, 847–851 (2013).
27. A. A, Z. H, Z. M, U. Haq I., P. Ar, A. Js, and H. A, "Synthesis, characterization, applications, and challenges of iron oxide nanoparticles," DOAJ (DOAJ: Directory of Open Access Journals), (2016).
28. D. Shi, M.E. Sadat, A.W. Dunn, and D.B. Mast, "Photo-fluorescent and magnetic properties of iron oxide nanoparticles for biomedical applications," Nanoscale **7**(18), 8209–8232 (2015).
29. S. Kuriakose, D.K. Avasthi, and S. Mohapatra, "Effects of swift heavy ion irradiation on structural, optical and photocatalytic properties of ZnO–CuO nanocomposites prepared by carbothermal evaporation method," Nano Online, (2016).
30. Z. Sabouri, A. Akbari, H.A. Hosseini, M. Khatami, and M. Darroudi, "Tragacanth-mediate synthesis of NiO nanosheets for cytotoxicity and photocatalytic degradation of organic dyes," Bioprocess and Biosystems Engineering **43**(7), 1209–1218 (2020).
31. M. Firouzi, M. Giahi, M. Najafi, S.S. Homami, and S.H.H. Mousavi, "Electrochemical determination of amlodipine using a CuO-NiO nanocomposite/ionic liquid modified carbon paste electrode as an electrochemical

sensor," Journal of Nanoparticle Research **23**(4), (2021).

32. S. Arya, P. Mahajan, S. Mahajan, A. Khosla, R. Datt, V. Gupta, S.-J. Young, and S.K. Oruganti, "Review—Influence of processing parameters to control morphology and optical properties of Sol-Gel synthesized ZNO nanoparticles," ECS Journal of Solid State Science and Technology **10**(2), 023002 (2021).
33. P. Kaur, and S. Rani, "Defect induced emission of MgAl2O4 sintered at high temperature," Journal of Physics Conference Series **2267**(1), 012100 (2022).
34. A. Rautela, J. Rani, and M. Debnath, "Green synthesis of silver nanoparticles from Tectona grandis seeds extract: characterization and mechanism of antimicrobial action on different microorganisms," Journal of Analytical Science & Technology **10**(1), (2019).
35. G.T. Freschet, J.H.C. Cornelissen, R.S.P. Van Logtestijn, and R. Aerts, "Evidence of the 'plant economics spectrum' in a subarctic flora," Journal of Ecology **98**(2), 362–373 (2009).
36. E.H.H. Hasabeldaim, "CIE-1931 chromaticity diagram | an online tools," (n.d.).
37. A. Bala, and S. Rani, "UV excited emission spectra of gadolinium aluminium garnet," Journal of Optics **52**(2), 868–874 (2022).
38. R. Zainul, "Determination of the half-life and the quantum yield of ZnO semiconductor photocatalyst in humic acid," Der Pharmacia Lettre **15**(8), 176–179 (2018).
39. J. Mathew, A.S. Raj, D.D. Priya, D. Titus, E.J.J. Samuel, and S.M. Roopan, "Photoluminescence properties of Ag3PO4/CuO nanocomposites: Quantum yield effect," Optik **219**, 165282 (2020).
40. J.B. Birks, "Fluorescence quantum yield measurements," Journal of Research of the National Bureau of Standards Section a Physics and Chemistry **80A**(3), 389 (1976).
41. A. Sharma, G. Sahu, and S.P. Mahapatra, "Synthesis, characterization, and dielectric studies of magnetic iron oxide nanoparticles," Ferroelectrics, **618**(1), 11–24 (2024).
42. S.T. Fardood, A. Ramazani, and S.W. Joo, "Eco-friendly Synthesis of Magnesium Oxide Nanoparticles using Arabic Gum," Journal of Applied Chemical Research. **12**(1), 8–15 (2018).

43. O. Diachenko, J. Kováč, O. Dobrozhan, P. Novák, J. Kováč, J. Skriniarova, and A. Opanasyuk, “Structural and optical properties of CUO thin films synthesized using spray pyrolysis method,” Coatings **11**(11), 1392 (2021).
44. S. Dagher, Y. Haik, A.I. Ayesh, and N. Tit, “Synthesis and optical properties of colloidal CuO nanoparticles,” Journal of Luminescence **151**, 149–154 (2014).
45. G.T. Anand, R. Nithiyavathi, R. Ramesh, S.J. Sundaram, and K. Kaviyarasu, “Structural and optical properties of nickel oxide nanoparticles: Investigation of antimicrobial applications,” Surfaces and Interfaces **18**, 100460 (2020).
46. A. Vanaja, and K.S. Rao, “Effect of co doping on structural and optical properties of zinc oxide nanoparticles synthesized by Sol-Gel Method,” Advances in Nanoparticles **05**(01), 83–89 (2016).
47. P. Kaur, S. Rani, B. Lal, and A.M. Nelson, “Role of defect states in the luminescence properties of ZnO,” AIP Conference Proceedings **2136**, 040015 (2019).
48. K. He, F.-X. Ma, C.-Y. Xu, and J. Cumings, “Mapping magnetic fields of Fe3O4 nanosphere assemblies by electron holography,” Journal of Applied Physics **113**(17), (2013).
49. S. Thomas, D. Sakthikumar, Y. Yoshida, and M.R. Anantharaman, “Spectroscopic and photoluminescence studies on optically transparent magnetic nanocomposites based on sol–gel glass: Fe3O4,” Journal of Nanoparticle Research **10**(1), 203–206 (2007).
50. P.B. Devaraja, D.N. Avadhani, S.C. Prashantha, H. Nagabhushana, S.C. Sharma, B.M. Nagabhushana, and H.P. Nagaswarupa, “Synthesis, structural and luminescence studies of magnesium oxide nanopowder,” Spectrochimica Acta Part a Molecular and Biomolecular Spectroscopy **118**, 847–851 (2013).
51. H.R. Naika, K. Lingaraju, K. Manjunath, D. Kumar, G. Nagaraju, D. Suresh, and H. Nagabhushana, “Green synthesis of CuO nanoparticles usingGloriosa superbaL. extract and their antibacterial activity,” Journal of Taibah University for Science **9**(1), 7–12 (2014).
52. G.M. Sulaiman, A.T. Tawfeeq, and M.D. Jaaffer, “Biogenic synthesis of copper oxide nanoparticles using olea europaea leaf extract and evaluation of their toxicity activities: An in vivo and in vitro study,” Biotechnology Progress **34**(1),

218–230 (2017).

53. S.R. Nalage, M.A. Chougule, S. Sen, P.B. Joshi, and V.B. Patil, “Sol–gel synthesis of nickel oxide thin films and their characterization,” Thin Solid Films **520**(15), 4835–4840 (2012).
54. N. Mayedwa, N. Mongwaketsi, S. Khamlich, K. Kaviyarasu, N. Matinise, and M. Maaza, “Green synthesis of nickel oxide, palladium and palladium oxide synthesized via Aspalathus linearis natural extracts: physical properties & mechanism of formation,” Applied Surface Science **446**, 266–272 (2017).
55. F.T. Thema, E. Manikandan, A. Gurib-Fakim, and M. Maaza, “Single phase Bunsenite NiO nanoparticles green synthesis by Agathosma betulina natural extract,” Journal of Alloys and Compounds **657**, 655–661 (2015).
56. A.A. Ezhilarasi, J.J. Vijaya, K. Kaviyarasu, M. Maaza, A. Ayeshamariam, and L.J. Kennedy, “Green synthesis of NiO nanoparticles using Moringa oleifera extract and their biomedical applications: Cytotoxicity effect of nanoparticles against HT-29 cancer cells,” Journal of Photochemistry and Photobiology B Biology **164**, 352–360 (2016).
57. S. Karthik, P. Siva, K.S. Balu, R. Suriyaprabha, V. Rajendran, and M. Maaza, “Acalypha indica– mediated green synthesis of ZnO nanostructures under differential thermal treatment: Effect on textile coating, hydrophobicity, UV resistance, and antibacterial activity,” Advanced Powder Technology **28**(12), 3184–3194 (2017).
58. J. Hernández-Andrés, R.L. Lee, and J. Romero, “Calculating correlated color temperatures across the entire gamut of daylight and skylight chromaticities,” Applied Optics **38**(27), 5703 (1999).
59. D. Hassan, A.T. Khalil, J. Saleem, A. Diallo, S. Khamlich, Z.K. Shinwari, and M. Maaza, “Biosynthesis of pure hematite phase magnetic iron oxide nanoparticles using floral extracts of Callistemon viminalis (bottlebrush): their physical properties and novel biological applications,” Artificial Cells Nanomedicine and Biotechnology **46**(1), 693–707 (2018).
60. S. Vasantharaj, S. Sathiyavimal, P. Senthilkumar, F. LewisOscar, and A. Pugazhendhi, “Biosynthesis of iron oxide nanoparticles using leaf extract of Ruellia tuberosa: Antimicrobial properties and their applications in photocatalytic

degradation," Journal of Photochemistry and Photobiology B Biology **192**, 74–82 (2018).

61. S. Ananthi, M. Kavitha, E.R. Kumar, A. Balamurugan, Y. Al-Douri, H.K. Alzahrani, A.A. Keshk, T.M. Habeebullah, S.H. Abdel-Hafez, and N.M. El-Metwaly, "Natural tannic acid (green tea) mediated synthesis of ethanol sensor based Fe3O4 nanoparticles: Investigation of structural, morphological, optical properties and colloidal stability for gas sensor application," Sensors and Actuators B Chemical **352**, 131071 (2021).
62. P.B. Devaraja, D.N. Avadhani, S.C. Prashantha, H. Nagabhushana, S.C. Sharma, B.M. Nagabhushana, and H.P. Nagaswarupa, "Synthesis, structural and luminescence studies of magnesium oxide nanopowder," Spectrochimica Acta Part a Molecular and Biomolecular Spectroscopy **118**, 847–851 (2013).
63. C. Shen, T.K. Ng, C. Lee, J.T. Leonard, S. Nakamura, J.S. Speck, S.P. Denbaars, A.Y. Alyamani, M.M. El-Desouki, and B.S. Ooi, "Semipolar InGaN-based superluminescent diodes for solid-state lighting and visible light communications," Proceedings of SPIE, the International Society for Optical Engineering/Proceedings of SPIE **10104**, 101041U (2017).
64. C. Zhao, X. Zhang, and Y. Zheng, "Biosynthesis of polyphenols functionalized ZnO nanoparticles: Characterization and their effect on human pancreatic cancer cell line," Journal of Photochemistry and Photobiology B Biology **183**, 142–146 (2018).
65. P. Kaur, S. Rani, and B. Lal, "Excitation dependent photoluminescence properties of ZnO nanophosphor," Optik **192**, 162929 (2019).
66. S. Thomas, D. Sakthikumar, Y. Yoshida, and M.R. Anantharaman, "Spectroscopic and photoluminescence studies on optically transparent magnetic nanocomposites based on sol–gel glass: Fe3O4," Journal of Nanoparticle Research **10**(1), 203–206 (2007).
67. M. Herlekar, S. Barve, and R. Kumar, "Plant-Mediated green synthesis of iron nanoparticles," Journal of Nanoparticles **2014**, 1–9 (2014).
68. Y. Mou, Z. Yu, Z. Lei, M. Chen, and Y. Peng, "Enhancing opto-thermal performances of white laser lighting by high reflective phosphor converter," Journal of Alloys and Compounds **918**, 165637 (2022).

69. Y. Peng, Z. Yu, J. Zhao, Q. Wang, J. Liu, B. Sun, Y. Mou, and M. Chen, “Unique sandwich design of high-efficiency heat-conducting phosphor-in-glass film for high-quality laser-driven white lighting,” Journal of Advanced Ceramics **11**(12), 1889–1900 (2022).
70. H. Wang, Y. Mou, Y. Peng, Y. Zhang, A. Wang, L. Xu, H. Long, M. Chen, J. Dai, and C. Chen, “Fabrication of phosphor glass film on aluminum plate by using lead-free tellurite glass for laser-driven white lighting,” Journal of Alloys and Compounds **814**, 152321 (2019).
71. H.V. Demir, S. Nizamoglu, T. Erdem, E. Mutlugun, N. Gaponik, and A. Eychmüller, “Quantum dot integrated LEDs using photonic and excitonic color conversion,” Nano Today **6**(6), 632–647 (2011).
72. R. Zainul, “Determination of the half-life and the quantum yield of ZnO semiconductor photocatalyst in humic acid,” Der Pharmacia Lettre **8**(15), 176–179 (2016).
73. J. Mathew, A.S. Raj, D.D. Priya, D. Titus, E.J.J. Samuel, and S.M. Roopan, “Photoluminescence properties of Ag3PO4/CuO nanocomposites: Quantum yield effect,” Optik **219**, 165282 (2020).
74. J.B. Birks, “Fluorescence quantum yield measurements,” Journal of Research of the National Bureau of Standards Section a Physics and Chemistry **80A**(3), 389 (1976).

Chapter 5
METAL OXIDES NANO COMPOSITE FROM GREEN WASTE

5.1 Introduction

In this chapter, we synthesized the nanocomposite of the metal oxides and tuned the optical band gap for grow light applications. The optical band gap of a material determines its ability to absorb and emit light at specific wavelengths, making it an essential factor in the design of effective phosphors for plant growth. The optical band gap edge refers to the energy threshold at which a material begins to absorb photons and subsequently generate electron-hole pairs. This energy level is essential in defining the wavelengths of light that the material can effectively utilize for various applications, including grow lights. The ability to tune the optical band gap for the light emission must lie in the blue (400–500 nm) and red (600–700 nm) regions of the spectrum, which are crucial for photosynthesis. Metal oxides with appropriate band gaps can efficiently emit light in these ranges, enhancing plant growth. We focus on metal oxides, which serve as the host materials for our red and blue phosphors. Our initial investigations include a thorough analysis of the UV absorption characteristics and the optical band gaps of the nanocomposites discussed in section 5.2. This chapter presents the synthesis of various nanocomposites such as MgO/NiO, MgO/CuO, NiO/ZnO, and CuO/ZnO as mentioned in Fig 5.1. Different weight ratios of CuO and ZnO were used such as CuO-20% / ZnO-80%, CuO-40% / ZnO-60%, CuO-60% / ZnO-40%, and CuO-80% / ZnO-20%. For the C20Z80 abbreviation means, 0.2 mol of copper nitrate trihydrate and 0.8 grams of zinc hexahydrate were utilized, as discussed in Chapter 3 (Table 3.4). In addition, nanocomposites of MgO/NiO, MgO/CuO, and NiO/ZnO were also synthesized using appropriate metal salt ratios. By varying the composition and synthesis conditions, we aim to achieve specific band gap values that enhance light emission as required for the PAR region. This tuning process not only improves the performance of the phosphor but also ensures that the grow lights operate effectively under varying environmental conditions. In Fig 5.1, we presented an overview of the various nanocomposites examined throughout this chapter, focusing on their potential applications in grow light technologies. Among the materials studied, CuO/ZnO emerged as the most promising

host due to its advantage in UV absorption and the band gap was also suitable for grow light properties. The decision to proceed with CuO/ZnO was based on its superior performance compared to other nanocomposites we investigated. Its unique combination of optical properties not only meets the specific requirements for grow light applications but also positions it as a viable candidate for further research and optimization.

5.2. To Study the band gap of nanocomposite for an optically stable host composite.

This study investigates the effects of various metal oxide nanocomposites such as MgO/NiO, MgO/CuO, NiO/ZnO, and CuO/ZnO as mentioned in Fig 5.1 to study the grow light properties and their interaction with PAR (Photosynthetically Active Radiation) spectra. The goal is to identify stable host material that optimally enhances plant growth through improved nutrient availability and light absorption. The specific ratios of metal oxides in the nanocomposite can significantly influence UV absorption efficiency. Optimizing the composition is essential to maximize the protective effects. The size of nanoparticles influences their surface area and reactivity. Smaller particles generally have better UV absorption due to increased surface area and quantum effects. Understanding UV absorption is crucial when studying grow light spectra, especially in the context of optimizing conditions for plant growth. This section of the thesis explores the significance of the UV absorption study of all the mentioned nanocomposites to study band gaps and find out the stable host for the grow light [1-2]**.**

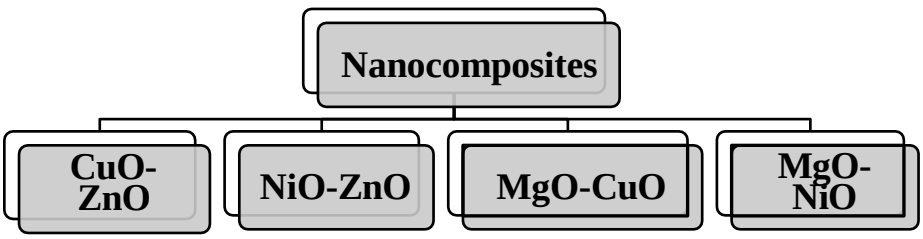

Fig 5.1. Nanocomposite prepared using banana peels

5.2.1. UV Absorption of nanocomposite MgO/CuO

The UV absorption spectra provide crucial vision into the absorption characteristics and the absorption edge, an important parameter for understanding semiconductor behaviour. The spectra for pure MgO, CuO and MgO/CuO composites sintered at 400°C are shown in Fig 5.2(a). The optical band gap and absorption edge were analysed using UV spectroscopy, with results displayed in Fig 5.2(b). The optical band gap (Eg) was determined using the Tauc relation (equation 3.2), and the values for pure MgO, CuO, and MgO/CuO nanocomposites are summarized in Table 5.1. The decrease in Eg with increasing Mg concentration in the MgO/CuO samples indicates a synergistic effect, shifting from the CuO band gap toward that of MgO. As crystallite size reduces to the nanoscale which is because of the quantum confinement can modify the band gap and related optical properties [3-4].

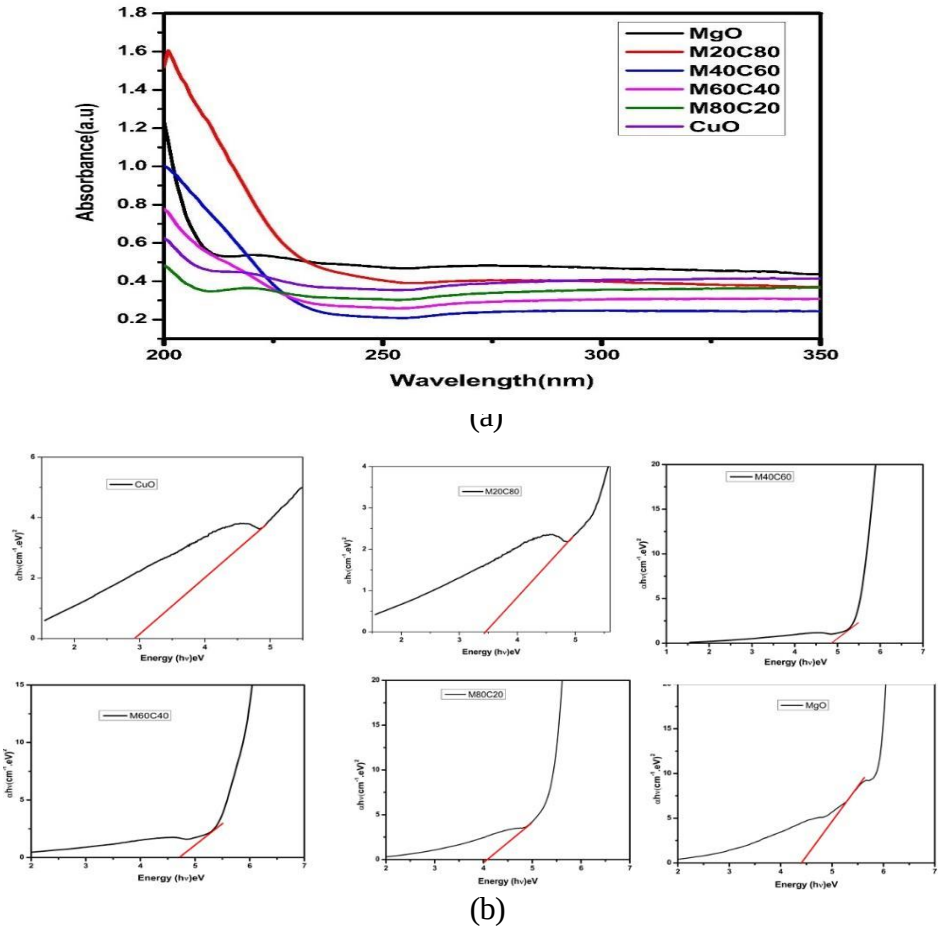

Fig 5.2.(a) UV absorption (b) Tauc plot of CuO, MgO and the MgO /CuO nanocomposite sintered at 400 ^{0}C.

Table 5.1. Calculated Optical band gaps of the metal oxide and nanocomposite of MgO/CuO from the UV absorption data.

S.no	Sample	Band Gap (eV)
1	CuO	3.0
2	M_{20} C_{80}	3.5
3	$M_{40}C_{60}$	4.7
4	$M_{60}C_{40}$	4.9
5	$M_{80}C_{20}$	4.1
6	MgO	4.5

5.2.2. UV Absorption of nanocomposite NiO/ZnO

The UV absorption spectra for pure ZnO, NiO and NiO/ZnO composites sintered at 400°C are presented in Fig 5.3(a). The analysis of the optical band gap and absorption edge was conducted using UV-Vis's spectroscopy, with the findings illustrated in Fig 5.3(b). In NiO/ZnO nanocomposites, UV absorption studies show that the band gap decreases as NiO concentration increases. At lower concentrations, the band gap is similar to pure ZnO, but higher NiO levels introduce new energy states and quantum confinement effects, leading to a red shift in the absorption spectrum. This shift indicates a reduced band gap, influenced by the interaction between NiO and ZnO, making these composites suitable for optoelectronic applications.[5]

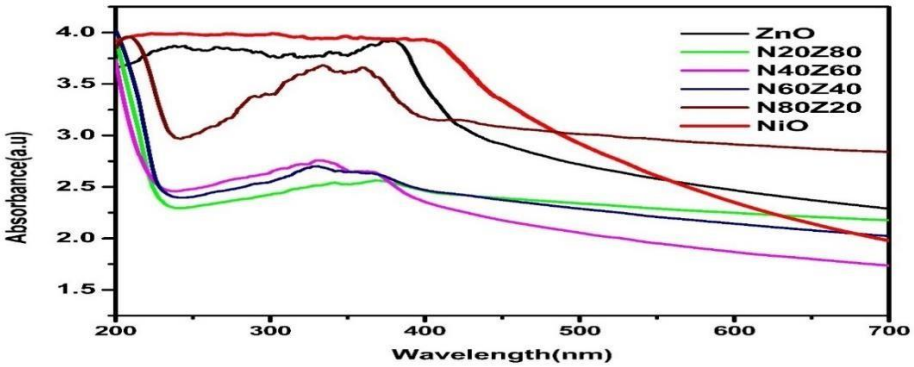

(a)

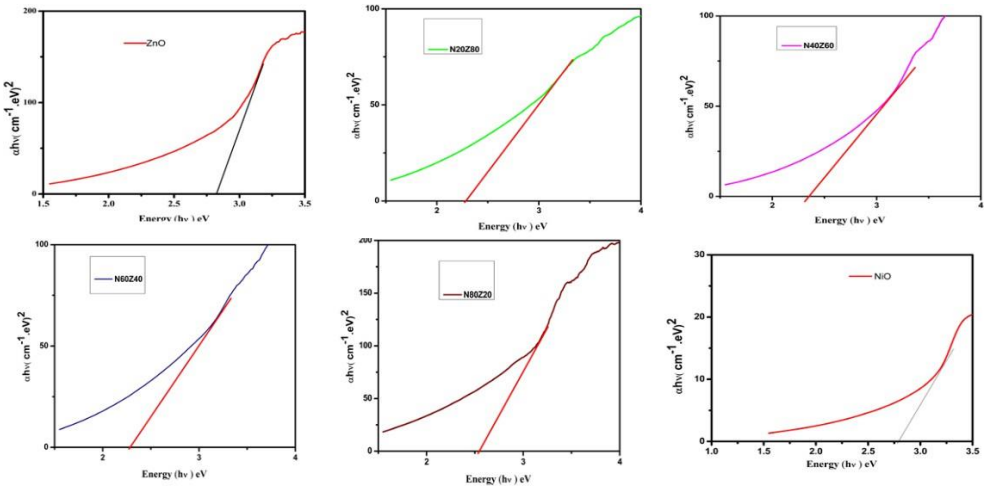

(b)

Fig 5.3. (a)UV absorption (b) Tauc plot of ZnO, NiO and the ZnO/NiO nanocomposite sintered at 400 ^{0}C

Table 5.2. Calculated Optical band gaps of the metal oxide and nanocomposite of NiO/ZnO from the UV absorption data.

S.no	Samples	Band Gap (eV)
1	ZnO	2.8
2	$N_{20}Z_{80}$	2.2
3	$N_{40}Z_{60}$	2.2
4	$N_{60}Z_{40}$	2.1
5	$N_{80}Z_{20}$	2.6
6	NiO	2.5

5.2.3. UV Absorption Of nanocomposite MgO/NiO

As the concentration of NiO increases in MgO nanocomposites, the effective band gap shifts towards that of NiO. The introduction of NiO creates new energy states within the MgO band gap, facilitating electron transitions and reducing the overall band gap. In nanoscale materials, smaller particle sizes and higher NiO concentrations enhance quantum confinement effects, leading to shifts in energy levels and a

decrease in band gap. The interaction between MgO and NiO may result in the hybridization of their electronic states, further aligning the band gap with that of NiO. UV absorption spectroscopy confirms the red shift in the absorption edge, indicating a reduction of the band gap as NiO concentration increases. The band gap of nanocomposites generally decreases with increasing the concentration of NiO in MgO due to the introduction of additional energy levels and quantum confinement effects. In MgO nanocomposites, doping or reducing grain size can slightly decrease the band gap due to quantum confinement and the introduction of defect states, potentially enhancing UV absorption but generally keeping it within the range of wide-bandgap materials [6-8].

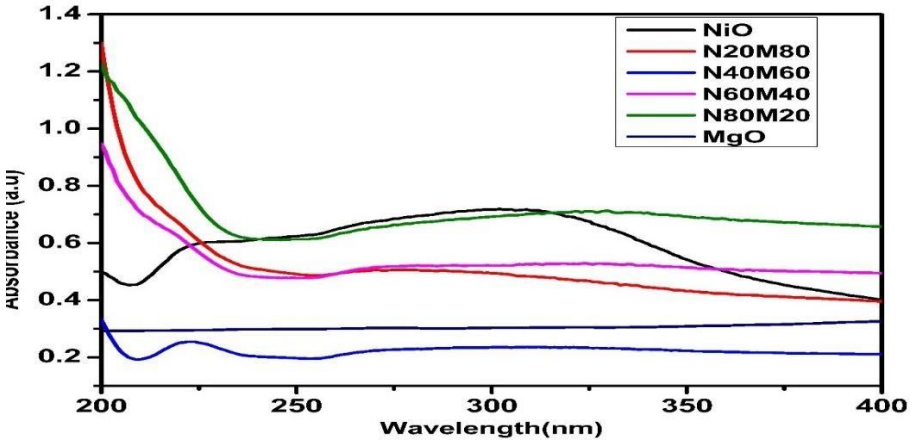

(a)

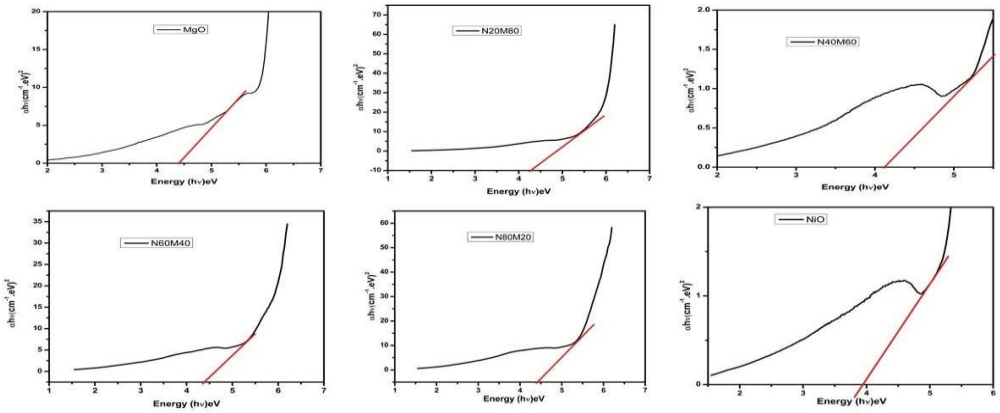

(b)

Fig 5.4. (a) UV absorption (b) Tauc plot of NiO, MgO and the NiO/MgO nanocomposite sintered at 400^0C.

Table 5.3. Calculated Optical band gaps of the metal oxide and nanocomposite of MgO/NiO from the UV absorption data.

S.no	Samples	Band Gap (eV)
1	MgO	4.4
2	$N_{20}M_{80}$	4.3
3	$N_{40}M_{60}$	4.2
4	$N_{60}M_{40}$	4.4
5	$N_{80}M_{20}$	4.5
6	NiO	3.10

5.2.4 UV-Vis Absorption Of nanocomposite CuO/ ZnO

The UV absorption spectra offer significant information about the change in absorption, which is an essential parameter. The optical band gap and the absorption edge of a semiconductor are examined using UV spectroscopy shown in Fig 5.5(b) calculated by using the tauc relation given in equation 3.2. The calculated optical band gap of pure ZnO, CuO and nanocomposites of CuO/ZnO are listed in Table 5.4. The optical band gap results of Eg for all Cu^{2+} concentrations employed in this work show that increasing the atom% of Cu in the CuO/ZnO samples causes Eg to decrease from the values of the ZnO band gap to that of the band gap of CuO. [9-10]. The energy levels of the electrons in a material may become quantized as its crystallite size shrinks to the nanoscale, changing the bandgap and the material's subsequent optical and electrical characteristics. This represents one way in which the crystallite size and bandgap of a material can influence one another. The material’s bandgap and crystallite size are frequently correlated. Because of quantum confinement effects, a material's bandgap can be affected by the size of its crystallites.

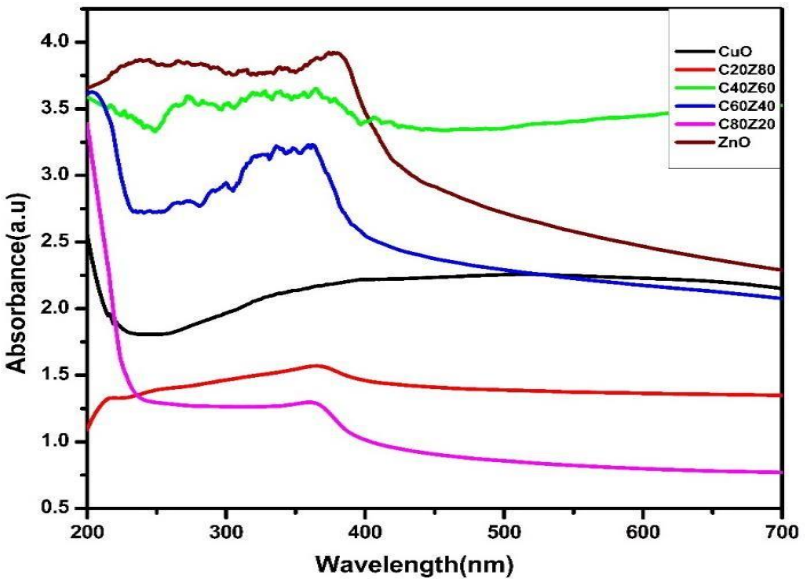

(a)

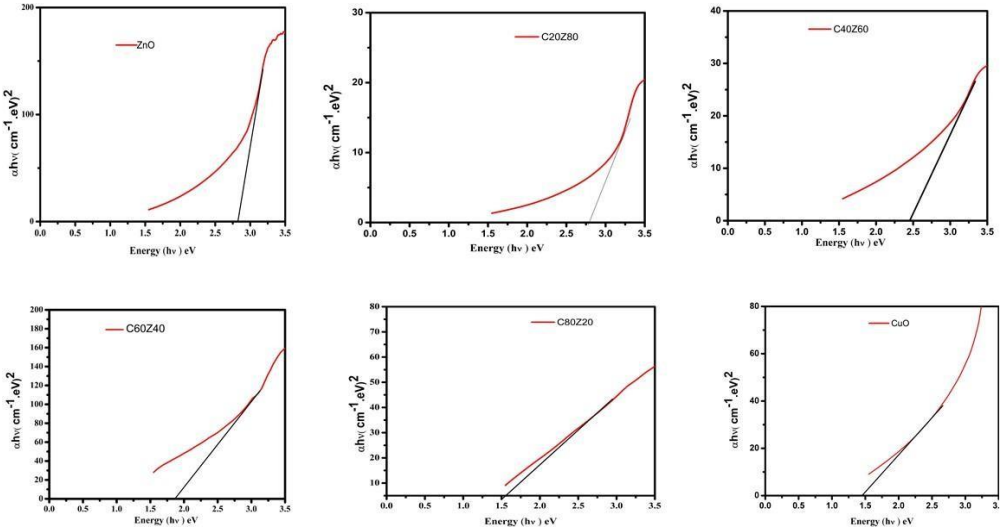

(b)

Fig 5.5. (a)UV absorption (b) Tauc plot of CuO, ZnO and the CuO/ZnO nanocomposite sintered at 400 ^{0}C.

Table 5.4. Calculated Optical band gaps of the metal oxide and nanocomposite of CuO/ZnO from the UV absorption data.

S.no	Sample	Band Gap (eV)
1	ZnO	2.83
2	$C_{20}Z_{80}$	2.79
3	$C_{40}Z_{60}$	2.45
4	$C_{60}Z_{40}$	1.88
5	$C_{80}Z_{20}$	1.55
6	CuO	1.43

The optimal optical band gap for plant growth applications typically corresponds to the wavelengths in the photosynthetically active radiation (PAR) spectrum, which ranges from approximately 400 nm to 700 nm. This range includes two critical regions: Blue Light (400–500 nm) this part of the spectrum is essential for chlorophyll a and b, promoting vegetative growth and influencing plant morphology. An ideal optical band gap for efficient blue light emission would be around 2.5 to 3.1 eV, corresponding to wavelengths from approximately 400 nm to 500 nm and Red Light (600–700 nm) this region is also crucial for photosynthesis, particularly in stimulating flowering and fruiting. The optimal optical band gap for red light emission typically falls between 1.8 to 2.1 eV, corresponding to wavelengths from about 600 nm to 700 nm. From the above analyses of UV-Vis spectroscopy, the band gap was studied to find out the stable host that effectively spans the UV and blue light spectrum, which are essential for promoting photosynthesis in plants. The combination of CuO and ZnO can create synergistic effects that improve light absorption and conversion efficiency. This is beneficial for maximizing the amount of usable light for photosynthesis. The CuO/ZnO nanocomposite's band gap is particularly suited for the growth spectra of plants due to its ability to emit light in both UV and blue regions, which are crucial for photosynthesis. In contrast, the MgO/NiO and MgO/CuO, NiO/ZnO composites do not effectively cover these wavelengths, limiting their applicability in plant lighting. This understanding emphasizes the importance of selecting the right materials for optimal plant growth applications.

5.3. Synthesis of CuO/ZnO nanocomposite

5.3.1. X-Ray Diffraction

The XRD pattern of the prepared nanocomposite is shown in Fig 5.6. The obtained phase of the nanocomposite is crystalline, and the calculated average crystallize size is mentioned in Table 5.5. The peak position 2θ(hkl) and the intensity I(hkl) are the important parameters which are strongly dependent on the mixing ratio of the sample material.[11] The pure copper oxide was indexed by the JCPDS card no 80-1268[12] having a monoclinic structure and 2θ at 32.42,35.43,38.65, 48.68, 53.37, 58.20, 61.48, 66.03, 67.94 and 72.34 respectively. The XRD pattern of ZnO shows the hexagonal Wurtzite structure which is well matched with the JCPDS card no 00-036-1451[12]. The 2θ peaks of ZnO lie at 31.82, 34.46, 36.27, 47.57, 56.64, 62.88, 66.45, 67.98 and 69.13 respectively. The nanocomposite of CuO/ZnO shows a mixed phase as the weight proportion varies as the structure reaches pure CuO. The presence of CuO causes the ZnO peaks to broaden as the Cu^{2+} concentration rises, and the intensity of the peaks that match with the CuO grows progressively. Similar findings have been reported in earlier studies. CuO/ZnO composite has a high degree of purity and crystallinity, according to XRD investigations. From the analysis, we analyzed the mixed phase of CuO/ZnO.

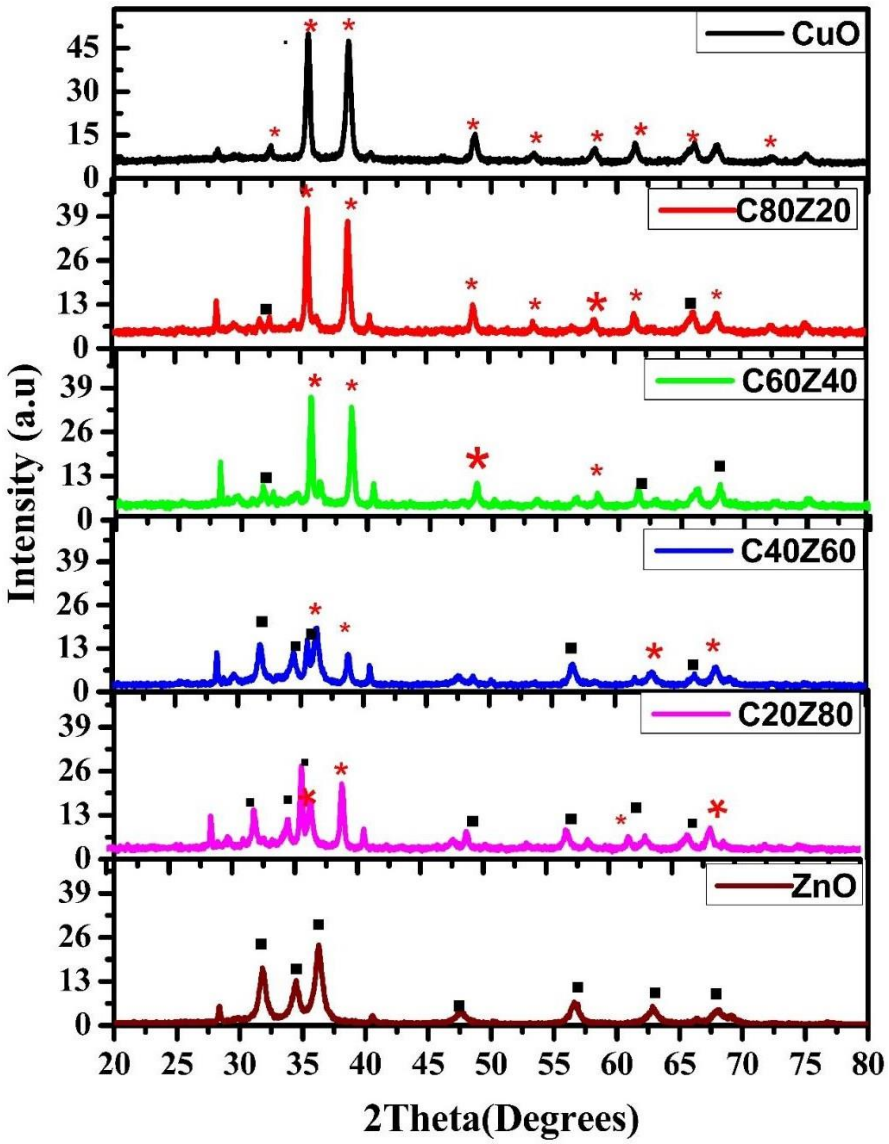

Fig 5.6: XRD spectra of pure ZnO, CuO and nanocomposites of CuO/ZnO annealed at 400^0C.

The Scherer equation is used to calculate the average crystalline size (D) as mentioned above in equation 3.2 of the prepared material and tabulated in Table 5.5.

Table 5.5 Parameters calculated for the nanocomposites prepared from green synthesis such as crystallite size (D), lattice strain of metal oxide ZnO, $C_{20}Z_{80}$, $C_{40}Z_{60}$, $C_{60}Z_{40}$, $C_{80}Z_{20}$, CuO sintered at 400^0C.

S.no	Sample	Structure	D (nm)	Lattice Strain (10^{-3})
1	ZnO	Hexagonal wurtzite	16.89	4.83
2	$C_{20}Z_{80}$	Mixed phase	28.46	2.85
3	$C_{40}Z_{60}$	Mixed phase	34.90	2.78
4	$C_{60}Z_{40}$	Mixed Phase	24.97	4.08
5	$C_{80}Z_{20}$	Mixed Phase	24.10	4.02
6	CuO	Monoclinic	21.62	4.01

5.3.2. FTIR (Fourier Infrared spectroscopy)

The FTIR spectrum of powder samples of CuO, ZnO and CuO/ZnO nanocomposites are used to determine the functional groups of the MOs nanocomposite as shown in Fig 5.7 all the samples were sintered at 400 ^{0}C [16]. Typically, the FTIR spectra of nanocomposite show distinctive absorption bands at particular wave numbers, which correlate to various atomic vibrational modes within the crystal lattice.

These bands positioning in the spectrum and intensity can be used to identify different chemical bonds, such as O–H, Zn–O and Cu–O. The position and shape of absorption bands in the spectrum can reveal details concerning the existence of impurities or defects in the lattice, as well as alteration to the crystal structure during the synthesis process [17-19]. The absorption peaks in 400-600 cm^{-1} are due to the metal-oxygen bonds present in the powder material due to Cu-O and Zn-O stretching vibrations [20]. The peaks lie at 1676, 1455, and 1376 Cm^{-1} are O-H stretching vibration and HOH bending vibration modes of absorbed water molecules, because the high surface area to volume ratio of the nanocrystalline materials causes moisture to be absorbed in the lattice. The C–O stretching of phenol and alcoholic compounds is reflected in the absorption band at 1006 and 1096 cm^{-1} respectively. The presence of residual organic components in ZnO and CuO/ZnO is indicated by peaks located at 2353 cm^{-1}, respectively. Peaks located between 1400 and 1600 cm^{-1} in the samples show that the surface of the resulting nanoparticles contains metal carbonyl groups. Instead, shows a displaced peak at 484 cm^{-1}, which indicates the incorporation of CuO into ZnO

nanoparticles. The stretching vibration of the adsorbed water is attributed to the significant characteristic absorption at 3000-3400cm^{-1}, which indicates the hydroxyl group of the sample material bending. According to research, the stretching frequency is associated with metal oxides and ranges from 430 to 700 cm^{-1} [20]. Consequently, the absorption peak was seen as a ZnO integrated into CuO composite is validated by a prominent band at 2353 cm^{-1} in CuO/ZnO composite.

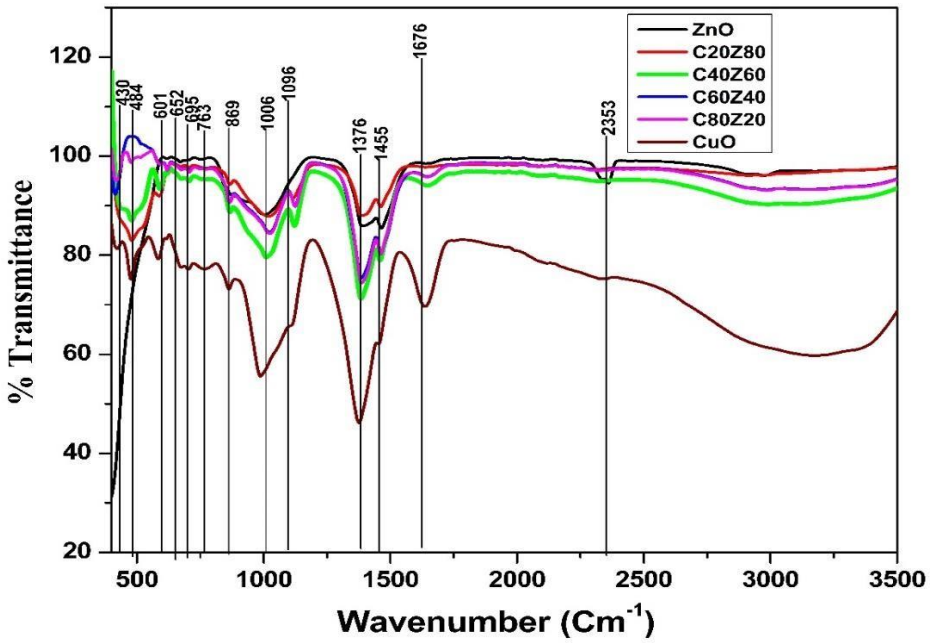

Fig 5.7 Fourier transform infrared spectroscopy pure CuO, ZnO, CuO/ZnO sintered at 400^{0}C prepared from banana peels.

5.3.3 FESEM Study

The average particle size was determined using the particle distribution curve as shown in Fig. 5.8 and the calculated average particle size is 22.89 nm for CuO, 15 nm for ZnO, and 23.28 for the nanocomposite $C_{20}Z_{80}$ which was calculated by ImageJ software and histogram was plotted in the origin software. The morphology of pure CuO, ZnO, and nanocomposite are spherical as shown in Fig 5.8 which shows the comparison of crystallite size calculated from XRD and particle size measured from FESEM. As expected, the average size calculated from the FESEM is slightly larger than the crystallite size confirming that crystals of different crystallite sizes have strong magnetic interaction which forms particles of different sizes. Some particles

are seen to be large which is due to the agglomeration in the particles.[21]. The FESEM results demonstrate that the CuO/ZnO nanocomposite material is constant in shape and size, with agglomeration visible in the images. The distribution of the CuO/ZnO is further analyzed by the EDS mapping images.

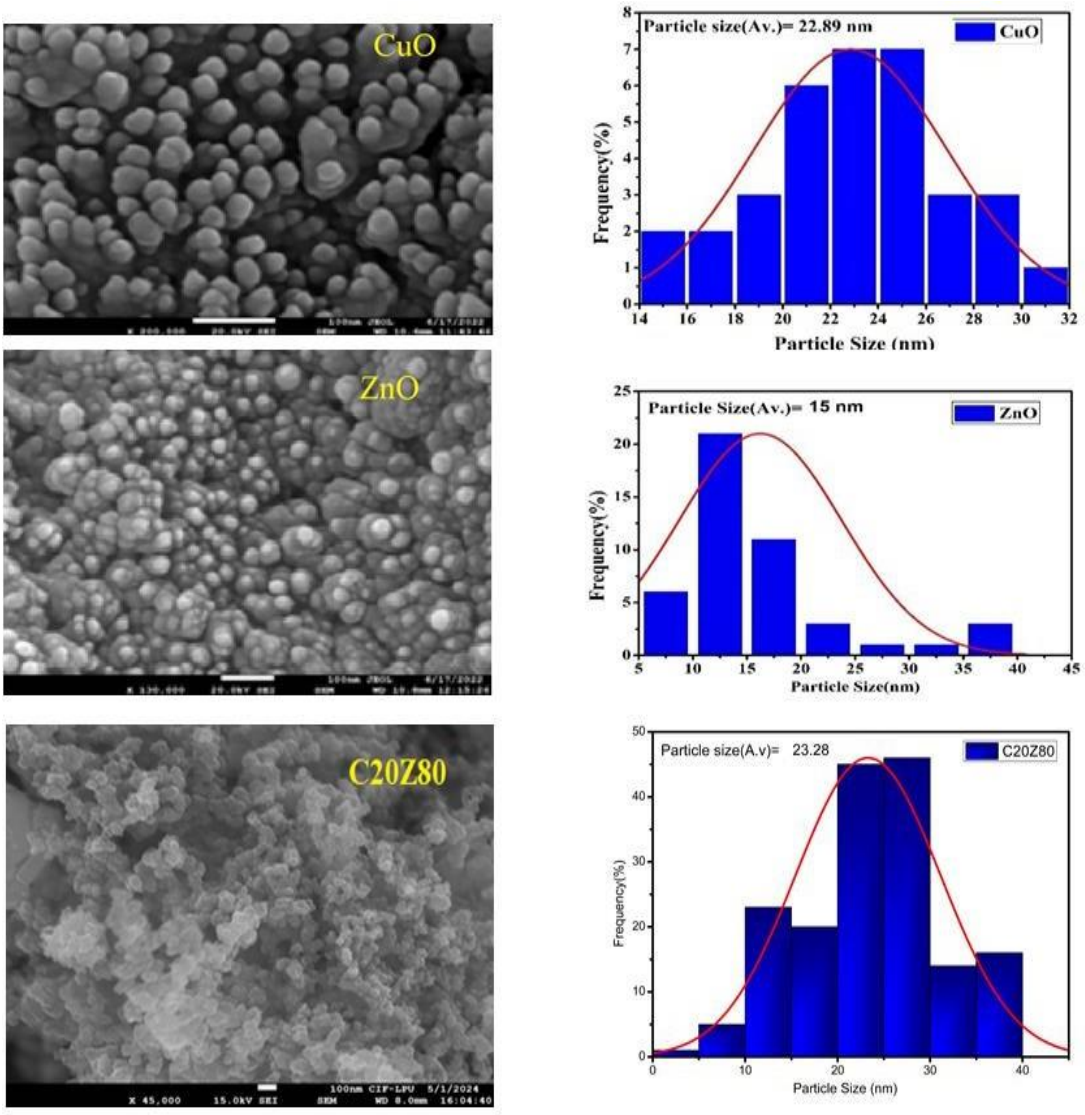

Fig 5.8: FESEM micrographs and bar graphs of particle size of the Pure CuO, ZnO, $C_{20}Z_{80}$ and of powder sample sintered at 400 ^{0}C respectively.

5.3.4. EDX

The elemental composition was determined by using the EDX and this technique is also applicable to minerals, metal alloys, ceramics and metals. This is quantitative compositional information of the nanoparticles. Fig 5.9 shows the EDX spectrum of the ZnO, CuO and the nanocomposite $C_{20}Z_{80}$. The Zn, O and Cu peaks detected in

sample material and the concentration were mentioned in Fig 5.9

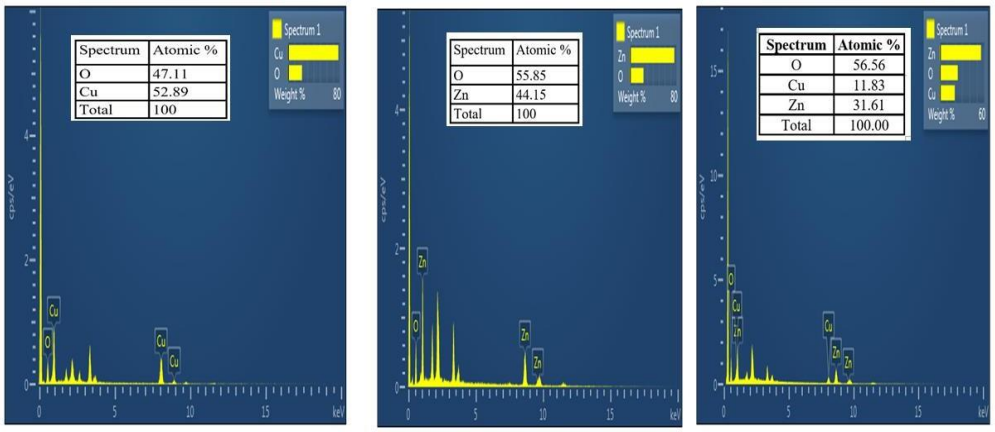

Fig 5.9. EDX spectrum of Pure CuO, ZnO, and C20Z80 of powder sample sintered at 400 ^{0}C respectively.

5.3.5 UV-Vis Absorption

The UV absorption spectra offer significant information about the change in absorption as well as the absorption edge, which is an essential parameter. The optical band gap and the absorption edge of a semiconductor are examined using UV spectroscopy shown in Fig 5.5(b) calculated by using the tauc relation given in equation 3.2. The calculated optical band gap of pure ZnO, CuO and nanocomposites of CuO/ZnO are listed in Table 5.4. The optical band gap results of Eg for all Cu^{2+} concentrations employed in this work show that increasing the atom% of Cu in the CuO/ZnO samples causes Eg to decrease from the values of the ZnO band gap to that of the band gap of CuO. [9-10]. Electron energy levels may become quantized as a material's crystallite size shrinks to the nanoscale, changing the bandgap and the material's subsequent optical and electrical characteristics. This represents one way in which the crystallite size and bandgap of a material can influence one another. The material’s bandgap and crystallite size are frequently correlated. Because of quantum confinement effects, a material's bandgap can be affected by the size of its crystallites.

5.3.6. Fluorescence spectroscopy

- The Fluorescence spectra of the prepared sample material is studied in the range of 200-800 nm excitations by UV light in Fig 5.10. The electronic structure and the dynamics of the material were analyzed by using this technique. It was a very

important technique through which we could differentiate the excitation and emission properties of the composite material from those of the pure samples.

- When the sample material is excited at 310 the emission of the red Shift was observed which is because of the increase in the copper content in the material. As calculated the integrated intensity was observed highest for the $C_{20}Z_{80}$ sample.
- When exited at 210 nm the two emissions are seen which are present at 424 nm and 634 nm which clearly defines the presence of CuO/ZnO in the nanocomposite. UV- blue emission between 400-500 is possible due to the transfer of energy between the surfaces of the nanoparticles. The 424 nm emission is due to the surface impurities and peaks that could have originated from the deep-level defects. The visible bands can be ascribed to certain defects linked to emission arising from oxygen vacancies (Vo), oxygen interstices (Oi), zinc vacancies (VZn), and zinc interstitials (Zni).[24]
- The peak at 634 nm is attributed to orange red emission which is because of the interstitial oxygen defect. In addition, the oxygen vacancies are present in ZnO, CuO and the nanocomposite of ZnO-CuO.
- In both excitations, the intensity of the sample $C_{20}Z_{80}$ was enhanced as compared to the other samples but the peak position was not changed. As the proportion of the CuO increases the intensity decreases. The decrease in the luminous intensity in other sample material was consistent, which was also reported by other researchers. [25-26] which was because of the interface effects. The integrated area of the sample is mentioned below in the tables and Fig 5.11 illustrates the integrated area of CuO/ZnO different concentrations in the range from 300 to 800 nm. The highest intensity of the $C_{20}Z_{80}$ makes a stable host for further study.

As stated in the literature, Photosynthetically Active Radiation (PAR) is the visible light that plants employ to promote photosynthesis and ranges in wavelength from 400 to 700 nm. As our results demonstrated high red and blue emission, the synthesized material has the potential to be further explored. It also showed grow light spectra, which is useful for indoor plantations [27-28]. Table 5.6 shows calculated integrated areas of the prepared samples at 210 nm and 310 nm excitations.

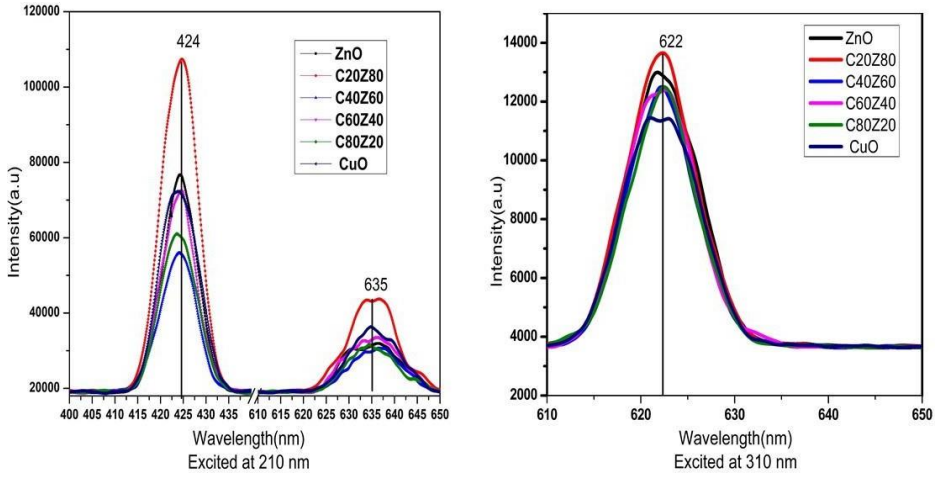

Fig 5.10. Fluorescence Spectra of CuO, ZnO, and nanocomposites of CuO/ZnO metal excited at 210 nm ,310 nm and sintered at 400^0C

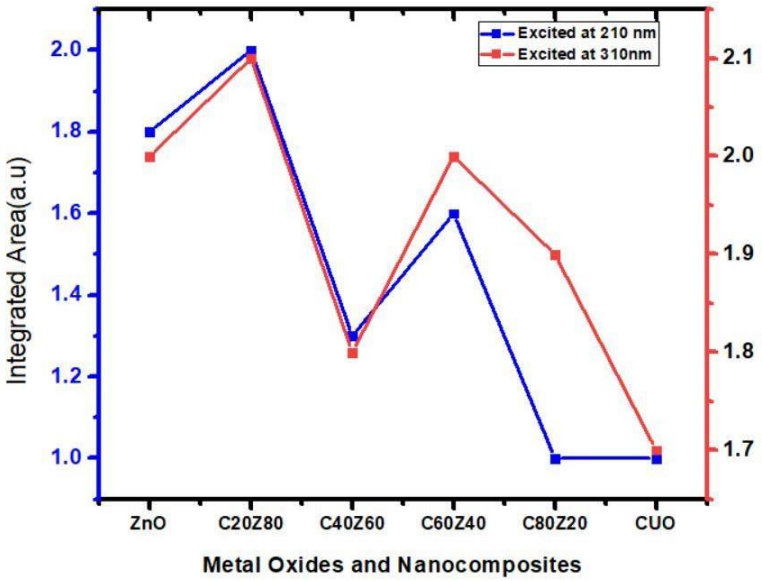

Fig 5.11: Integrated Areas of the CuO, ZnO, and nanocomposites of ZnO-CuO metal oxides excited at 210 nm,310 nm and sintered at 400^0 C.

Table 5.6: Calculated Integrated Areas of the prepared samples at 210 nm and 310 nm excitations.

S.no	Sample	Integrated area excited at 210 nm (10^{-6} A.U.)			Integrated area excited at 310 nm (10^6 A.U.)
		Peak 1		Peak 2	
		Total			
1	ZnO	1.16×10^{-6}	0.73×10^{-6}	1.8×10^{-6}	0.20×10^{-6}
2	$C_{20}Z_{80}$	1.30×10^{-6}	0.71×10^{-6}	2.0×10^{-6}	0.21×10^{-6}
3	$C_{40}Z_{60}$	0.75×10^{-6}	0.54×10^{-6}	1.3×10^{-6}	0.18×10^{-6}
4	$C_{60}Z_{40}$	0.93×110^{-6}	0.66×10^{-6}	1.6×10^{-6}	0.20×10^{-6}
5	$C_{80}Z_{20}$	0.77×10^{-6}	0.24×10^{-6}	1.0×10^{-6}	0.19×10^{-6}
6	CuO	0.83×10^{-6}	0.23×10^{-6}	1.0×10^{-6}	0.17×10^{-6}

5.3.7 Quantum Yield

The percentage of photons absorbed that cause fluorescence emission is essentially known as the quantum yield. According to the IUPAC definition, the integral quantum yield, represented by φ(λ) and calculated by using equation 4.1 and Fig 5.12 represents calculated quantum yield of the pure ZnO, CuO and the nanocomposites.[29]

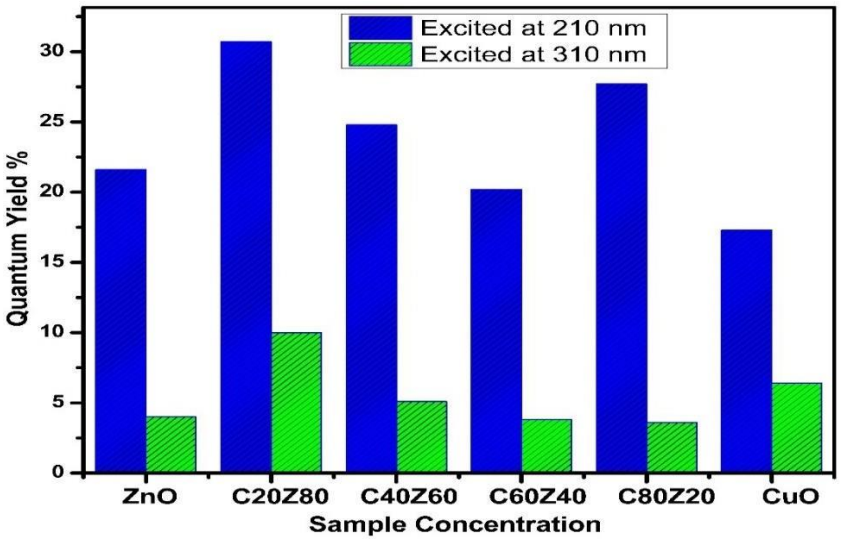

Fig 5.12 Representation of calculated quantum yield of the ZnO, CuO, ZnO/CuO and the nanocomposites.

5.3.8 Decay Analysis

The decay curve for pure ZnO, CuO and the nanocomposites of CuO/ZnO can be expressed as a single exponential function using the equation

$I=A*\exp(-x/t) + B$ .....(5.1)

In this equation, I represent relative intensity, x is decay time, t is fluorescence lifespan, and A and B are constants. Table 5.6 displays the values of lifetime (t) and decay time (x) obtained using exponential fitting. The average duration of a molecule's excited state before emitting a photon is known as its fluorescence lifetime. The molecules emit light at different times called the short-lived period and the long-lived periods. The calculated decay time and the lifetime are tabulated in Table 5.6.[30-31]. The graph shows that the decay time and fluorescence lifetime vary, indicating that $C_{80}Z_{20}$ has a longer lifetime and decay period than other nanophosphors. Fig 5.13 shows fluorescence Decay times obtained for pure ZnO, CuO and nanocomposites of CuO/ZnO sintered at 400^0C.[32-33]

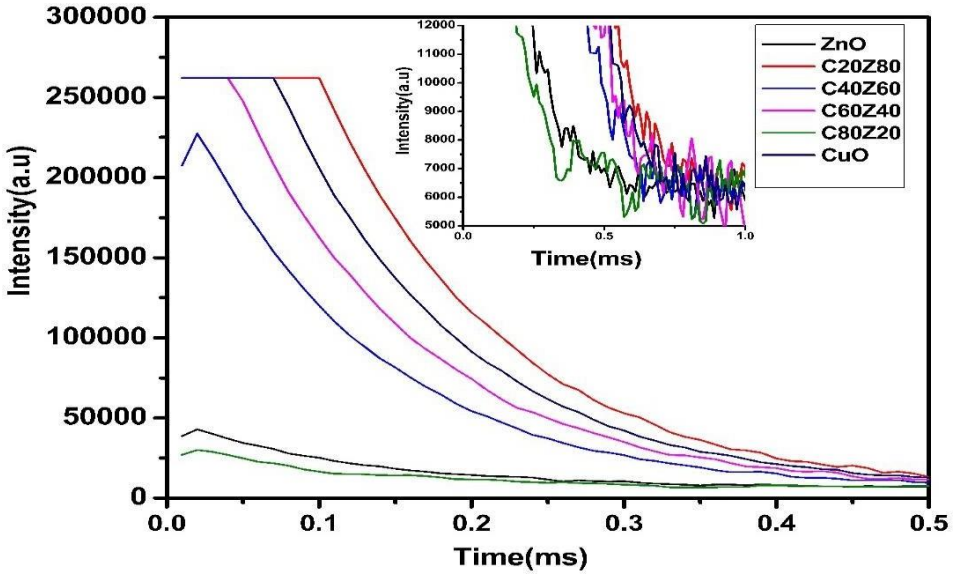

Fig 5.13 Fluorescence Decay times obtained for pure ZnO, CuO and nanocomposites of CuO/ZnO sintered at 400^0C.

5.3.9. Color Space Conversion

In the present research, we focus on determining the chromaticity color coordinates of a phosphorescent material's emission within the visible spectrum, which is crucial for assessing the material's suitability for specific applications and evaluating the colors coordinates for the lighting of plant's growth are determined. [34-36]. The parameters calculated for the metal oxides and the nanocomposite are detailed in Table 5.7. As studied for plant-friendly grow lights, the CIE coordinates typically fall within a range that aligns with the Photosynthetically Active Radiation PAR spectrum (400-700nm) the plants absorb the PAR spectra, especially blue and red radiation. But plants transmit the reflection of most FR radiation which encompasses wavelengths from approximately 400 to 700 nanometers. The exact coordinates can vary depending on the plant species and growth stage but generally aim to replicate natural sunlight as closely as possible [36-37]. When excited at a wavelength of 210 nm, the photonic emission from nanocomposites results in a spectrum that combines both blue and red light. This light combination is advantageous for the fruiting stage of plant development. Conversely, excitation at 310 nm yields light that predominantly falls within the red spectrum (600-700 nm). This specific range of red light is known to

promote vegetative growth and enhance the flowering process. For optimal indoor plant growth, it is recommended to utilize a well-balanced light spectrum that combines both red (600-700 nm) and blue (400-500 nm) wavelengths [38-39]. Using the right light spectrum can significantly influence plant health and productivity, making it crucial for effective indoor gardening. Fig 5.14 shows the CIE coordinates of the pure CuO, ZnO and the nanocomposites excited at 210 nm, and 310 nm respectively. Table 5.6 shows the Calculated CIE coordinates, lifetime, and decay time of the Pure ZnO, CuO and nanocomposites of CuO/ZnO annealed at 400^0C.

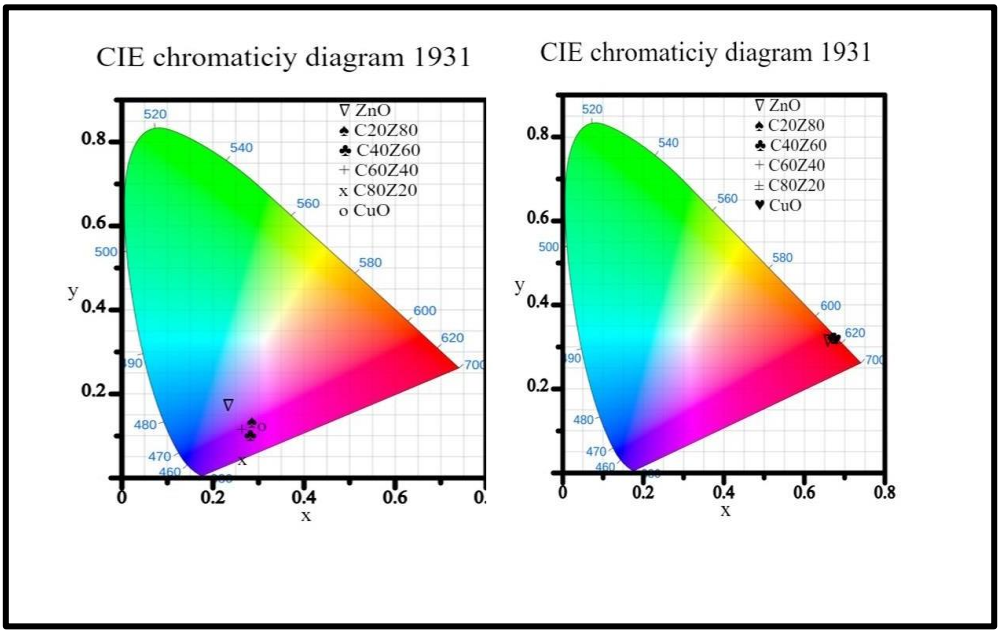

Fig 5.14 CIE coordinates of the pure CuO, ZnO and the nanocomposites of CuO/ZnO excited at 210 and 310 respectively

Table 5.7. Calculated CIE coordinates, lifetime, and decay time of the Pure ZnO, CuO and nanocomposites of CuO/ZnO annealed at 400^0C.

S.No	Sample	CIE (X,Y) coordinates(Excited at 210)	CIE (X,Y) coordinates(Excited at 310)	t (lifetime)	Decay (ms)
1	ZnO	0.23,0.17	0.65,0.31	0.124	0.047
2	$C_{20}Z_{80}$	0.28,0.132	0.66,0.32	0.492	0.101

3	$C_{40}Z_{60}$	0.28,0.11	0.67,0.32	0.635	0.061
4	$C_{60}Z_{40}$	0.26,0.11	0.66,0.32	0.589	0.021
5	$C_{80}Z_{20}$	0.26,0.04	0.67,0.31	0.703	0.824
6	CuO	0.30,0.12	0.67, 0.31	0.503	0.101

Conclusion

MOs nanocomposites MgO/NiO, MgO/CuO, CuO/ZnO and NiO/ZnO were successfully synthesized from banana peels and all the prepared nanocomposites were characterized by UV absorption spectroscopy to understand the tuneability of band gap for grow light spectra.

1. Absorption spectra fall in the UV region for all the nanocomposite of the metal oxides due to defect center formation and no absorption peak was observed in the blue region.
2. From the XRD analysis both the CuO and ZnO peaks which results in the mixed phase that confirms the formation of nanocomposite
3. The morphology of pure CuO, ZnO and nanocomposite are spherical which shows the comparison of crystallite size calculated from XRD and grain size measured from FESEM. As expected the average size calculated from the FESEM is slightly larger than the crystallite size confirming that crystals of different crystallite sizes have strong magnetic interaction which forms particles of different sizes.
4. Upon excitation at 210 nm, the nanocomposite emits light in the near-purple region, while excitation at 310 nm results in red light emission. These emissions align with the expected photoluminescence spectra, confirming the material's suitability for tunable light emission. Notably, the $C_{20}Z_{80}$ composition exhibited the highest fluorescence intensity, indicating its superior optical performance among the various compositions tested. Given that plant growth requires specific light spectra, particularly in the red and blue regions, the CuO/ZnO nanocomposite shows promise in meeting these requirements. The near-purple emission at 210 nm corresponds to the blue light region, while the red emission at 310 nm aligns with the red-light requirement for photosynthesis. This makes the nanocomposite a viable candidate for

PAR (Photosynthetically Active Radiation) light sources, which are crucial for efficient plant growth.

References:

1. N. Rengasamy, R.Y. Othman, H.S. Che, and J.A. Harikrishna, “Beyond the PAR spectra: impact of light quality on the germination, flowering, and metabolite content of Stevia rebaudiana (Bertoni),” Journal of the Science of Food and Agriculture **102**(1), 299–311 (2021).
2. P. Mondal, A. Anweshan, and M.K. Purkait, “Green synthesis and environmental application of iron-based nanomaterials and nanocomposite: A review,” Chemosphere **259**, 127509 (2020).
3. A.L. Laza, M. Jaber, J. Miehé-Brendlé, H. Demais, H.L. Deit, L. Delmotte, and L. Vidal, “Green Nanocomposites: synthesis and characterization,” Journal of Nanoscience and Nanotechnology **7**(9), 3207–3213 (2007).
4. R. Mohammadi-Aloucheh, A. Habibi-Yangjeh, A. Bayrami, S. Latifi-Navid, and A. Asadi, “Green synthesis of ZnO and ZnO/CuO nanocomposites in Mentha longifolia leaf extract: characterization and their application as anti-bacterial agents,” Journal of Materials Science Materials in Electronics **29**(16), 13596–13605 (2018).
5. V. Pavitra, H.P. Divya, B.M. Praveen, G. Nagaraju, and U. Udayabhanu, “Radish (Raphanus sativus) Leaves Mediated CuO-NiO Nanocomposite for Photocatalytic Activity,” Advanced Materials Research **1173**, 47–55 (2022).
6. L. Arun, C. Karthikeyan, D. Philip, and C. Unni, “Optical, magnetic, electrical, and chemo-catalytic properties of bio-synthesized CuO/NiO nanocomposites,” Journal of Physics and Chemistry of Solids **136**, 109155 (2019).
7. V. Pavitra, H.P. Divya, B.M. Praveen, G. Nagaraju, and U. Udayabhanu, “Radish (Raphanus sativus) Leaves Mediated CuO-NiO Nanocomposite for Photocatalytic Activity,” Advanced Materials Research **1173**, 47–55 (2022).
8. L. Arun, C. Karthikeyan, D. Philip, and C. Unni, “Optical, magnetic, electrical, and chemo-catalytic properties of bio-synthesized CuO/NiO nanocomposites,” Journal of Physics and Chemistry of Solids **136**, 109155 (2019).
9. Y. Xu, Y. Ding, L. Zhang, and X. Zhang, “Highly sensitive enzyme-free glucose

sensor based on CuO–NiO nanocomposites by electrospinning," Composites Communications **25**, 100687 (2021).

10. M.A. Khan, N. Nayan, S. Shadiullah, M.K. Ahmad, and C.F. Soon, "Surface Study of CuO Nanopetals by Advanced Nanocharacterization Techniques with Enhanced Optical and Catalytic Properties," Nanomaterials **10**(7), 1298 (2020).
11. N. Goraya, and S. Singh, "Synthesis and Optical Properties of CuO Nanocrystals with Controllable Shapes and Size," MATEC Web of Conferences **57**, 01007 (2016).
12. Ö. Yıldız, A.M. Soydan, E.F. Ipçizade, D. Akın, and Ö. Uçak, "Properties of ZNO nanopowders synthesized by Glycine-Nitrate gel combustion," Acta Physica Polonica A **125**(2), 664–666 (2014).
13. S.A. Akintelu, A.S. Folorunso, F.A. Folorunso, and A.K. Oyebamiji, "Green synthesis of copper oxide nanoparticles for biomedical application and environmental remediation," Heliyon **6**(7), e04508 (2020).
14. M.J. Iqbal, and M.N. Ashiq, "Physical and electrical properties of Zr–Cu substituted strontium hexaferrite nanoparticles synthesized by co-precipitation method," Chemical Engineering Journal **136**(2–3), 383–389 (2007).
15. G. Aurore, B. Parfait, and L. Fahrasmane, "Bananas, raw materials for making processed food products," Trends in Food Science & Technology **20**(2), 78–91 (2008).
16. J.H. Fries, C.N. J, and R.J. Waldron, "Dehydrated banana in the dietetic management of diarrheas of infancy," The Journal of Pediatrics **37**(3), 367–372 (1950)
17. S. Dagher, Y. Haik, A.I. Ayesh, and N. Tit, "Synthesis and optical properties of colloidal CuO nanoparticles," Journal of Luminescence **151**, 149–154 (2014).
18. P. Kaur, S. Rani, B. Lal, and A.M. Nelson, "Role of defect states in the luminescence properties of ZnO," AIP Conference Proceedings **2136**, 040015 (2019).
19. A. Akkaya, B. Şahin, R. Aydın, H. Çetin, and E. Ayyıldız, "Solution-processed nanostructured ZnO/CuO composite films and improvement its physical properties by lustrous transition metal silver doping," Journal of Materials Science Materials in Electronics **31**(17), 14400–14410 (2020).

20. P. Bharathi, S. Karthigeyan, and M.K. Mohan, “Synthesis and functional properties of ZnO/CuO nanocomposite for gas sensing applications,” IOP Conference Series Materials Science and Engineering **1219**(1), 012053 (2022).
21. W. Wang, L. Xu, F. Xian, Z. Yu, H. Qian, R. Zhang, and J. Xu, “Optical properties of CuO/ZnO composites prepared by mechanical grinding,” Optik **224**, 165759 (2020).
22. A. Zainelabdin, S. Zaman, G. Amin, O. Nur, and M. Willander, “Optical and current transport properties of CuO/ZnO nanocoral p–n heterostructure hydrothermally synthesized at low temperature,” Applied Physics A **108**(4), 921–928 (2012).
23. E.D. Sherly, J.J. Vijaya, and L.J. Kennedy, “Visible-light-induced photocatalytic performances of ZnO–CuO nanocomposites for degradation of 2,4-dichlorophenol,” Chinese Journal of Catalysis **36**(8), 1263–1272 (2015).
24. N. Abraham, A. Rufus, C. Unni, and D. Philip, “Dye sensitized solar cells using catalytically active CuO-ZnO nanocomposite synthesized by single step method,” Spectrochimica Acta Part a Molecular and Biomolecular Spectroscopy **200**, 116–126 (2018).
25. A.B. Migdadi, M.K. Alqadi, F.Y. Alzoubi, H.M. Al-Khateeb, and W.T. Bani-Hani, “Photocatalytic activity of prepared ZnO/CuO nanocomposites and kinetic degradation study of methylene blue,” Journal of Materials Science Materials in Electronics **33**(36), 26744–26763 (2022).
26. P. Sable, N. Thabet, J. Yaseen, and G. Dharne, “Effects on structural morphological and optical properties Pure and CuO/ZnO nanocomposite,” Trends in Sciences **19**(24), 3092 (2022).
27. V. Siddiqui, A. Ansari, M. Ansari, Md. Akram, W. Siddiqi, A. Alosaimi, M. Hussein, and M. Rafatullah, “Optimization of facile synthesized ZNO/CUO nanophotocatalyst for organic dye degradation by visible light irradiation using response surface methodology,” Catalysts **11**(12), 1509 (2021).
28. J.W. Hart, “Light and Plant Growth,” Springer Science & Business Media (**1**), (1988).
29. Y. Park, and E.S. Runkle, “Spectral effects of light-emitting diodes on plant growth, visual color quality, and photosynthetic photon efficacy: White versus

blue plus red radiation," PLoS ONE **13**(8), e0202386 (2018).

30. K. Rurack, "Fluorescence Quantum Yields: Methods of Determination and Standards," Springer Series on Fluorescence, 101–145 (2008).
31. S. Das, and V.C. Srivastava, "An overview of the synthesis of CuO-ZnO nanocomposite for environmental and other applications," Nanotechnology Reviews **7**(3), 267–282 (2018).
32. K. Luo, W. Hu, J. Wei, Q. Zhang, Z. Wu, D. Li, F. Miao, Y. Huang, M. Xu, J. Ma, C. Li, G. Chen, R. Han, X. Wang, X. Cui, and P. Ruterana, "Exploration of irradiation intensity dependent external in-band quantum yield for ZnO and CuO/ZnO photocatalysts," Physical Chemistry Chemical Physics **23**(18), 10768–10779 (2021).
33. T. Chang, Z. Li, G. Yun, Y. Jia, and H. Yang, "Enhanced photocatalytic activity of ZNO/CUO nanocomposites synthesized by hydrothermal method," Nano-Micro Letters **5**(3), 163–168 (2013).
34. S. Ouir, H. Lachenani, F. Boudeffar, A. Bouaoua, H. Cheraga, F. Zermane, Z. Benmaamar, and N. Gabouze, "Structural, morphological and optical characterization of CuO/ZnO nanocomposite films," Applied Physics A **129**(1), (2022).
35. T. Smith, and J. Guild, "The C.I.E. colorimetric standards and their use," Transactions of the Optical Society **33**(3), 73–134 (1931).
36. Y. Ohno, "CIE Fundamentals for Color Measurements," International Conference on Digital Printing Technologies, (2000).
37. Nardelli, E. Deuschle, L.D. De Azevedo, J.L.N. Pessoa, and E. Ghisi, "Assessment of Light Emitting Diodes technology for general lighting: A critical review," Renewable and Sustainable Energy Reviews **75**, 368–379 (2016).
38. A. Lavín, R. Sivasamy, E. Mosquera, and M.J. Morel, "High proportion ZnO/CuO nanocomposites: Synthesis, structural and optical properties, and their photocatalytic behavior," Surfaces and Interfaces **17**, 100367 (2019).
39. U.J. Blaszczak, D.A. Aziz, and L. Gryko, "Influence of the spectral composition of LED lighting system on plants cultivation in a darkroom," Proceedings of SPIE, the International Society for Optical Engineering/Proceedings of SPIE **10445**, 104453V (2017).

Chapter 6

DOPED CuO/ZnO NANOCOMPOSITE

6.1 Introduction

Terbium and Cobalt-doped CuO/ZnO nanocomposites for grow light applications are studied in this chapter. The incorporation of terbium and cobalt ions doping into the CuO/ZnO matrix aims to enhance the optical properties and photoluminescence characteristics, which are crucial for effective plant growth. As discussed in Chapter 5, the optical band gap and fluorescence data indicates the maximum integrated area for the C20Z80 nanocomposite. Consequently, we determined that this material is the best-suited host for grow light applications. Doping with terbium/cobalt further enhanced its properties, yielding the most favorable results for our research objectives. By optimizing the doping concentration and analyzing the structural and optical properties of the resulting nanocomposites, we explore their potential to improve light emission efficiency and spectral quality. This study presents an investigation of a novel approach to the sustainable production of Tb CuO/ZnO nanocomposites, for Solid State grow light Spectra. This study investigates the chromatic CIE characteristics of Tb CuO/ZnO for solid-state grow light spectra. This work highlights the potential of green synthesis in the development of advanced materials for grow light applications, paving the way for more environmentally friendly practices. This research focuses on the sustainable synthesis of a terbium (Tb) doped CuO/ZnO nanocomposite, designed for the enhancement of grow light applications. The nanocomposite doped terbium is created by using a green approach, incorporating varying concentrations of terbium (1%, 3%, 5%, and 7%) to optimize its properties. Cobalt-doped CuO/ZnO can be synthesized using the same method as terbium. The structural and optical properties are studied by using Characterization techniques such as X-ray diffraction (XRD), Fourier transforms infrared (FTIR) spectroscopy, UV absorption, and fluorescence spectroscopy and the results of XRD of the nanocomposite reveal a mixed phase of the host material after doping of terbium the structure of the nano powders, indicates that no change in the crystal structure. The synthesized nanocomposite doped terbium exhibits maximum UV absorption at 210 nm which indicates the optimal excitation at this wavelength of both

the terbium and cobalt doped CuO/ZnO nanocomposite. Terbium is often considered the superior dopant compared to cobalt due to its exceptional characteristics that align with the requirements for optimal plant growth. The color rendering index (CRI) of terbium is ideal for promoting photosynthesis, as it emits light in wavelengths that are most beneficial for plants. In contrast, cobalt primarily emits white light, which, while useful in various applications, does not specifically cater to the needs of plant growth. This distinction underscores the importance of selecting the appropriate dopant in the synthesis of materials intended for horticultural applications.

6.1.1. X-Ray Diffraction

The XRD patterns of the samples of the nanocomposite terbium doped 1% Tb,3% Tb,5% Tb, and 7 %Tb are presented in Fig.6.1. In this pattern, the diffraction peaks marked with (x) correspond to CuO, while those marked with (o) correspond to ZnO. From the XRD analysis, we investigated the phase composition and crystallite size of the prepared metal oxides. The peak positions (2θ(hkl)) and intensities (I(hkl)) are crucial parameters that are significantly influenced by the dopant introduced in the sample materials. Pure copper oxide is indexed by JCPDS card no. 80-1268,[1] displaying a monoclinic structure with the following 2θ values: 32.42°, 35.43°, 38.65°, 48.68°, 53.37°, 58.20°, 61.48°, 66.03°, 67.94°, and 72.34°. The XRD pattern of ZnO reveals a hexagonal wurtzite structure, matching well with JCPDS card no. 00-036-1451.[2] The observed 2θ peaks for ZnO are: 31.82°, 34.46°, 36.27°, 47.57°, 56.64°, 62.88°, 66.45°, 67.98°, and 69.13°. X-ray diffraction (XRD) is an effective technique used to analyze peak broadening caused by variations in crystallite size and lattice strain due to dislocations. It is generally presumed that the crystallite shape remains constant across different compositions. Deformation or distortion of the crystal lattice is referred to as lattice strain, which can occur upon doping. As shown in Fig. 6.1, crystallite size is found to be inversely related to lattice strain. This strain can arise in CuO/ZnO due to the existence of impurities or defects introduced during doping.[6]

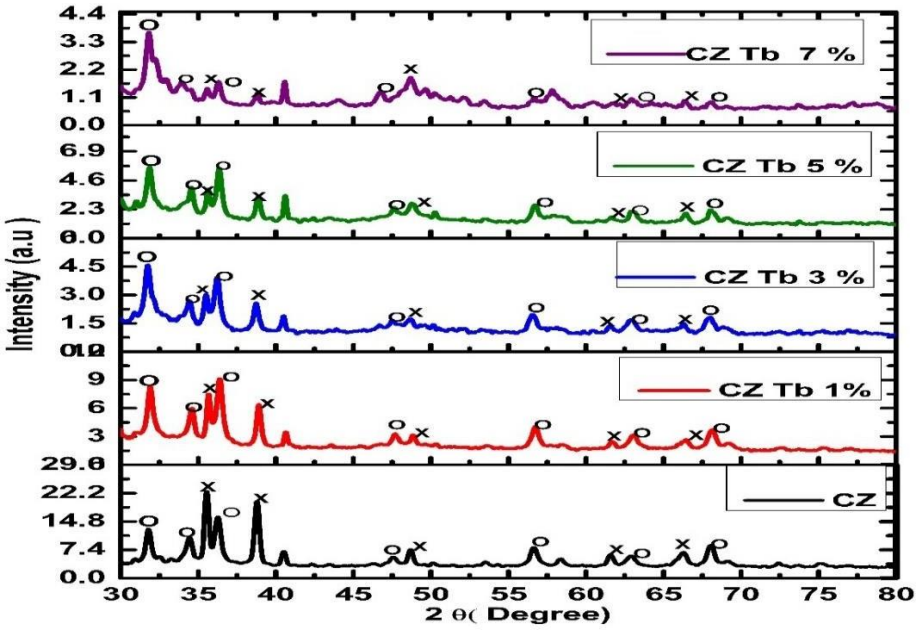

Fig 6.1. XRD spectra of Pure ZnO, CuO and Terbium doped ZnO/CuO nanocomposite annealed at 400^0C.

Overall, the decrease in crystallite size with Tb doping while maintaining the same crystal structure in CuO/ZnO nanocomposites can be attributed to a combination of substitutional effects, enhanced nucleation, kinetic changes, and defect formation. The introduction of Tb can lead to the creation of defects (such as vacancies or interstitials) in the lattice. These defects can inhibit crystal growth by disrupting the orderly arrangement of atoms, preventing larger crystallites from forming while keeping the overall structure consistent.[6] Characterization techniques like X-ray diffraction (XRD) can confirm that the primary structure remains unchanged despite the presence of the dopant.

Table 6.1 Parameters calculated for the nanocomposites prepared from green synthesis such as crystallite size D (nm), Lattice Strain ((× 10^{-6}) of Tb doped CuO/ZnO sintered at 400^0C.

S.No	Sample	Structure	Crystallite Size (D nm)	Lattice Strain (× 10^{-6})

2	CuO/ZnO	Mixed phase	28.46	2.85
3	CuO/ZnO -1 %Tb	Mixed phase	18.31	2.75
4	CuO/ZnO -3%Tb	Mixed Phase	18.20	3.84
5	CuO/ZnO -5%Tb	Mixed Phase	17.23	2.82
6	CuO/ZnO 7%Tb	-- Monoclinic	16.00	2.45

6.1.2 FTIR Spectroscopy

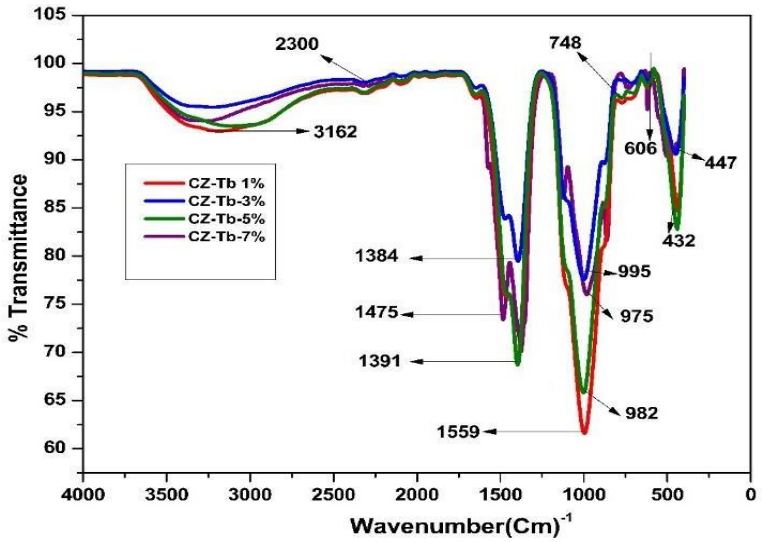

Fig 6.2 FTIR spectra of Tb doped CuO-ZnO nanocomposites prepared from banana peels and sintered at 400 ^{0}C**.**

The FTIR is a useful technique for determining chemical function and intramolecular connections. The typical peaks seen in the FTIR spectra of doped Tb CuO/ZnO samples are shown in Fig 6.2 The absorption peaks at 3162 cm^{-1} are assigned to the regular polymeric O-H stretching vibration of absorbed H_2O in Zn-O and Cu-O lattices from the environment [10]. The peaks at 2300 cm^{-1} and 1559 cm^{-1} are attributed to the anti-symmetric stretching vibration modes C=O caused by the presence of CO_2 molecules in the air. The peaks at 400-450cm^{-1} and 440 cm^{-1} correspond to the stretching vibrations of the oxide groups Zn-O, Cu-O, and doped

(3%, 5%, and 7%) Tb-CuO/ZnO [11], which indicates the hexagonal wurtzite and monoclinic structures, respectively. The CuO/ZnO exhibits peaks at 606, 1559, 1391, 1475, and 2300 cm^{-1}, which are related to the new structure's internal bending and stretching vibrations, including Zn-Tb, Tb-O, Zn-Tb-O, Tb-Zn-O [3]. An increase in peak sharpness indicates that the lattice structure is well-crystallized [12]. The FTIR analyses provide a comprehensive view of the chemical interactions and structural features of the CuO/ZnO doped Tb samples. The presence of specific peaks related to different bonds and vibrations indicates the successful doping and interaction between terbium, zinc, and copper oxides. Fig 6.2 shows FTIR spectra of CuO/ZnO nanocomposites doped terbium 1%,3%,5%, and 7% prepared from banana peels and sintered at 400 ^{0}C.

6.1.3 UV-Vis Absorption

The optical absorption bandgap and the electronic transitions of the prepared material are analyzed by the UV-Vis spectrum [3,4]. This technique is effective for analyzing the impact of doping on the host lattice and coordination location. The Optical absorption versus wavelength (nm) plot of Tb-doped CuO/ ZnO is shown in Fig 6.3 and the broad absorption peaks are seen in 200-250 nm. The optical absorbance of samples steadily decreases when Tb content increases basically with the doping concentration. The band gaps were calculated by using the Tauc relation given in equation(3.4)

The Tb-doped CuO/ZnO nanocomposite band gap energy can be examined as shown in Fig 6.3 (b). Optical bandgap energy decreases with the doping concentration 3.10,3.00,2.78 eV for 1%, 3% and 5% Tb doping respectively. The slight increase in the bandgap observed in 7% doping of Tb could be ascribed to the modest increase in crystal size and micro-strain with this Tb quantity. According to studies, the reduction in the band was ascribed to the exchange of interactions among sp electrons and the d-electron of the dopant, or the presence of mid-band gap states causing a shift in the optical band gap [8-9].

The redshift in the optical absorption edge of Tb-doped CuO/ZnO can be explained by the combined effects of the donor energy levels introduced by Tb^{3+} ions, the narrower bandgap of CuO, and the interactions between the two phases. The donor states created by Tb^{3+}ions lower the bandgap of ZnO, and the presence of CuO

further narrows the overall bandgap, shifting the absorption edge towards longer wavelengths (redshift). This results in enhanced visible light absorption and enhances the composite material more effectively for grow light applications.

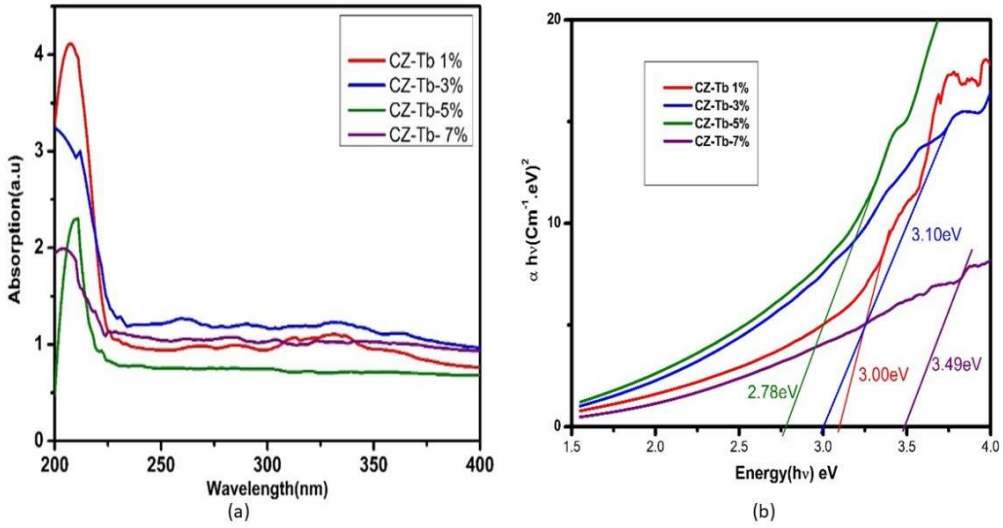

Fig 6.3: Plot of UV absorption spectra of Tb doped CuO/ZnO nanocomposites (b) Tauc plot of the obtained UV spectra prepared from banana peels and sintered at 400 ^{0}C.

6.1.4 Fluorescence spectroscopy

The ZnO-CuO nanocomposite doped with terbium shows an exciting fluorescent property that makes it suitable for the indoor plantation called grow light. The broad band of blue and red emission was observed from 400-440 nm and 600-660 nm at high intensity. The peak was also seen in the range of ~ 460–560 nm centered at 465,475, 488,523,541,554,578 for 1% Tb,3%Tb, 5%Tb and 7%Tb doped CuO/ZnO respectively corresponds to the blue emission. This deep-level emission was linked to the charge carrier relaxation through the surface and was caused by defects at the intrinsic oxygen and zinc vacancies as well as the $^{5}D_{4}$–$^{7}F_{5}$ transition of Tb^{3+} ions due to the Tb incorporation, which resulted in the lattice distortion, which reached an extremum for 5% Tb doping, as the micro-strain analysis showed [13].

Terbium (Tb^{3+}) exhibits sharp green luminescence when excited by UV light, with its strongest emission peak at around **545 nm** due to the $^5D_4 \rightarrow {}^7F_5$ transition. Other weaker emission peaks appear near **490 nm**, **585 nm**, and **620 nm**, corresponding to blue-green, yellow, and orange-red emissions. This makes Tb^{3+} ideal for use in green-emitting phosphors and optical applications. Fig 6.4 demonstrates many peaks in the visible region caused by Tb^{3+} transition lines. Fig 6.5 (a, b) shows emission spectra in the visible area at 210nm, resulting from the broadband emission 5d-4f transition of Tb^{3+} ions [14-15].

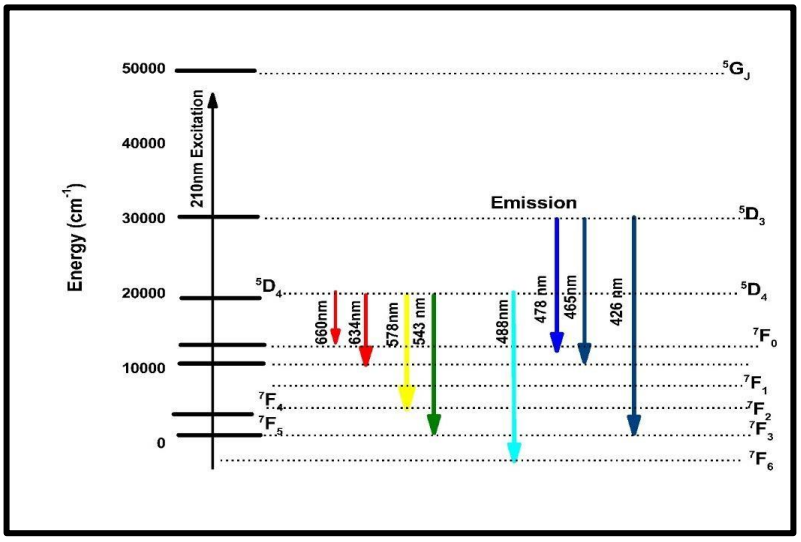

Fig 6.4. Transition lines /Energy level diagram of Terbium Tb^{3+}

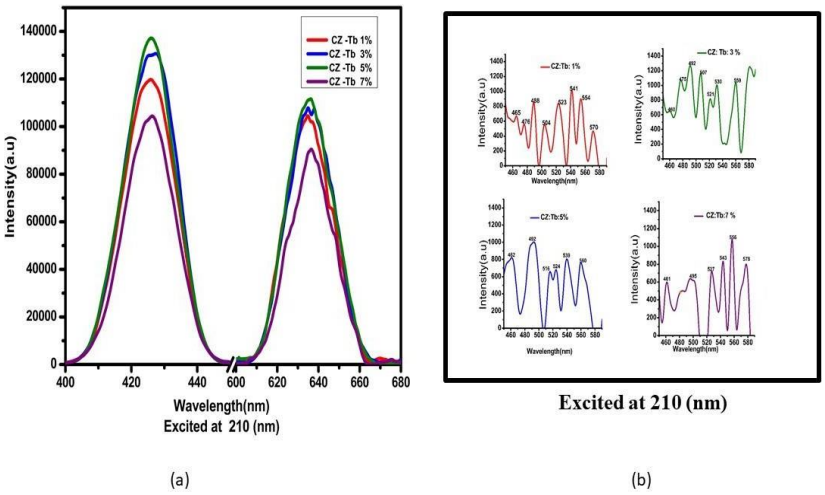

Fig 6.5. Fluorescence Spectra of Tb^{3+} doped CuO- ZnO nanocomposites (a) Wavelength 400-600nm (b) 460-580 nm excited at 210, sintered at 400^0C

The obtained results are suitable for the grow light as studied from the literature the important stages of plant growth require the Photosynthetically Active Radiation (PAR) spectra to play a vital role in this study to analyze the importance of photosynthesis, plants utilize light with wavelengths ranging from 400 to 700 nanometers. Blue light (400-500 nm) promotes vegetative growth, strengthens stems and leaves, and regulates plant shape. It is necessary for chlorophyll production and general plant health. Blue light is essential in the seedling stage because it promotes compact, strong growth and aids in the formation of leaves and stems and red light (600–700 nm) promotes flowering, fruiting, and seed germination. The combination of blue and red light is frequently employed to encourage healthy, strong growth. Blue light helps to maintain compact growth, but red light promotes foliage growth in this stage is called the vegetative stage. The 500-600 nm wavelength range, which includes blue-green and yellow-orange light, promotes plant growth. Although not as important as blue and red light, it helps to provide a balanced light spectrum that can improve overall plant health, photosynthesis, and development. Grow lights with changeable spectra allow the light to be fine-tuned to meet the needs of certain plants at different stages of growth. Full-spectrum lights are generally an excellent choice for most indoor growing applications; however, the light requirements may differ depending on the plant species and growth stage.[16]. Fig 6.5 shows fluorescence Spectra of doped terbium with nanocomposite (a) Wavelength 400-600nm (b) 460-580 nm excited at 210, sintered at 400^0C

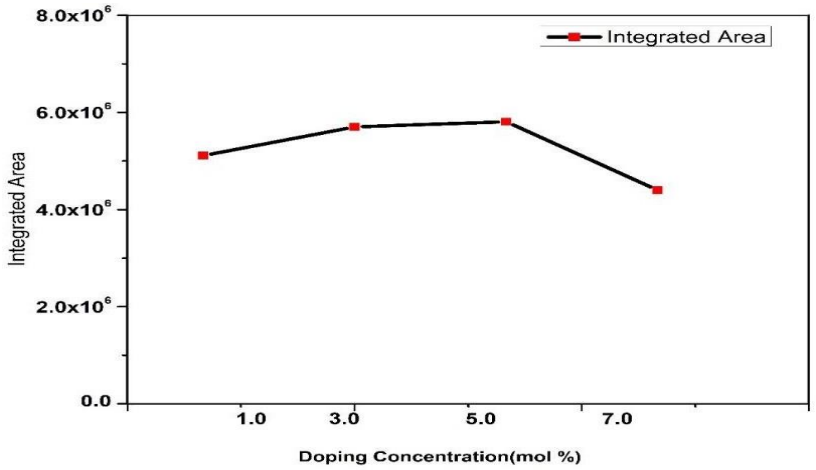

Fig 6.6: Integrated Areas of the Tb^{3+} doped CuO- ZnO nanocomposite excited at 210 sintered at 400^0 C.

For maximum indoor plant growth, use a well-balanced light spectrum that includes both red (600-700 nm) and blue (400-500 nm) wavelengths. Using the appropriate light spectrum can have a major impact on plant health and productivity, making it essential for successful indoor gardening. The color and spectrum of these devices can influence your plants' growth. Blue light encourages vegetative development, while red light promotes flowering and fruiting. It's important to consider the spectrum temperature measured in Kelvin (K). Grow lights with a high red-to-blue ratio (such as 650–675 nm red and 450–470 nm blue) are preferred in many cases, as these wavelengths are most effective for plant growth. Grow lights intended to support vegetative growth often have a more balanced spectrum with a slightly higher proportion of blue light (in the range of 450-500 nm), while flowering and fruiting lights tend to emphasize red wavelengths (in the 620-680 nm range). Typical CIE coordinates for plant growth lights: Grow lights designed for plant growth typically have coordinates around ($x \approx 0.34$, $y \approx 0.37$), which corresponds to a slightly cooler light with a higher concentration of blue wavelengths for vegetative growth. The more red-leaning lights for flowering and fruiting may shift toward ($x \approx 0.60$, $y \approx 0.35$) or higher red coordinates.

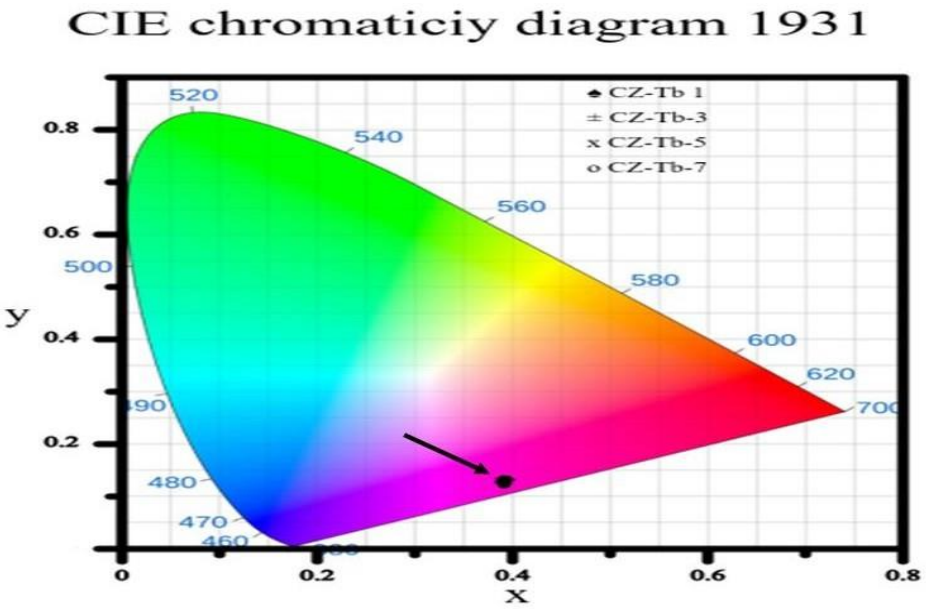

Fig 6.7. CIE coordinates of the terbium doped CuO- ZnO nanocomposites excited at 210 sintered at 400^0 C.

Table 6.2. Calculated CIE coordinates, CCT and quantum yield of the Tb doped CuO/ ZnO nanocomposites excited at 210 sintered at 400^0 C.

S.no	Sample	CIE (X,Y) Coordinates (Excited at 210)	CCT Coordinates	Quantum Yield (%)
1	CZ-Tb 1%	(0.39,0.13)	20056	66
2	CZ-Tb-3%	(0.38,0.13)	17786	60
3	CZ-Tb-5%	(0.39,0.13)	18211	58
4	CZ-Tb-7%	(0.38,0.12)	16528	75

6.2. Synthesis of Cobalt doped CuO/ZnO nanocomposite

6.2.1 X-Ray Diffraction

The powdered sample made for this study was analyzed using a Bruker diffractometer to determine its X-ray diffraction (XRD) patterns. In this pattern, the diffraction peaks marked with (x) correspond to CuO, while those marked with (o) correspond to ZnO. The XRD patterns of Co-doped CuO/ZnO precursors that were calcined at 400 °C were compared to undoped CuO/ZnO phosphors, as illustrated in Fig. 6.8. The crystal structure reveals a mixed phase of ZnO [JCDPS: 00-036-1451][17]and CuO [JCDPS: 80-1268] [18]. From the observed data, no new peaks were found in the XRD patterns of CuO/ZnO when doped with different concentrations of cobalt, suggesting that the material's phase remained consistent after doping. However, both the intensity and crystallite size of the material changed with increased cobalt concentration. When a crystal slightly deviates from its perfect order, its diffraction peaks may shift or broaden. This can result from various factors, such as crystal defects, changes in crystalline size, and lattice strain. Furthermore, the peak's width, intensity, and positional shifts may also be influenced by the crystalline size and lattice strain induced in the sample material. The XRD results confirm that after doping with cobalt (Co), the peaks in the CuO/ZnO sample shifted to lower 2θ angles. It’s important to note that because of the small size of the nanoparticles, not all of the added dopants may have fully integrated into the host lattice; some could be located on the surface or at the grain boundaries. [19-20]

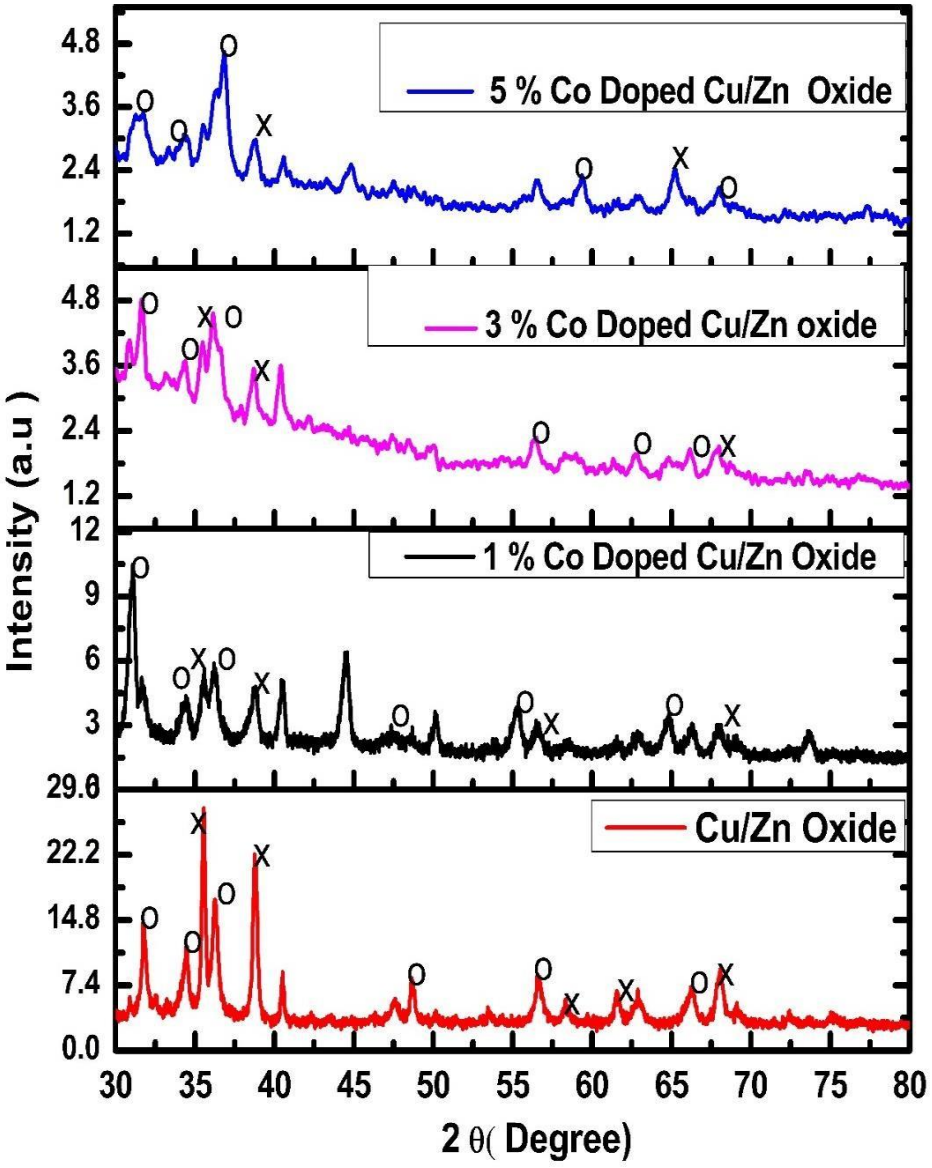

Fig 6.8: XRD spectra of pure ZnO, CuO and nanocomposites of Cobalt doped CuO/ZnO annealed at 400^0C.

Table 6.3 Crystallite size (D) and lattice strain of Cobalt doped ZnO/CuO sintered at 400^0C.

S.No	Sample	Structure	D (nm)	Lattice Strain ($\times 10^{-6}$)
1	CuO/ZnO	Mixed phase	28.46	2.85
2	CuO/ZnO-1 % Co	Mixed phase	22.15	2.45
3	CuO/ZnO-3%Co	Mixed Phase	17.00	3.20
4	CuO/ZnO-5%Co	Mixed Phase	16.36	4.52

6.2.2 FTIR spectroscopy

FTIR spectroscopy was conducted using a Perkin Elmer Fourier Transform Spectrometer over the wavenumber range of 400–4000 cm^{-1} to analyze the functional groups present in the precursors of Tb-doped CuO/ZnO composites, with varying concentrations of cobalt. The samples were sintered at 400°C, as depicted in Fig. 6.9. The FTIR spectra revealed absorption peaks in the region of 400–700 cm^{-1}**,** corresponding to metal-oxide vibrations, specifically Zn-O and Cu-O bonds, which remained unchanged upon cobalt doping. Additionally, peaks observed between 3500–2600 cm^{-1} were attributed to the presence of adsorbed water in the sample. An absorption peak around 1011 cm^{-1} was also noted, while absorption bands in the range of 1250–1580 nm were associated with the 4A2 → 4T1 (4F) transition of the tetrahedrally coordinated Co^{2+} ions. A peak at 1639 cm^{-1} pointed to C=N stretching vibrations, suggesting the coordination of nitrogen ligands with metal ions. Additionally, a strong absorption band from 2600 to 3500 cm^{-1} indicated moisture presence in the sample. FTIR results highlight the structural integrity and functional implications of cobalt doping in the nanocomposite [21-22].

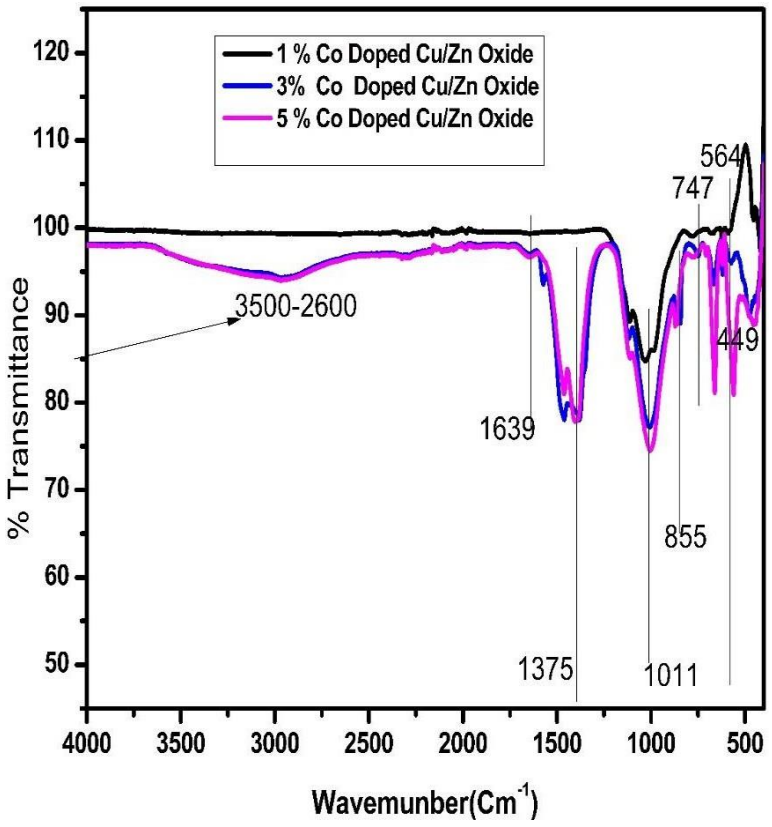

Fig 6.9 FTIR spectra of Cobalt doped CuO/ZnO nanocomposites prepared from banana peels sintered at 400 ^{0}C.

6.2.3 UV-Vis Spectroscopy

In the UV absorption spectrum of Co-doped CuO/ZnO oxide nanocomposites, strong absorption was observed in the 200–400 nm range as shown in Fig 6.10 This region is critical for understanding the material's electronic properties and band gap characteristics. The optical band gap can be calculated from the absorption data. The strong UV absorption indicates that the nanocomposite possesses significant electronic transitions, contributing to the calculated band gap. The results imply that cobalt doping influences the electronic structure, potentially narrowing or widening the band gap compared to pure CuO/ZnO. The precise value of the band gap obtained from this analysis can provide insights into the effectiveness of co-doping in tailoring the optical properties of the nanocomposite for specific applications. Furthermore, as the doping percentage in CuO/ZnO increased, a corresponding reduction in the optical

band gap was observed. Bandgap energy decreases with the doping concentration 3.90, 2.65, 2.48 eV for 1%, 3% and 5% Co doping respectively calculated by using tauc relation and shown in Fig 6.10(b). This phenomenon can be explained by examining various studies, which suggest that the decrease in the band gap may result from exchange interactions between the sp electrons and the d-electrons of the dopant. Alternatively, the presence of mid-band gap states could lead to a shift in the optical band gap.[23]

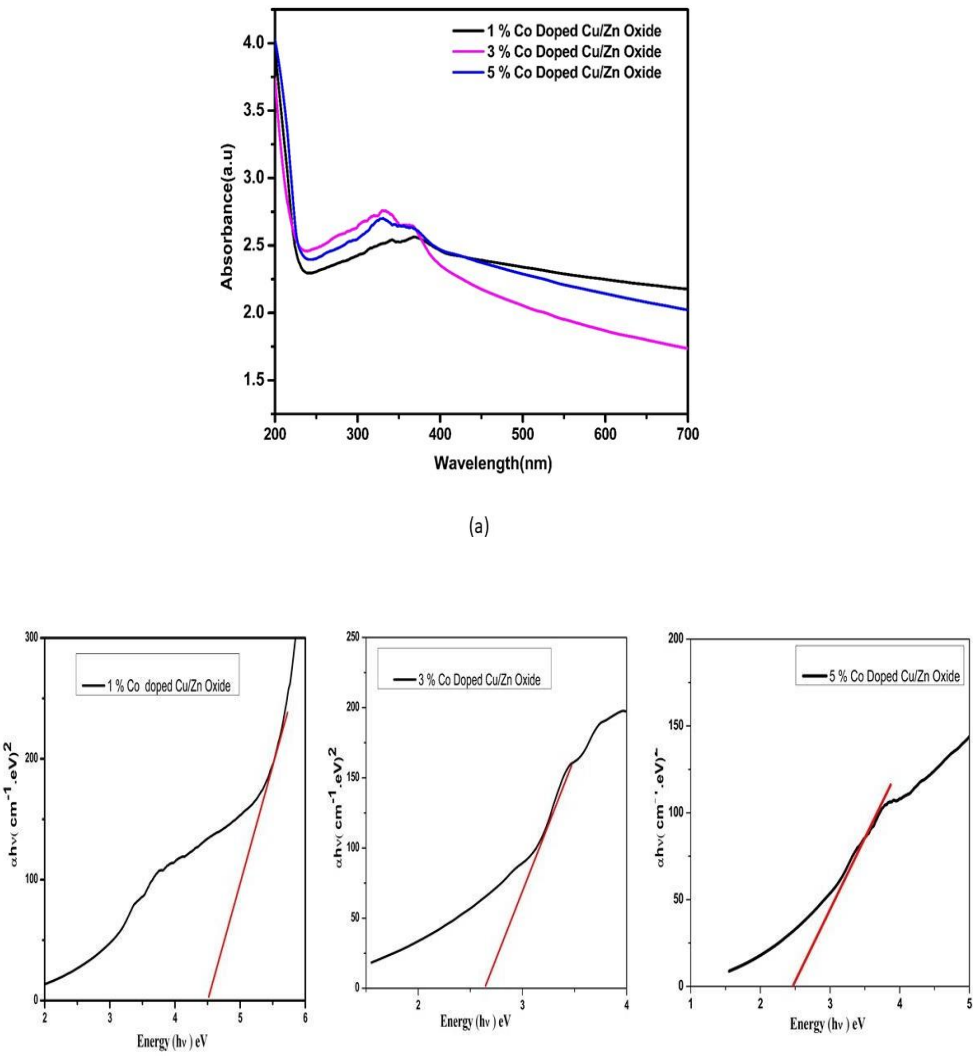

Fig 6.10. Plot of UV absorption spectra of Tb^{3+} doped CuO/ZnO nanocomposites (b) Tauc plot of the obtained UV spectra prepared from banana peels and sintered at400 ^{0}C.

6.2.4. Fluorescence Spectroscopy

The Fluorescence emissions of the prepared material were performed on all Co-doped samples using an excitation of UV light with a wavelength of 210 nm as shown in Fig 6.11. The transition line responsible for the blue emission observed in the Co-doped CuO/ZnO material is significant.

The fluorescent properties, excited by 210 nm, arise from both band edge emission and defect-related emission. The emission spectra of the Co-doped CuO/ZnO nanocomposite samples display peaks in violet, blue, and green within the 423–550 nm range. The violet emission peak is attributed to band edge emission, which occurs through a phonon-assisted indirect transition from the edge to the center of the band structure. In contrast, the blue and green emission peaks are linked to defect centers, particularly those associated with oxygen vacancies. The emission spectra of Co-doped Cu/Zn oxide (CZ Co doped Cu/Zn Oxide) show two main emission peaks: a strong one at 425 nm (blue region) and a comparatively weaker one at 640 nm (red region). These peaks vary with cobalt doping concentrations of 1%, 3%, and 5%. The 5% Co-doped sample shows the highest PL intensity, suggesting enhanced radiative recombination, likely due to increased defect density such as oxygen vacancies introduced by Co^{2+} ions. In contrast, the 3% Co-doped sample shows slightly lower intensity, possibly due to non-radiative recombination centers.

The emission wavelengths resemble known electronic d–d transitions of Co^{2+} ions in oxide matrices. For instance, the 425 nm peak corresponds to $4T1g(F) \rightarrow 4T1g(P)$, while the 640 nm peak falls within the range of $4T1g(F) \rightarrow 4T_{2g}(F)$ transitions [24-26]. However, the emissions are not solely due to these Co transitions. Instead, they originate mainly from defect-related recombination within the Cu/Zn oxide lattice, influenced by Co doping. Notably, the intensities of the blue and green emission peaks rise with increasing cobalt doping concentration, indicating a corresponding increase in defect centers. Overall, the fluorescence emission of cobalt- doped CuO/ZnO , excited by 210 nm, reflects various transitions involving cobalt ions and defect centers within the lattice. This information can provide valuable insights into the structural and optical characteristics of the material, as detailed in the corresponding PAR spectra.

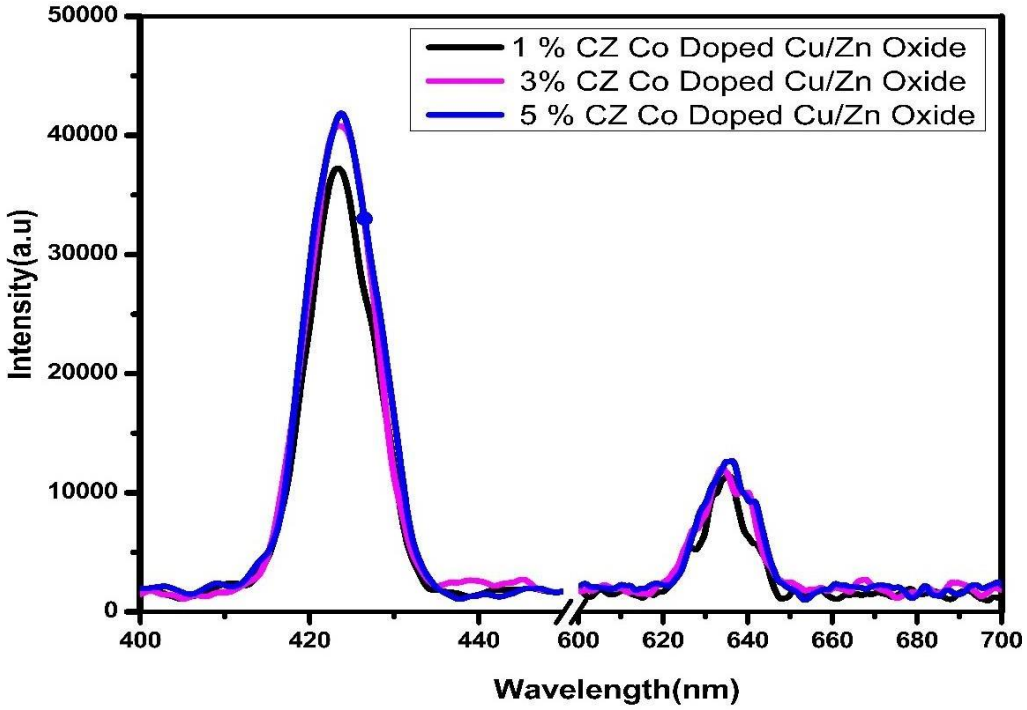

Fig 6.11. Fluorescence Spectra of Cobalt doped CuO/ZnO nanocomposites (a) wavelength 400-650nm (b) 450-580 nm excited at 210, sintered at 400^0C.

The color purity for all samples of Co-doped CuO/ZnO was calculated, along with the corresponding CIE and Correlated Color Temperature (CCT). This information is summarized in Table 6.3. Co-doped CuO/ZnO , determining color purity helps assess how effectively the material can produce specific colors, which is crucial for applications in lighting and displays. Overall, the high CRI values associated with the Co-doped CuO/ZnO nanocomposite samples suggest that they are more advantageous for white light applications, ensuring vibrant color rendering and enhancing visual quality, while they may not perform as effectively in applications requiring PAR lighting.

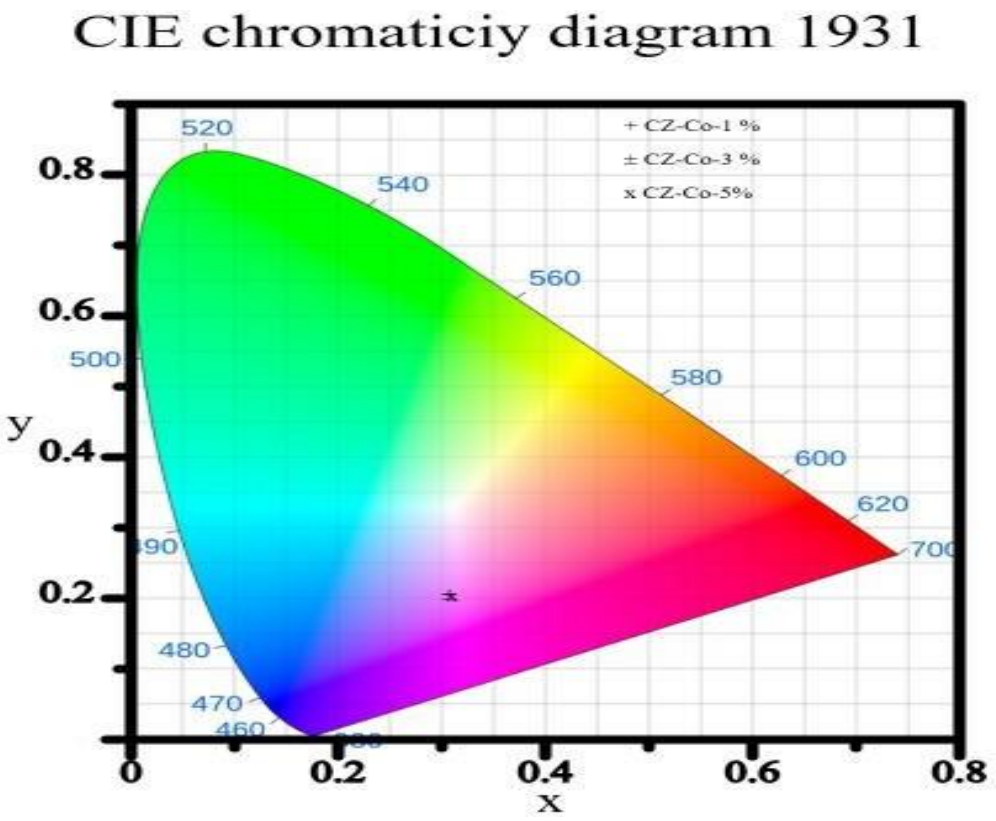

Fig 6.12. CIE coordinates of the Cobalt doped CuO- ZnO nanocomposites excited at 210 nm sintered at 400^0 C.

Table 6.4. Calculated CIE coordinates and CCT and quantum yield of the Cobalt doped Cu/Zn oxide nanocomposites metal oxide excited at 210 nm sintered at 400^0 C.

S.no	Sample	CIE (X,Y) Coordinates (Excited at 210)	CCT Coordinates	Quantum Yield (%)
1	CZ-Co 1%	(0.30,0.20)	19998	56
2	CZ-Co-3%	(0.30,0.20)	23015	52
3	CZ-Co-5%	(0.31,0.20)	20763	65

Conclusion

In this chapter Tb^{3+}/Co^{3+} doped with CuO/ZnO nanocomposite were successfully synthesized from banana peels.

1. The XRD data confirms the successful synthesis of Tb^{3+}/Co^{3+}-doped CuO/ZnO nanocomposites. It was observed that doping did not alter the overall structure of the nanocomposite; however, the Tb^{3+}-doped nanocomposites exhibited higher crystallinity compared to the Co^{3+}-doped ones. The donor states created by the Tb^{3+}/Co^{3+} ions help reduce the bandgap of ZnO, and the addition of CuO further narrows the bandgap, shifting the absorption edge towards longer wavelengths (redshift). This results in enhanced visible light absorption, making the composite material more efficient for use as a grow light.
2. When excited at 210 nm, the fluorescence of the nanocomposites emitted both red and blue lines. The integrated intensity was higher for the Tb^{3+}-doped sample compared to the Co^{3+}-doped sample, though both exhibited significant enhancements over the undoped CuO/ZnO material.
3. For optimal plant growth, light should primarily focus on wavelengths between 400 nm and 700 nm, which includes both blue (400–500 nm) and red (600–700 nm) light, commonly referred to as Photosynthetically Active Radiation (PAR), as these wavelengths are most effective for photosynthesis. Ideally, the light required for plant growth should lie in the purple region, a combination of blue and red light. Both Co^{3+}- and Tb^{3+}-doped composites achieved this objective, making them suitable for use in grow lights.
4. The color coordinates (CIE) for effective grow light fall within this purple range, and both Co^{3+}- and Tb^{3+}-doped composites were able to achieve this objective, making them suitable for enhancing plant growth through tailored lighting.

References:

1. Ö. Yıldız, A.M. Soydan, E.F. Ipçizade, D. Akın, and Ö. Uçak, "Properties of ZNO nanopowders synthesized by Glycine-Nitrate gel combustion," Acta Physica Polonica A **125**(2), 664–666 (2014).
2. S.A. Akintelu, A.S. Folorunso, F.A. Folorunso, and A.K. Oyebamiji, "Green synthesis of copper oxide nanoparticles for biomedical application and environmental remediation," Heliyon **6**(7), e04508 (2020).
3. T. Ghrib, I. Massoudi, A.L. Al-Otaibi, A. Al-Malki, A. Kharma, E. Al-Hashem, R.A. Al-Ghamdi, and R.A. Al-Zuraie, "Effects of terbium doping on structural, optical and photocatalytic properties of ZNO nanopowder prepared by Solid-State Reaction," Journal of Inorganic and Organometallic Polymers and Materials **31**(1), 239–250 (2020).
4. B. Choudhury, and A. Choudhury, "Luminescence characteristics of cobalt doped TiO2 nanoparticles," Journal of Luminescence **132**(1), 178–184 (2011).
5. S. Thakur, S. Thakur, J. Sharma, and S. Kumar, "Comparative study of Ni and Cu doped ZnO nanoparticles: Structural and optical properties," AIP Conference Proceedings, (2018).
6. A. Bala, S. Rani, A. Sharma, P.E. Lokhande, and D. Kumar, "Effect of Cobalt doping on luminescence properties of gadolinium aluminum garnet," Journal of Materials Science Materials in Electronics **34**(36), (2023).
7. I. Massoudi, and A. Rebey, "Analysis of in situ thin films epitaxy by reflectance spectroscopy: Effect of growth parameters," Superlattices and Microstructures **131**, 66–85 (2019).
8. A. Manikandan, E. Manikandan, B. Meenatchi, S. Vadivel, S.K. Jaganathan, R. Ladchumananandasivam, M. Henini, M. Maaza, and J.S. Aanand, "Rare earth element (REE) lanthanum doped zinc oxide (La: ZnO) nanomaterials: Synthesis structural optical and antibacterial studies," Journal of Alloys and Compounds **723**, 1155–1161 (2017).
9. A. Manikandan, E. Manikandan, B. Meenatchi, S. Vadivel, S.K. Jaganathan, R. Ladchumananandasivam, M. Henini, M. Maaza, and J.S. Aanand, "Rare earth element (REE) lanthanum doped zinc oxide (La: ZnO) nanomaterials: Synthesis structural optical and antibacterial studies," Journal of Alloys and Compounds

723, 1155–1161 (2017).

10. P.P. Pal, and J. Manam, “Photoluminescence and thermoluminescence studies of Tb3+ doped ZnO nanorods,” Materials Science and Engineering B **178**(7), 400–408 (2013).
11. I. Massoudi, A. Rebey, “Analysis of in situ thin films epitaxy by reflectance spectroscopy: effect of growth parameters,” Superlattices Microstructure, (2019).
12. O. Bechambi, S. Sayadi, and W. Najjar, “Photocatalytic degradation of bisphenol A in the presence of C-doped ZnO: Effect of operational parameters and photodegradation mechanism,” Journal of Industrial and Engineering Chemistry **32**, 201–210 (2015).
13. W.B. White, and V.G. Keramidas, “Vibrational spectra of oxides with the C-type rare earth oxide structure,” Spectrochimica Acta Part a Molecular Spectroscopy **28**(3), 501–509 (1972).
14. W.F. Van Der Weg, Th.J.A. Popma, and A.T. Vink, “Concentration dependence of UV and electron-excited Tb3+ luminescence in Y3Al5O12,” Journal of Applied Physics **57**(12), 5450–5456 (1985).
15. Z. Boruc, B. Fetlinski, M. Kaczkan, S. Turczynski, D. Pawlak, and M. Malinowski, “Temperature and concentration quenching of Tb3+ emissions in Y4Al2O9 crystals,” Journal of Alloys and Compounds **532**, 92–97 (2012).
16. Y. Park, and E.S. Runkle, “Spectral effects of light-emitting diodes on plant growth, visual color quality, and photosynthetic photon efficacy: White versus blue plus red radiation,” PLoS ONE **13**(8), e0202386 (2018).
17. J. Chauhan, Synthesis and Characterization Zinc, Nickel and Silver with Different Doping, Rajiv Gandhi Proudyogiki Vishwavidyalaya (2019).
18. J. Ponnarasan, V., & Krishnan, A, “Synthesis, structural and optical properties of cobalt doped CuO nanoparticles. International Journal of Nanoscience, **16**(2), 1650031 (2017).
19. J.I. Langford, and A.J.C. Wilson, “Scherrer after sixty years: A survey and some new results in the determination of crystallite size,” Journal of Applied Crystallography **11**(2), 102–113 (1978).
20. V.M. Vinosel, A. Amaliya, S. Vijayalakshmi, and S. Pauline, “Synthesis and characterization of Fe3O4 nanopowder and dielectric studies,” International

Journal of Technical Research and Applications **38**, 17–19 (2016).

21. J.K. Li, J.G. Li, X.L. Wu, S.H. Liu, X.D. Li, and X.D. Sun, “Crystal Structure Stabilization of Gadolinium Aluminum Garnet (Gd3Al5O12) and Photoluminescence Properties,” Key Engineering Materials **544**, 245–251 (2013).
22. J. Li, J. Li, Z. Zhang, X. Wu, S. Liu, X. Li, X. Sun, and Y. Sakka, “Gadolinium Aluminate Garnet (Gd3Al5O12): Crystal Structure Stabilization via Lutetium Doping and Properties of the (Gd1−xLux)3Al5O12 Solid Solutions (x = 0–0.5),” Journal of the American Ceramic Society **95**(3), 931–936 (2011).
23. B. Choudhury, and A. Choudhury, “Luminescence characteristics of cobalt doped TiO2 nanoparticles,” Journal of Luminescence **132**(1), 178–184 (2011).
24. A.M. Malyarevich, I.A. Denisov, K.V. Yumashev, O.S. Dymshits, and A.A. Zhilin, “Optical absorption and luminescence study of cobalt-doped magnesium aluminosilicate glass ceramics,” Journal of the Optical Society of America B **19**(8), 1815 (2002).
25. N. Serpone, “Is the Band Gap of Pristine TiO2 Narrowed by Anion- and Cation-Doping of Titanium Dioxide in Second-Generation Photocatalysts?,” The Journal of Physical Chemistry B **110**(48), 24287–24293 (2006).
26. W.-Y. Wu, Y.-M. Chang, and J.-M. Ting, “Room-Temperature synthesis of Single-Crystalline anatase TIO2 nanowires,” Crystal Growth & Design **10**(4), 1646–1651 (2010).
27. N.M. Rasdi, Y.W. Fen, N.A.S. Omar, R.S. Azis, and M.H.M. Zaid, “Effects of cobalt doping on structural, morphological, and optical properties of Zn2SiO4 nanophosphors prepared by sol-gel method,” Results in Physics **7**, 3820–3825 (2017).

Chapter 7

Summary and Future Scope

The study aimed to synthesize metal oxides (MOs) and their nanocomposites derived from green waste, specifically banana and potato peels, and evaluate their performance under grow light spectra. The targeted grow light spectra primarily encompass wavelengths between 400 nm and 700 nm, including blue light (400–500 nm) and red light (600–700 nm), collectively referred to as Photosynthetically Active Radiation (PAR). The research focused on achieving emission spectra that closely align with the grow light spectra (PAR).

To achieve this, MOs and their composites were successfully synthesized. The materials were then tested for their ability to produce grow light spectra through a mechanism involving red and blue phosphors excited by UV light. The synthesized materials effectively generated grow light spectra, contributing to the targeted wavelength range.

The key findings of the study are as follows:

1. MOs) were successfully such as MgO, NiO, ZnO, CuO, NiO, ZnO and Fe_3O_4 were synthesized from potato and banana peels. The structural and optical properties of the synthesized materials were thoroughly examined.
    - X-ray diffraction (XRD) analysis confirmed the successful synthesis of these metal oxides, and the phases obtained closely resemble those in the literature. The average crystallite size calculated by using Scherrer formula lies between the range from 9.84 nm-18.89 nm confirmed the formation of nanomaterial. The phases obtained for the metal oxides are as follows: CuO exhibits a monoclinic structure, NiO has a face-centered cubic (FCC) structure, ZnO adopts a hexagonal structure, MgO crystallizes in a cubic structure, and Fe_3O_4 has a cubic structure.
    - Yield of MOs(g) was found more with banana peels to those derived from potato peels.
    - Absorption spectra fall in UV region for all the metal oxides due to defect center formation and no absorption peak was observed in the blue region.

- The fluorescence results concluded that banana peel-derived MOs provide a better overall yield than potato peels. Also, all the metal oxides showed good emission in visible light when excited by UV light.

2. MOs nanocomposites MgO/NiO, MgO/CuO, CuO/ZnO and NiO/ZnO were successfully synthesis from banana peels and all the prepared nano-composite were characterized by UV absorption spectroscopy to understand the tuneability of band gap for grow light spectra. The following are the key finding from MOs nanocomposite:
   - Absorption spectra fall in the UV region for all the nanocomposites of the metal oxides due to defect center formation and no absorption peak was observed in the blue region. Among all the Nano composites CuO/ZnO Nano composites have maximum absorption in the UV region from 200-400 nm.
   - From the XRD analysis both the CuO and ZnO peaks which result in the mixed phase of CuO and ZnO i.e monoclinic and hexagonal structure that confirms the formation of nanocomposite
   - The morphology of pure CuO, ZnO and nanocomposite are spherical in shape. The grain size calculated from the FESEM is 22.89 nm for CuO, 15 nm for ZnO, and 23.28 for the nanocomposite $C_{20}Z_{80}$ (20% CuO and 80% ZnO)which is slightly larger than the crystallite size confirming that crystals of different crystallite sizes have strong magnetic interaction which forms particles of different sizes.
   - Upon excitation at 210 nm, the nanocomposite emits light in the near-purple region, while excitation at 310 nm results in red light emission. The $C_{20}Z_{80}$ (20% CuO and 80% ZnO) composition exhibited the highest fluorescence intensity, indicating its superior optical performance among the other composition of ZnO and CuO.
   - The near-purple emission at 210 nm corresponds to the blue light region, while the red emission at 310 nm aligns with the red-light requirement for photosynthesis. This makes the nanocomposite a viable candidate for PAR (Photosynthetically Active Radiation) light sources, which are crucial for efficient plant growth.

3. Tb^{3+}/Co^{3+} doped C20Z80 (20% CuO and 80% ZnO) nanocomposite were successfully synthesized from banana peels. The doping concentration of Tb^{3+} and Co^{3+} in C20Z80 nanocomposite are 1% ,3% ,5% ,7 %. The following are the key finding:
    - The XRD data confirms the successful synthesis of Tb^{3+}/Co^{3+}-doped C20Z80 nanocomposites. It was observed that doping did not alter the overall structure of the nanocomposite; however, the Tb^{3+}doped C20Z80 nanocomposites exhibited higher crystallinity compared to the Co^{3+}-doped C20Z80 nanocomposite. The donor states created by the Tb^{3+}/Co^{3+} ions help reduce the bandgap of ZnO, and the addition of CuO further narrows the bandgap, shifting the absorption edge towards longer wavelengths (redshift).
    - Tb^{3+}/Co^{3+} doped C20Z80 nanocomposite excited at 210 nm, the fluorescence of showed red and blue lines. The integrated intensity was higher for the Tb^{3+}-doped sample compared to the Co^{3+}-doped sample, though both exhibited significant enhancements as compared to CuO/ZnO nano-composite.
    - The color coordinates obtained for terbium and cobalt dopants at various concentrations are as follows: CZ-Tb 1% (0.39, 0.13), CZ-Tb 3% (0.38, 0.13), CZ-Tb 5% (0.39, 0.13), CZ-Tb 7% (0.38, 0.12); and for cobalt, CZ-Co 1% (0.30, 0.20), CZ-Co 3% (0.30, 0.20), CZ-Co 5% (0.31, 0.20) for effective grow light fall within this purple range, and both Co^{3+}- and Tb^{3+}-doped composites were able to achieve this objective, making them suitable for enhancing plant growth through tailored lighting. As shown below in Fig 7.1.

(a) (b)

Fig : 7.1 $C_{20}Z_{80}$ doped with (a) terbium (Tb^{3+}) and (b) cobalt (Co^{3+}) for grow light applications

For optimal plant growth, light should primarily focus on wavelengths between 400 nm and 700 nm, which includes both blue (400–500 nm) and red (600–700 nm) light, commonly referred to as Photosynthetically Active Radiation (PAR), as these wavelengths are most effective for photosynthesis. Ideally, the light required for plant growth should lie in the purple region, a combination of blue and red light. Both Co^{3+}- and Tb^{3+}-doped composites achieved this objective, making them suitable for use in grow lights.

List of paper published

1. J. Kaur and S. Rani, "Metal oxides synthesized from potato peels for grow light," Journal of Optics **52**(1), 41–48 (2023).

2. S. Kumar, S. Bakshi, S. Chaudhary, J. Kaur, A. P. Agrawal and S. Rani, "Heat Post-Treatment Effect on Optical and Electrical Properties of ZnS Thin Films," Biointerface Research in Applied Chemistry **14**(4), 100–108 (2024).

3. J. Kaur, F. Farooq and S. Rani, "Biogenic synthesis of copper oxide nanoparticles using green waste for the application of grow light," Materials Today: Proceedings **91**(1), 68–74 (2024).

4. J. Kaur, S. Kumar and S. Rani, "Effect on structural and optical properties of ZnO-CeO2-CdS nano-composite," AIP Conference Proceedings 3045(1), 020095 (2024).

5. J. Kaur and S. Rani, "CuO/NiO nano-composite synthesized from banana peels for grow light," Materials Today: Proceedings **81**(2), 216–222 (2023).

6. J. Kaur and S. Rani, "ZnO/CdS nano composite for visible light emission," AIP Conference Proceedings **2857**(1), 020016 (2023).

7. J. Kaur and S. Rani, "Comparative study on optical properties of pure ZnO and ZnO/CeO2 nano composite," AIP Conference Proceedings **2889**(1), 020035 (2023).

8. M. S. Afzal and J. Kaur, "Influence on the Optical properties of Green and Chemically Synthesized ZnO," Journal of Physics: Conference Series **833**(1), 012076 (2022).

9. J. Kaur , P Kaur and S Rani, "Investigation of optical and dielectric properties of metal oxides biogenically synthesized using banana peels". *Journal of Optics*, 1-14 (2025).